REPORT DOCUMENTATION PAGE	Form Approved OMB NO. 0704-0188

Public reporting burden for this collection of information is estimated to average 1 hour per response, including the time for reviewing instructions, searching existing data sources, gathering and maintaining the data needed, and completing and reviewing the collection of information. Send comment regarding this burden estimates or any other aspect of this collection of information, including suggestions for reducing this burden, to Washington Headquarters Services, Directorate for Information Operations and Reports, 1215 Jefferson Davis Highway, Suite 1204, Arlington, VA 22202-4302, and to the Office of Management and Budget, Paperwork Reduction Project (0704-0188), Washington, DC 20503.

1. AGENCY USE ONLY (Leave blank)	2. REPORT DATE September 21, 1999	3. REPORT TYPE AND DATES COVERED Final Report 15 July, 1996 - 14 July, 1999

4. TITLE AND SUBTITLE	5. FUNDING NUMBERS
Micromechanical Modeling of Superplastic Materials	Grant No. DAAH04-96-1-0226
6. AUTHOR(S) Dr. Namas Chandra (P. I.)	

7. PERFORMING ORGANIZATION NAMES(S) AND ADDRESS(ES) Florida A&M University Division of Sponsored Research 400 Foote Hilyer Administration Center Tallahassee, FL 32307	8. PERFORMING ORGANIZATION REPORT NUMBER

9. SPONSORING / MONITORING AGENCY NAME(S) AND ADDRESS(ES) U.S. Army Research Office P.O. Box 12211 Research Triangle Park, NC 27709-2211	10. SPONSORING / MONITORING AGENCY REPORT NUMBER ARO 35557.7-MS-SAH

11. SUPPLEMENTARY NOTES

The views, opinions and/or findings contained in this report are those of the author(s) and should not be construed as an official Department of the Army position, policy or decision, unless so designated by other documentation.

12a. DISTRIBUTION / AVAILABILITY STATEMENT Approved for public release; distribution unlimited.	12 b. DISTRIBUTION CODE

19991215 028

13. ABSTRACT (Maximum 200 words)

In this work, superplastic deformation were studied at atomistic, mesoscopic and macroscopic levels with a special focus on the former two. At the atomistic level, we studied the energy and structure of symmetric tilt boundaries and examined the energy barriers during grain boundary sliding of Aluminum bicrystal. We also studied the effect of temperature and impurity atoms on the structure, energy and deformation of grain boundary sliding.

At the mesoscopic level, polycrystal based micromechanical model was developed and append to conventional single-phase, dual-phase and high strain rate superplastic materials. This model has successfully predicted the flow-stress vs. strain rate and strain-rate sensitivity of conventional single-phase (7475 aluminium alloy, 2090-OE16 Al-Li alloy, and Al-Zn-Mg-Cu alloy), dual-phase (Ti-6Al-4V and Zn-22Al), and high strain-rate materials (IN905XL, IN9021 and IN90211).

At macroscopic level, the effect of the state of stain (uniaxial or biaxial) on the origin and evolution of cavities is Al based alloys were studied. This model was also integrated with finite element code. Most of the results are available at our web site: http://amml.eng.fsu.edu. In addition, an integrated web based simulation of SP process modeling was developed and implemented.

14. SUBJECT TERMS			15. NUMBER IF PAGES
			16. PRICE CODE

17. SECURITY CLASSIFICATION OR REPORT UNCLASSIFIED	18. SECURITY CLASSIFICATION OF THIS PAGE UNCLASSIFIED	19. SECURITY CLASSIFICATION OF ABSTRACT UNCLASSIFIED	20. LIMITATION OF ABSTRACT UL

MICROMECHANICAL MODELING OF SUPERPLASTIC MATERIALS

FINAL REPORT

Namas Chandra and Zhongyu Chen

September 1999

U.S. ARMY RESEARCH OFFICE

Grant No. DAAH04-96-1-0226

Department of Mechanical Engineering
FAMU-FSU College of Engineering
Florida A&M University
2525 Pottsdamer Street, Room 229
Tallahassee, FL 32310

EXECUTIVE SUMMARY

In this work, superplastic deformation were studied at atomistic, mesoscopic and macroscopic levels with a special focus on the former two. At the atomistic level, we studied the energy and structure of symmetric tilt boundaries and examined the energy barriers during grain boundary sliding of Aluminum bicrystal. We also studied the effect of temperature and impurity atoms on the structure, energy and deformation of grain boundary sliding.

At the mesoscopic level, polycrystal based micro-mechanical model was developed and append to conventional single-phase, dual-phase and high strain rate superplastic materials. This model has successfully predicted the flow-stress vs. strain rate and strain-rate sensitivity of conventional single-phase (7475 aluminum alloy, 2090-OE16 Al-Li alloy, and Al-Zn-Mg-Cu alloy), dual-phase (Ti-6Al-4V and Zn-22Al), and high strain-rate materials (IN905XL, IN9021 and IN90211).

At macroscopic level, the effect of the state of stain (uniaxial or biaxial) on the origin and evolution of cavities is Al based alloys were studied. This model was also integrated with finite element code. Most of the results are available at our web site: http://amml.eng.fsu.edu. In addition, an integrated web based simulation of SP process modeling was developed and implemented.

ACKNOWLEDGMENTS

PUBLICATIONS DURING THE PROJECT PERIOD 1996 - 1999

Journal Papers

1. N. Chandra and P. Dang, Atomistic Simulation of Grain Boundary Sliding and Migration, Journal of Materials Science, 34, 656 -666, (1999).

2. N. Chandra, Mechanics of Superplastic Deformations at Atomic Scale, Materials Science Forum, (1999).

3. P. Dang and N. Chandra A Micro-mechanical Model for Dual-Phase Superplastic Materials, Acta Materialia, 46, 8, 2851-1857, (1998).

4. N. Chandra, Industrial Applications of Superplasticity-A vision of the Future, Materials Science Forum, 243-245, 643-652 (1997).

5. N. Chandra and P. Dang, Numerical Modeling of Superplastic Deformation Mechanisms, Materials Science Forum, 243-245, 53-59 (1997).

6. N. Chandra, J. Rama and P. Dang, Application of Micro-mechanical Polycrystalline Model in the Study of Threshold Stress Effects on Superplasticity, Materials Science and Engineering, A231, 134-142, (1997).

7. N. Chandra and P. Dang, Application of Micro-mechanical Model to High Strain Rate Superplastic Materials, Scripta Materialia, 36, 1327-1332 (1997).

Proceedings (conference, symposium, congress)

8. J. Shih, U. Chandra and N. Chandra, Integrated Design Environment for the Manufacture of SPF components, Proceedings of Superplasticity and Superplastic Forming, ed. M. A. Khaleel, Pullman, Washington, pages 20-22, (1998).

9. P. Dang and N. Chandra, Atomic and Grain Level Modeling of Polycrystal Deformation, Modeling the Mechanical Response of Structural Materials, ed. E. M. Taleff and K. M. Rao, TMS Publications, ISBN 0-87339-329-9, 53-63, (1998).

10. Z. Chen, Z. Li, P. Dang and N. Chandra, Behavior of Titanium Alloy Under Uniaxial and Biaxial Superplastic Conditions, Modeling the Mechanical Response of Structural Materials, ed. E. M. Taleff and K. M. Rao, TMS Publications, ISBN 0-87339-329-9, 53-63, (1998).

11. N. Chandra and P. Dang, Study of Superplastic Deformation Mechanisms Using Atomistic Simulation Approach, Superplasticity and Superplastic Forming, ed. A. K. Ghosh and T. R. Bieler, TMS Publications, ISBN 0-87339-98-8, 53-64, (1988).

12. N. Chandra, Atomic and Grain Level Simulation of Superplastic Deformation, IMMM 97, Japan, (1997).

13. N. Chandra and P. Dang, Modeling Superplastic Deformation at Three Different Scales, Thermec '97, Australia, ISBN 0-87339-377-5, pages 1907-1914, (1997).

14. N. Chandra, Integrated Design Environment for the Manufacture of SPF Components, IMMM 97', Japan, (in print), July 1997.

15. N. Chandra and P. Dang, Atomistic and Continuum Modeling of High Temperature Deformation Mechanism, ICES 97', Costa Rica, pages1147-1152, (1997).

16. N. Chandra, Constitutive Modeling of Superplastic Materials Using Continuum Approach, Progress in Advanced Materials and Mechanics, ed. T. Wang and T.W. Chou, ICAM '96, Peking University Press, 374-380, (1996).

Conference Papers

1. Z. Li, Z. Chen, P. Dang and N Chandra, Cavitation Behavior of Superplastic Materials Under Biaxial Loading Conditions, TMS Annual Meeting, San Antonio, February 1998.

2. N Chandra, Integrated Design Environment for the Manufacture of SPF Components, IPMM 97, Brisbane, Australia, July 1997.

3. N. Chandra, Computational Materials Science, ICASE, NASA Langley, Williamsburg, VA, October 7-9, 1996.

4. N Chandra, Micro-mechanical Approach to the Constitutive Modeling of Superplastic Materials', U.S. Army Solid Mechanics Symposium, Myrtle Beach, SC, October 16-18, 1996.

GRADUATE STUDENTS AND POST-DOCTORAL ASSOCIATES

DR. K. MURALI
DR. PING DANG
ZHONGYU CHEN
JOHN WATTS
XIANGLEI CHEN

Contents

List of Tables

List of Figures

Chapter 1

Overview of the Research Effect

In this research effort, superplastic deformation mechanisms were examined at all the three scales with special focus on micro-mechanical and stomistic levels. At macro level, we examined the behavior of cavitation under different states of stress.

1.1   Meso-mechanical modeling of superplastic materials

The mechanical behavior of superplastic materials is characterized by a sigmoidal curve (regions I, II and III) spanning about seven to eight decades of strain rate in log σ - log$\dot{\epsilon}$ plot. Most of the superplastic deformation models cover only the superplastic regime (region II), over a small range of strain rate. We have previously proposed a model based on micro-mechanics to predict the mechanical behavior of material in regions II. In this work the model is modified to cover all the three regions and to predict the presence or absence of superplasticity in a given material. The new model incorporates a threshold stress term for diffusional flow at the atomic level which manifests as the experimentally observed threshold stress at the macro level. The model is applied to superplastic materials including statically recrystallized 7475 aluminum alloy, dynamically recrystallizing 2090-OE16 aluminum-lithium alloy and an Al-Zn-Mg-Cu alloy. With the introduction of the threshold stress, the influence of grain size and temperature on the behavior of these materials can be predicted over a wider range of strain rate. Also the maximum strain-rate sensitivity and its corresponding strain rate can be fairly accurately predicted. The variation of threshold stress with respect to grain size and temperature is also studied and an activation energy term is suggested for describing the threshold phenomenon.

The mechanical behavior of superplastic materials is characterized by a sigmoidal curve (regions I, II and III) spanning about seven to eight decades of strain rate in plot. Most of the superplastic deformation models cover only the superplastic regime (region II), over a small

1

given material. The new model incorporates a threshold stress term for diffusional flow at the atomic level that manifests as the experimentally observed threshold stress at the macro level. The model is applied to superplastic materials including statically recrystallized 7475 aluminum alloy, dynamically recrystallizing 2090-OE16 aluminum-lithium alloy and an Al-Zn-Mg-Cu alloy. With the introduction of the threshold stress, the influence of grain size and temperature on the behavior of these materials can be predicted over a wider range of strain rate. Also the maximum strain-rate sensitivity and its corresponding strain rate can be fairly accurately predicted. The variation of threshold stress with respect to grain size and temperature is also studied and an activation energy term is suggested for describing the threshold phenomenon.

1.2 Atomistic simulation

Inter-atomic potentials using Embedded Atom Method (EAM) are used in conjunction with molecular statics and dynamics calculations to study the sliding and migration of [110] symmetric tilt grain boundaries (STGB) in aluminum, under both applied displacement and force conditions. For equilibrium grain boundaries (without applied displacements and forces), three low energy configurations (corresponding to three twin structures) are found in the [110] STGB structures when grain boundary energies at 0 K are computed as a function of grain mis-orientation angle. "*Pure*" grain boundary sliding (GBS) without migration is implemented by applying external displacement. The propensity for "*pure*" GBS is evaluated by computing the energy associated with incremental equilibrium configurations during the sliding process, and the magnitude of the energy barriers is found to be much higher than that with migration. In contrast, in the applied force conditions, the energy barriers are reduced due to the fact that grain boundary sliding of STGB is always coupled with apparent migration. Relations between the applied force, internal stress field and displacement field are established and the role of grain boundary structure on the deformation process are examined. It is found that the GBS displacement is proportional to applied force, GB energy and time.

1.3 Cavitation study under superplastic conditions

Although pre-existing cavitation is controversial, the experimental evidence provided by directly observing as-received Al 5083 and Al 7475 sheet metal samples are supportive and convincing. Pre-existing cavities from previous thermo-mechanical processing do occur in both Al 5083 and Al 7475 superplastic alloys. The occurrence of pre-existing cavities is associated with second phase particles, especially those of a larger size. Numerical simulation verifies that there is a possibility of introduction of pre-existing cavities during single pass rolling process and that the occurrence depends on thickness reduction, particle size and bonding between

rolling process and that the occurrence depends on thickness reduction, particle size and bonding between

A quantitative study of cavity growth, cavitation behavior, and fracture behavior of a superplastic aluminum alloy, Al 5083, has been made under uniaxial tension and biaxial deformation. Pre-existing cavities were found in the vicinity of large Al_6Mn particles and aligned in a direction parallel to the rolling direction. Cavity stringers were also observed in the early stage of a superplastic deformation. However, with the increasing of deformation, the cavity stringers were masked by the concurrent nucleation and the interlinkage of cavities. The size and shape of the cavities, as well as the cavity volume fraction were measured using both image analysis and densitometry. Experimental results show that cavities continuously nucleate at the triple points of grains except for the pre-existing cavities. Discrepancy in the cavity volume fraction exists between the experimental results and the prediction made by the model assuming that all the cavities are pre-existed prior to deformation. The mechanism of cavity growth is thought to be diffusion controlled for small isolated voids, with a transition to the power-law controlled mechanism when cavities grow to a critical dimension. These critical cavity radii were determined to be 0.85 μm and 1.2 μm by the model for biaxial and uniaxial stress states respectively. Both morphological and densitometry results show that, cavity growth rate is higher under biaxial stress than that under uniaxial stress. At the same strain level, more and larger cavities could be found under biaxial stress. Extensive cavity interlinkage was observed in both states of stress before failure, but it indicates the opposite trend to the cavity growth rate. Under uniaxial stress, cavities are more prone to interlinkage than that under biaxial stress. The true thickness strains at failure are 1.06 for biaxial and 0.83 for uniaxial. FEM analysis indicates that stress level is higher at the interlinkage area under uniaxial stress.

Integrated systems bring together different applications, and/or software products that run on different platforms into one single cohesive environment. These systems are being continually developed in medium and large sized companies to solve business, scientific and engineering problems over the Intranet. However, the benefits are limited to a few companies with a sufficiently large workforce and budget. If these systems can be designed to be available over the Internet, the benefits will reach even smaller sized companies. This paper addresses the design of such a system. Such a design should consider control, data, and user interface dimensions while integrating the different components. Also, this design requires the use of a diverse set of concepts such as network programming, security, and coordination. This paper describes the design of a framework for developing an Internet-based Integrated Design System (IBIDS) and the implementation of a mechanical engineering application to demonstrate the concept. This work also describes the features of IBIDS and the rationale behind the design decisions.

Chapter 2

Application of Micro-mechanical Polycrystalline Model in the Study of Threshold Stress Effects on Superplasticity

2.1 Introduction

Superplasticity is the ability of certain fine grained materials to undergo several hundred percent elongation, when they are deformed within an optimum strain rate range (10^{-5} to 10^2 s^{-1}) and at temperatures greater than $0.5\,T_m$ where T_m is the absolute melting temperature. The mechanical behavior of a superplastic material is usually presented as a relationship between flow stress and strain rate on a $log\sigma$ - $log\dot{\epsilon}$ plot, which is often a sigmoidal curve as shown in Figure 2.1 [1]. The sigmoidal curve is usually divided into three regions based on the strain-rate sensitivity m, defined as the slope of the curve, i.e., $d(log\sigma)/d(log\dot{\epsilon})$. Region I and region III, at the lowest and highest ranges of $\dot{\epsilon}$ exhibit low values of m. Region II is the superplastic region with the highest value of m. The quantity m has been related both theoretically and experimentally to tensile elongations in superplastic materials. As can be seen from the curve, m continuously varies throughout the regions, hence, accurately modeling the shape of the curve in regions I and III is essential before m can be predicted in region II.

Figure 2.1 shows the presence of a plateau in region I, generally attributed to the existence of a threshold stress. Though the threshold stress behavior is exhibited in all superplastic materials, the magnitude of threshold stress is experimentally observed to be much higher for high strain-rate superplastic (HSRS) materials than that for conventional superplastic materials [2]. Threshold stress not only affects the material behavior in region I but also has a significant influence in region II. However, it has negligible effect on region III. In this paper, the micro-mechanical polycrystalline model developed earlier [3, 4] is extended

to describe the material behavior in all the regions, through the inclusion of the threshold stress term.

2.2 Micro-mechanical polycrystalline model

Grain boundary sliding (GBS) is believed to be the dominant strain producing mechanism during superplastic deformation. Most of the existing models relate the strain rate of the accommodation processes of GBS to the macroscopically measured superplastic strain rate. Such a relationship implies that the total strain in a superplastic material is governed purely by the accommodation processes. Using this concept, Chandra and co-workers [3, 4] have successfully developed a micro-mechanical polycrystalline model to predict the behavior of superplastic deformation with varying grain size and temperature in region II. This model significantly differs from the existing models in that it is developed from the grain level to the level of the aggregate in an explicit manner.

The micro-mechanical polycrystalline model used in this work is based on self consistent method, as shown in Figure 2.2. The development of this model for pseudo single phase materials has been fully described elsewhere [3, 4]. In this model, the three-dimensional polycrystal is obtained by rotating a basic crystal, aligned along the materials axes, first about the x_3 axis, then about the x_2 axis and finally about the x_1 axis. Due to the cubic symmetry, the rotation about each axis is taken to start from 0° to 75°, with an increment of 15°, leading to 216 grains with different orientations. This polycrystal model has been found to possess a reasonable three-dimensional isotropy [3]. The stress distribution inside the polycrystals is highly heterogeneous primarily due to the variation of grain orientation. Stress redistribution among various grains occurs continuously as the deformation proceeds. Since the accommodation activity of a constituent grain depends directly on its local stress, the superplastic deformation of the aggregate depends only on the level of accommodation in the constituent grains. The required principle of stress redistribution among the constituent grains is derived from the self-consistent relation.

If the incremental superplastic strain of a grain over a time increment dt is denoted by $d\epsilon_{ij}^{sp}$, and that of the aggregate by the corresponding barred (averaging) quantity $d\bar{\epsilon}_{ij}^{sp}$, the incremental stress variation of a grain can be written in the indicial form as

$$d\sigma_{ij} = d\bar{\sigma}_{ij} - 2\mu(1 - \beta)(d\epsilon_{ij}^{sp} - d\bar{\epsilon}_{ij}^{sp}), \qquad (2.1)$$

where μ is the shear modulus, and $\beta = 2(4 - 5\nu)/15(1 - \nu)$, ν being Poisson's ratio. The elastic isotropy for each constituent grain is assumed to obtain Equation (1).

The incremental superplastic strain of a grain is given by

$$d\epsilon_{ij}^{sp} = \dot{\epsilon}_{ij}^{sp} dt. \qquad (2.2)$$

Once $d\epsilon_{ij}^{sp}$ is determined for all the grains, the incremental superplastic strain of the polycrystalline aggregate can be calculated from the orientational average which is the numerical

average of the incremental superplastic strains of all the grains. Symbolically, this average can be expressed as

$$d\bar{\epsilon}_{ij}^{sp} = \{d\epsilon_{ij}^{sp}\}. \tag{2.3}$$

It may be noted that $\{d\sigma_{ij}\} = d\bar{\sigma}_{ij}$ results automatically from Equation (2.1), thereby justifying its self-consistency.

This micro-mechanical model considers all the grains to be uniformly sized and shaped and to have the same isotropic elastic constants. In this model, the presence of dispersions is not explicitly taken into account which leads to two different implications. The dispersions affect the elastic properties of the individual grains and this effect has been implicitly considered by the use of effective bulk properties. However, these dispersions along with any impurities that may be present in the material can also impose a barrier to the initiation of deformation manifested as the threshold stress. The effect of threshold stress has not been accounted in the previous work. In this work, threshold stress is introduced as an additional term in the constitutive equation. The concept of threshold stress and its application in the micro-mechanical model are explained later in the paper.

2.3 Constitutive Equations of Superplastic Deformation

The large tensile elongation observed in superplastic deformation is attributed to many different mechanisms including grain boundary sliding (GBS), grain rotation, grain switching, grain elongation and diffusional and dislocational creep. Geometrical models of superplastic flow consider sliding of individual grains or group of grains, the latter termed as cooperative grain boundary sliding (CGBS) [5]. In the present development since both GBS and CGBS have the same micro-mechanical feature, they are not considered separately. GBS has been shown to be the largest single contributor to total superplastic strain [6]. In fact, Langdon [7] suggests that all the superplastic deformation under optimum superplastic conditions is due to GBS. It was also suggested that the existing discrepancy between total macroscopic strain and strain due to GBS can be ascribed the limitations of the measuring procedure. Since superplastic material is a continuum in 3-D comprised of grains, GBS and other grain movements are possible only in the presence of accommodation processes. Since GBS by itself is a high rate process, the overall superplastic deformation rate can be considered to be controlled by these accommodation processes. Most of the superplastic deformation models relate the strain rate of the accommodation processes to the macroscopically measured strain rate by a proportionality factor built into their constitutive equations as shown in Table 1 of a paper by Sherby and Wadsworth [8].

The relationship between the macroscopic strain rate and the accommodation processes can be expressed in general as [8]:

$$\dot{\epsilon}^{sp} = K \cdot \dot{\epsilon}_{acc} \tag{2.4}$$

It is assumed that the proportionality remains constant in the ranges of strain rate, temperature and grain size considered. Even though this equation describes the macroscopic behavior of the material, a similar form is adopted in the development of micro-mechanical model at the grain level. Diffusional and dislocational creep are considered to be the major sources for accommodation, which has been suggested in the Ashby-Verrall model [9]. The overall strain rate, $\dot{\epsilon}_{acc}$, will be the sum of the strain rates contributed by each process as shown below:

$$\dot{\epsilon}_{acc} = \dot{\epsilon}_{diff.} + \dot{\epsilon}_{disloc.} \tag{2.5}$$

Diffusional flow is contributed from diffusion through crystal lattice (bulk or volume diffusion) and diffusion along grain boundaries (boundary diffusion). On this micro-continuum scale, the resolved normal stress σ_n acting on a slip plane has been found to direct the diffusion of atoms within the grains and grain boundaries [10]. Thus, the behavior of a slip system serves as a convenient method to study the micro-macro transition in modeling superplastic deformation. In order to model the grain boundary diffusional flow, grain boundary can be considered as made up of dislocations [11]. Thus the normal stress acting on the slip system can also be attributed to the grain boundary diffusional flow. The total accommodation due to diffusional flow for the k-th slip system (k varies from 1 to 12 for an FCC crystal) is then given by

$$\overset{(k)}{\dot{\epsilon}}_{diff.} = a_l \frac{1}{Td^2} exp \left(\frac{-Q_L}{RT} \right) (\overset{(k)}{\sigma_n}) + a_b \frac{1}{Td^3} exp \left(\frac{-Q_B}{RT} \right) (\overset{(k)}{\sigma_n}), \tag{2.6}$$

where Q_L is the activation energy of lattice diffusion, Q_B is the activation energy of grain boundary diffusion, T is the absolute temperature, d the grain diameter and R is the universal gas constant. a_l and a_b are material constants which are determined from experimental superplastic deformation data. However, we can define a ratio $r=a_b/a_l$, and this ratio r is found to be a material constant, as described in the appendix. Thus Equation (2.6) can be rewritten as

$$\overset{(k)}{\dot{\epsilon}}_{diff.} = a_l [\frac{1}{Td^2} exp \left(\frac{-Q_L}{RT} \right) (\overset{(k)}{\sigma_n}) + r \frac{1}{Td^3} exp \left(\frac{-Q_B}{RT} \right) (\overset{(k)}{\sigma_n})] \tag{2.7}$$

Equation (2.7) is different from the earlier versions (Equation (8) of reference [3]) in that the number of constants in the present form is reduced by one, with the introduction of the term $r = a_b/a_l$.

Accommodation due to dislocation is available through the movement of dislocations which has been modeled as glide of dislocations on the slip plane [12]. This glide of dislocations is directly influenced by the resolved shear stress τ acting on the slip plane. Using this approach, the accommodation rate due to dislocations is derived as,

$$\overset{(k)}{\dot{\gamma}}_{disloc.} = a_s \frac{1}{T} exp \left(\frac{-Q_L}{RT} \right) (\overset{(k)}{\tau})^n, \tag{2.8}$$

where a_s and n are material constants which are determined from experimental superplastic deformation data. Both the resolved normal stress σ_n and resolved shear stress τ of the k-th

slip plane are related to the local stresses σ_{ij} of the grain being considered:

$$\overset{(k)}{\sigma_n} = b_i b_j \sigma'_{ij}, \tag{2.9}$$

$$\overset{(k)}{\tau} = \frac{1}{2}(b_i n_j + b_j n_i)\sigma_{ij}, \tag{2.10}$$

where b_i and n_i are respectively the i-th component of the unit slip direction and slip-plane normal of the κ-th slip system, and σ'_{ij} is the deviatoric component of the local stress field.

As a_l, a_s and n are obtained from experimental data, the factor K mentioned in Equation (2.4) is taken into account within these constants. It should be noted that though a_l, a_s and n may possess constant numerical values, the influence of lattice, grain boundary diffusions and dislocation towards total strain rate drastically various in region I, II and III. Once the strain rate due to the k-th slip system is calculated from Equations (2.7) and (2.8), the superplastic strain-rate components of the considered grain can be obtained by the summation of the contributions of all the slip systems as following:

$$\dot{\epsilon}_{ij}^{sp} = \sum_k (b_i b_j - \frac{1}{3}\delta_{ij}) \overset{(k)}{\dot{\epsilon}}_{diff.} + \sum_k \frac{1}{2}(b_i n_j + b_j n_i) \overset{(k)}{\dot{\gamma}}_{disloc.} \tag{2.11}$$

where k varies from 1 to 12 for the FCC materials considered in this work.

2.4 Threshold Stress

The presence of threshold stress is evident from the plateau portion of region I of the sigmoidal curve of superplastic materials (Figure 2.1). This region represents the transition from conventional diffusional creep (Nabarro-Herring or Coble creep) to superplastic region. Though the macroscopic threshold stress σ_o has been experimentally observed in almost all of the superplastic materials, there is no consensus on the origin of σ_o. One major difficulty is the measurement of σ_o which occurs at extremely low strain rate (10^{-6} and below) in commercial superplastic materials. In this strain rate range, grain growth becomes a dominant factor, due to the extended period of test time. Other attempts to measure σ_o through stress relaxation test have been criticized due to the inability to account for changes in machine stiffness during extended period of test time at evaluated temperatures [7].

The presence of this low stress region I, restricts the range of region II in which superplastic behavior with high m values is present. Region I assumes a large role in high strain-rate superplastic materials, where this region extends for three to four decades of strain rate [2]. In the Ashby and Verrall model [9], a threshold stress is introduced in the diffusional based flow to account for the increased surface area of grains in an intermediate step of the grain switching process. In their model, $\sigma_o = 0.72\Gamma/d$ (Γ is the grain boundary free energy and d is the grain size) represents the fluctuations in the grain boundary area

and is responsible for the flat region I. This threshold stress is a constant at a given temperature. However, since experimental evidence shows that σ_o depends on temperature and also experimentally no quarter point (a point shared by four grains) is seen in superplastic deformation, there are some doubts on their theory [5].

In analyzing the experimental result of Zn-22%Al alloy and Pb-62%Sn alloy, Mohamed [13] concluded that threshold stresses strongly depend on temperature according to an equation of the form

$$\sigma_o = Bexp(\frac{Q_o}{RT}), \tag{2.12}$$

where B is a constant and Q_o is an activation energy term. They offered an explanation that the threshold stress results from the segregation of impurities at grain boundaries and their interactions with grain boundary dislocations. However, the activation energy of 240 KJ/mole for Zn-22%Al obtained in their study is much higher than the boundary activation energies of either Zn (60 KJ/mole) or Al (84 KJ/mole). In a detailed study of threshold stress in Al-Zn-Mg-Cu alloy system, Malek [14] evaluated σ_o by fitting all the data in regions I and II in a straight line by varying the value of m. By replotting the data using σ-σ_o instead of σ, he arrived at an activation energy of 140 KJ/mole which is close to that of self-diffusion coefficient (142 KJ/mole) of pure aluminum. Mukherjee and co-workers [15] analyzed a number of conventional and high strain-rate superplastic materials and noted a smooth transition in stress exponent with decrease in strain rate in regions I and II. They concluded that this change was due to threshold stress and the same mechanism is operative in region II and not due to a new deformation mechanism. However, the actual value σ_o is very sensitive to the chosen stress exponent, range of datum basis used in the analysis, and uncertainty in the experimental data. Sherby and Wadsworth [8] concluded after analyzing numerous published data that regions I, II and III can be explained as a combination of two independent processes, namely, GBS with threshold stress and power-law dislocation creep where the fastest process of the two is rate controlling. Their data indicated that threshold stress is a function of temperature, decreasing in magnitude with increase in temperature. The exact meaning of the threshold stress, and its values as a function of temperature and grain size are still an area of investigation [15]. Thus it is clear that though the existence of threshold stress is unequivocal, the explanation is still not fully understood.

In our micro-mechanical model, we introduce a threshold stress term σ_* in both the lattice and grain boundary diffusion equations. Thus Equation (2.7) is modified as

$$\overset{(k)}{\dot{\epsilon}}_{diff.} = a_l[\frac{1}{Td^2}exp\left(\frac{-Q_L}{RT}\right)(\overset{(k)}{\sigma_n} - \sigma_*) + r\frac{1}{Td^3}exp\left(\frac{-Q_B}{RT}\right)(\overset{(k)}{\sigma_n} - \sigma_*)]. \tag{2.13}$$

As discussed earlier, threshold stress arises due to the interaction of precipitates at the grain boundaries and particles within the grain necessary for the commencement of flow. A significant departure of σ_* in our approach to that of σ_o is that σ_* is based on the stress value at slip plane (micro) level, whereas σ_o is the experimentally determined macroscopic stress value. We further note that at this low strain-rate range, contribution from dislocation flow towards grain boundary sliding is negligible and Equation (2.8) is retained in its original form.

2.5 Application of Model

Though the proposed model could be applied to any single phase superplastic material, in this paper mainly aluminum based materials have been considered. The reason for this is the interest shown by automotive industries lately on aluminum and aluminum based alloys. Therefore in this paper, the model has been applied to aluminum based pseudo single phase alloys such as Al7475 and Al2090, whose experimental results are readily available. The model has also been applied to an Al-Zn-Mg-Cu alloy reported by Malek [14]. These reported experimental data include the effect of temperature and grain size on superplastic behavior and the sigmoidal curve describing all the regions.

The sigmoidal curve showing the relationship between the applied stress and strain rate during superplastic deformation is obtained by numerical simulation of step strain rate test. The polycrystal material is superplastically deformed at a constant strain rate and temperature until the applied stress value reaches a steady state. This steady state stress value is the flow stress at that particular strain rate and temperature. Then the material is further deformed at an increased strain rate, which results in a new corresponding flow stress. Thus by numerical simulation, at a particular constant temperature, the flow stress must be determined for a wide range of strain rates, including the specific strain rates reported in the experimental results. The appropriate material constants a_l, a_s, n and σ_* are chosen such that the simulation results match the experimental data for one specific temperature and a grain size. It should be noted that only one σ-$\dot{\epsilon}$ curve at a specific temperature and grain size is used in the evaluation of constants a_l, a_s and n. However, the threshold stress, σ_*, is found to be strongly dependent on temperature.

The first material that is considered for the study of temperature effect is Al7475, a statically recrystallized aluminum alloy. The thermo-mechanical property of this material has been reported by Hamilton et al [16]. The step strain rate tests were reported for 644°K, 700°K, 755°K and 789°K. The numerical simulation is carried out for the temperature at 700°K and grain size at 14 μm, and the material constants (a_l=0.065, a_s=0.00065 and n=6) and σ_* (temperature dependent parameter, to be discussed later in this paper) are obtained. The numerical simulation is subsequently carried out for other temperatures *by varying only the threshold stress, σ_* and keeping a_l, a_s and n as constants*. The simulation results compared with the experimental data are given in Figure 2.3. It is seen that the model has predicted successfully both the shape and values of the σ-$\dot{\epsilon}$ curves. Similarly the material constants (a_l=0.039, a_s=0.00065 and n=6) are obtained for Al2090-OE16, a dynamically recrystallizing aluminum-lithium alloy. The modeling results as well as the experimental thermo-mechanical properties of this material reported by Goforth and Srinivasan [17], are shown in Figure 2.4. The two sets of data are in fairly good agreement. The aluminum based alloy tested by Malek [14] has the composition (in weight per cent) Al-6.05Zn-1.91Mg-1.46Cu-0.15Cr-0.09Mn-0.12Fe, where chromium and magnesium rich particles were found to be distributed as second phase. Though the micro-mechanical model assumes the material as single phase, it describes the material behavior of this alloy successfully, as shown in Figure 2.5 (materials constants are a_l=0.032, a_s=0.00065 and n=6). The excellent agree-

ment between the simulation and experiment in all three regions can be attributed to the introduction of threshold stress.

The model is next applied to study the effect of varying grain size on the σ-$\dot{\epsilon}$ curve and threshold stress. Hamilton et al [16] have reported the effect of grain size on the superplastic behavior of Al7475 aluminum alloy. Various grain sizes (12.3, 16.3, 22, 69.4 and 156.3 microns) were obtained by thermo-mechanical treatment. The experiments were conducted at 789°K. For numerical simulation, the same material constants including the threshold stress at 789°K, obtained previously is then applied for different grain size materials. The effect of grain size in the micro-mechanical model depends on the grain size as given in Equation (2.13). Figure 2.6 shows the numerical predictions and experimental values. Considering that no modifications to the equations or to the constants are necessary to predict the grain size effect, the theoretical predictions are excellent. In order to verify the validity of the micro-mechanics-based model, an alternative numerical scheme using four new parameters was developed. In this curve fitting model, Equation (13) and (8) were directly used but without the summation of k slip systems in each grain as shown in Equation (11). This curve fitting model failed to predict the effect of temperature and grain size, especially that of grain size. This demonstrates that the summation over each slip system in all the grains is essential for the success of the micro-mechanical model.

As mentioned earlier, the superplastic strain rate is accommodated by lattice and boundary diffusional and dislocational movement of atoms. The relative contribution of each of these processes can be studied by computing the ratio strain rate of each of the processes to the total strain rate, expressed as percentage. Let $\dot{\epsilon}_l$ and $\dot{\epsilon}_{gb}$ represent the contribution of lattice and grain boundary diffusional accommodation towards the total strain rate $\dot{\epsilon}_{sp}$. $\dot{\epsilon}_l$ and $\dot{\epsilon}_{gb}$ can be computed from the two terms in Equation (13) by summing over all possible slip systems for all grains. Similarly $\dot{\epsilon}_d$, the dislocational contribution to the strain rate, can be calculated from Equation (8). Figure 2.7 shows the relative contributions of lattice and grain boundary diffusion and dislocation accommodations in Al 7475 alloy at 700°K and 789°K. As can be seen from the results, the diffusion contribution to the strain rate is dominant at low strain rate regions. The strain rate due to lattice diffusion is higher than that from boundary diffusion. The dislocational contribution $\dot{\epsilon}_d$ becomes larger as the strain rate increases. Also, at low temperature the relative contribution due to dislocation increases. Since threshold stress is present at low strain-rate region (region I), it is concluded from Figure 2.7 that the threshold stress arises from the diffusion process. This is the reason that we have introduced threshold stress only in the diffusion Equation (13) but not in the dislocation Equation (8).

The introduction of threshold stress also results in a better prediction of strain rate sensitivity (m), of the material. The plateau regions of the flow stress vs. strain rate curve in regions I and III, result in a bell shaped strain rate sensitivity curve, with a maximum value of m in region II (superplastic region). Figures 2.8 and 2.9 compare the predicted m curves at various grain sizes and temperatures with the experimental m curves for Al7475 and Al-Zn-Mg-Cu alloys respectively. As can be seen from these figures, the agreement of the entire m curve between numerical simulation and experiment is fairly good. A comparison

11

of the predictions and the corresponding experimental counterparts of maximum strain rate sensitivity with respect to varying temperature and grain size is made and is shown in Table 1.

We should note that in this model a_l, a_s and n remain as material constants whereas σ_* varies with temperature but not grain size. The threshold stress is found to be strongly dependent on temperature and independent of grain size, which is in agreement with the experimental observations [13]. Figure 2.10 shows the effect of temperature on the threshold stress in all three materials studied in this work. It is seen that the dependence of micro-level threshold stress on temperature can be expressed similar to Equation (11), with B_* and Q_*, respectively, a constant and an energy term at the slip plane level. If it turns out that B_* and Q_* are true materials constants then a total of five constants from one set of values are sufficient to describe superplastic behavior in regions I, II and III.

2.6 Summary and Conclusions

A micro-mechanical model using the concept of threshold stress has been proposed to model the superplastic deformation process. On a grain level, strains produced by diffusional and dislocational accommodation mechanisms are explicitly computed based on the fundamental material properties. The self-consistent method using Eshelby's approach is used to account for the effect of heterogeneity arising from the crystallographic orientation and the consequent stress field. The model is successfully applied to aluminum-based conventional superplastic materials. The material constants including the threshold stresses (σ_*) are evaluated from experimental data. These constants except σ_* are found to be true constants for a particular material irrespective of temperature and grain size etc. σ_* is found to be strongly dependent on temperature and independent of grain size. σ_* is also expressed in the form of activation energy, which can explain the decrease in σ_* levels with increase in temperature. Efforts to apply the threshold stress concept to the high strain-rate superplastic (HSRS) materials are currently in progress.

REFERENCES

1. J. Pilling and N. Ridley, Superplasticity in Crystalline Solids, The Institute of Metals, London, UK, 1989,

2. K. Higashi, T. Okada, T. Mukai and N. Tanimura, Scripta Metall., 26 (1992) 761.

3. K. Murali and N. Chandra, Acta Metall., 43 (1995) 1783.

4. N. Chandra and K. Murali, Scripta Metall., 32 (1995) 1429.

5. M. G. Zelin and A. K. Mukherjee, Mater. Sci. Eng., A208 (1996) 210.

6. R. B. Vastava and T. G. Langdon, Acta Metall., 27 (1979) 251.

7. T. G. Langdon, Mater. Sci. Eng., A174 (1994) 225.

8. O. D. Sherby and J. Wadsworth, Superplasticity in Metals, Ceramics, and Intermetallics, MRS Symposium Proceedings, ed. by M. J. Mayo, M. Kobayashi and J. Wadsworth, Materials Research Society, Pittsburgh, PA, 196 (1990) 3.

9. M. F. Ashby and R. A. Verrall, Acta Metall., 21 (1973) 149.

10. J. Weertman, Phil. Mag., 11 (1965) 1217.

11. D. McLean, Grain Boundaries in Metals, Oxford University Press, London, UK, 1957.

12. J. Weertman, J. Appl. Phy., 26 (1955) 1213.

13. F. A. Mohamed, J. Mater. Sci., 18 (1983) 582.

14. P. Malek, Mater. Sci. Eng., A137 (1991) 21.

15. R. S. Mishra, T. R. Bieler and A. K. Mukherjee, Mater. Sci. Forum, 170-172 (1994) 65.

16. C. H. Hamilton, C. C. Bampton and N. E. Paton, Superplastic Forming of Structural Alloys, ed. by N. E. Paton and C. H. Hamilton, TMS, PA, (1982) 173.

17. R. E. Goforth and M. N. Srinivasan, Advances in Superplasticity and Superplastic Forming, ed. by N. Chandra, H. Garmestani and R. E. Goforth, TMS, PA, (1993) 31.

Al7475 [16]	Temperature (K)	m (Experiment)	m (Theory)
	700	0.53	0.56
	755	0.61	0.64
	789	0.88	0.90
Al7475 [16]	Grain Size (μm)	m (Experiment)	m (Theory)
	12.3	0.86	0.90
	16.3	0.92	0.93
	22.0	0.94	0.95
	69.4	0.74	0.70
Al-Zn-Mg-Cu [14]	Temperature (K)	m (Experiment)	m (Theory)
	723	0.58	0.62
	748	0.59	0.71
	771	0.69	0.79
	789	0.74	0.82

Table 2.1: Comparison of maximum 'm' value
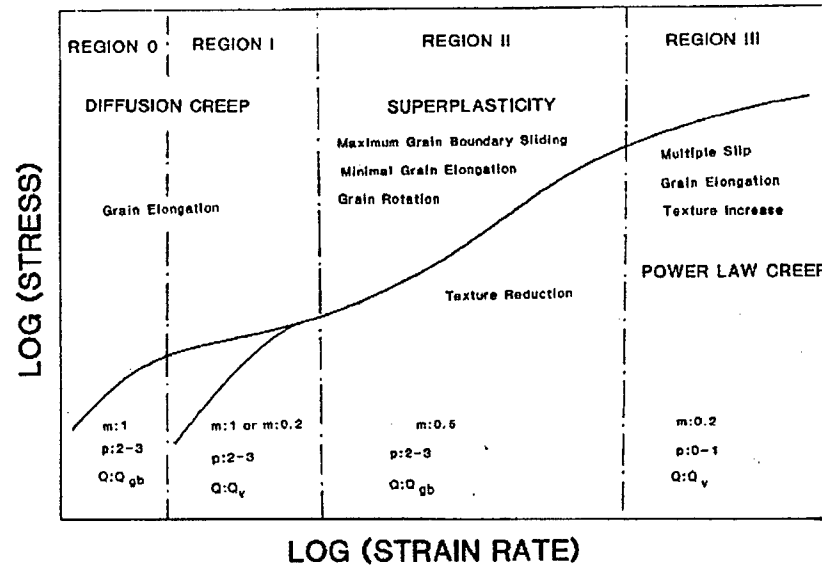
Figure 2.1: Schematic of the mechanical behavior of superplastic materials [1]
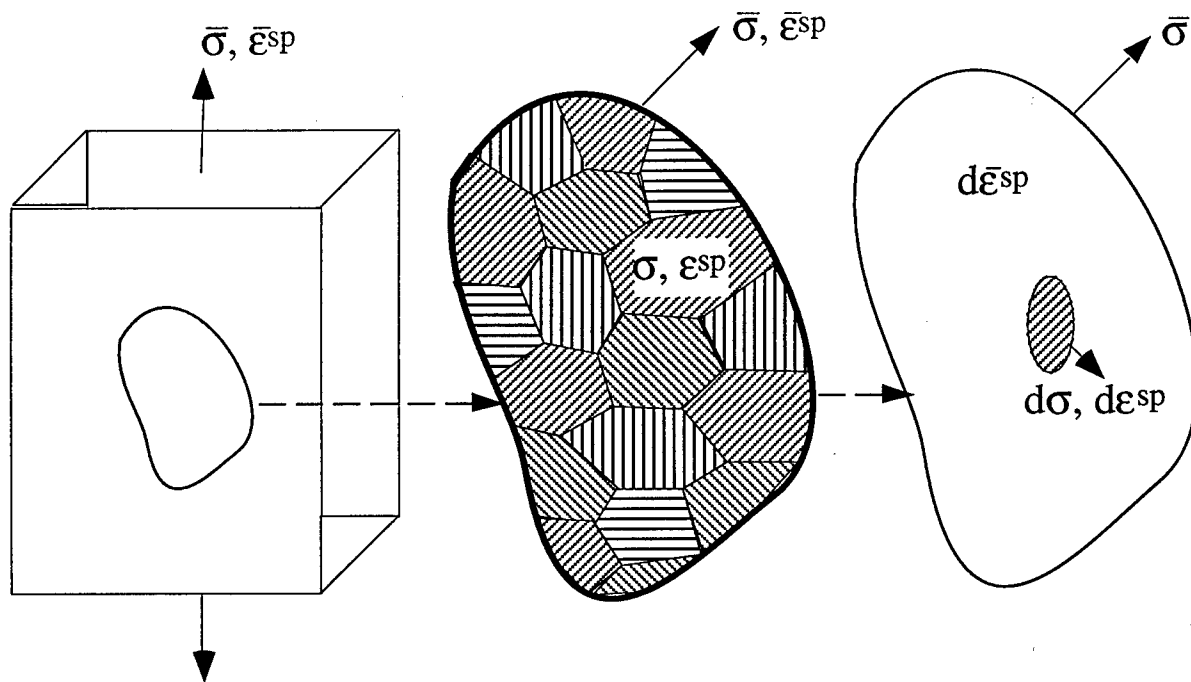
Figure 2.2: Polycrystalline model based on the self-consistent relation [2]
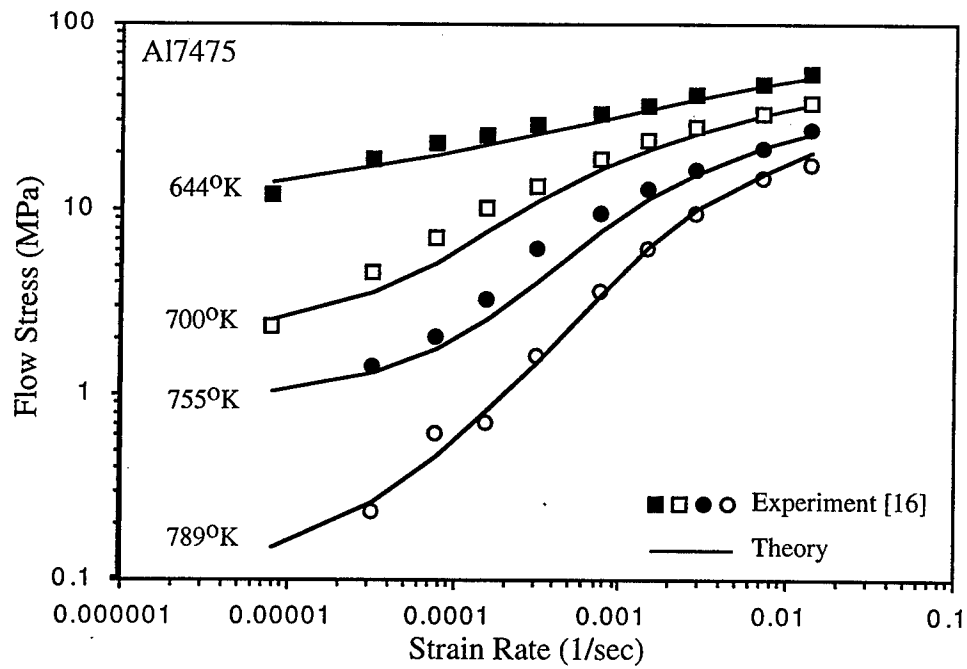
Figure 2.3: Micro-mechanical prediction of the flow stress-true strain rate behavior of Al7475 aluminum alloy.
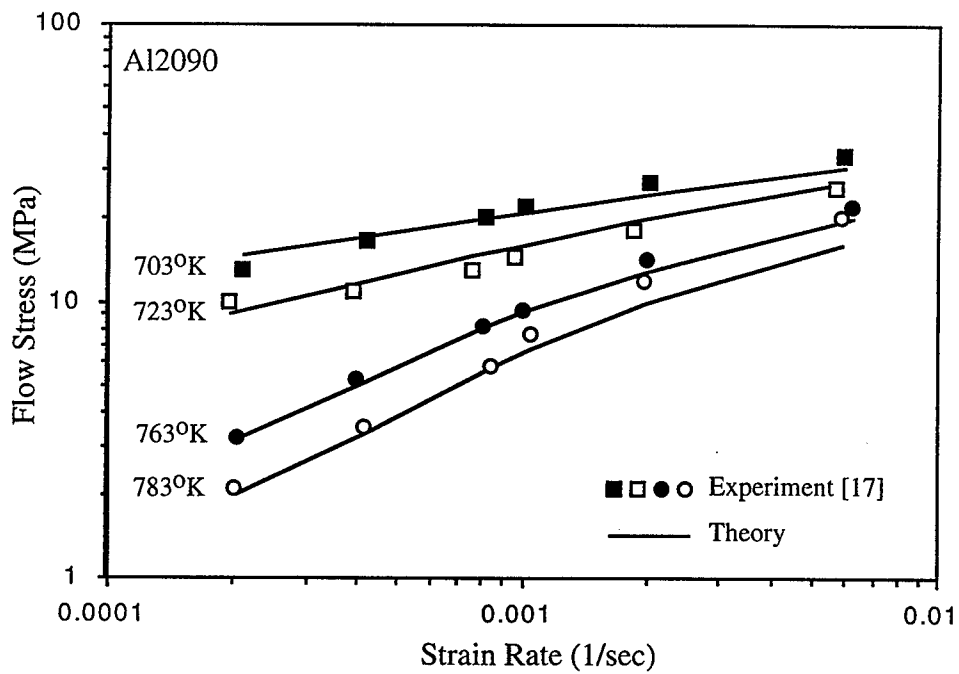
Figure 2.4: Micro-mechanical prediction of the flow stress-true strain rate behavior of Al2090 aluminum alloy.
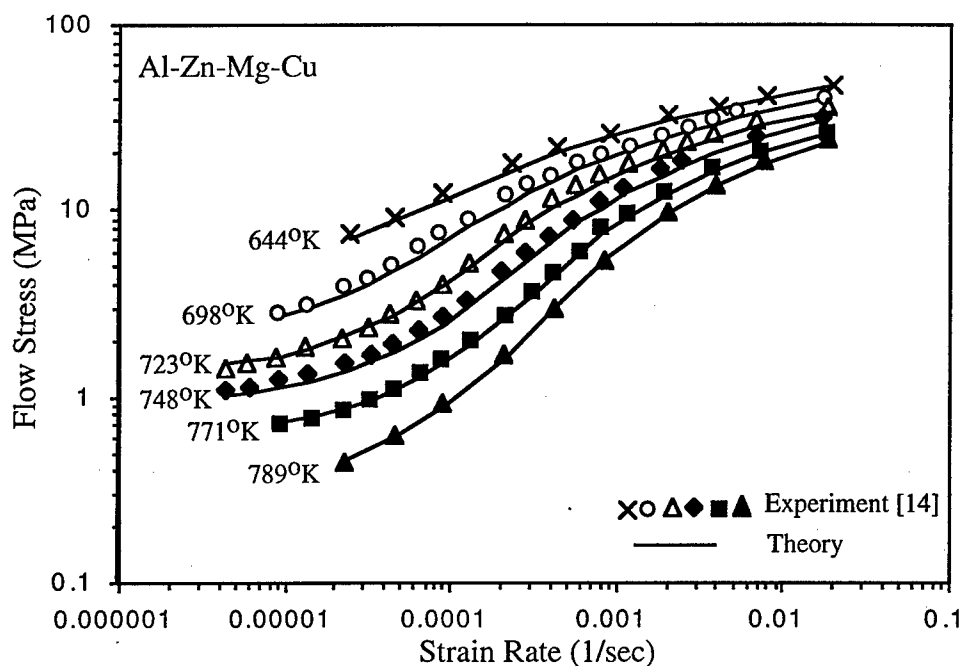
Figure 2.5: Micro-mechanical prediction of the flow stress-true strain rate behavior of an Al-Zn-Mg-Cu alloy.
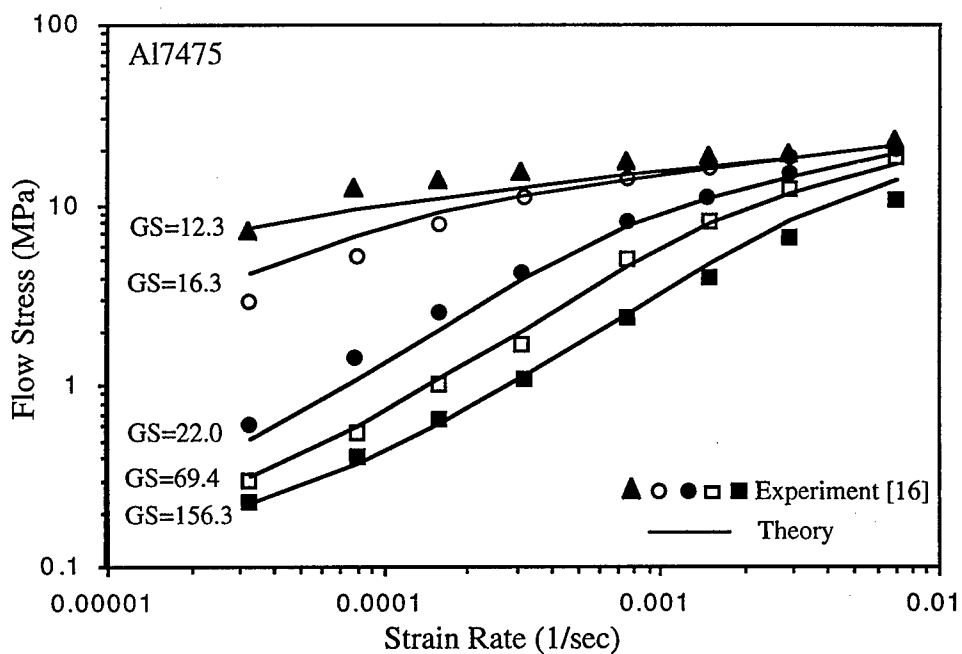
Figure 2.6: Independent prediction of the flow stress-true strain rate behavior of Al7475 aluminum alloy with different grain sizes.
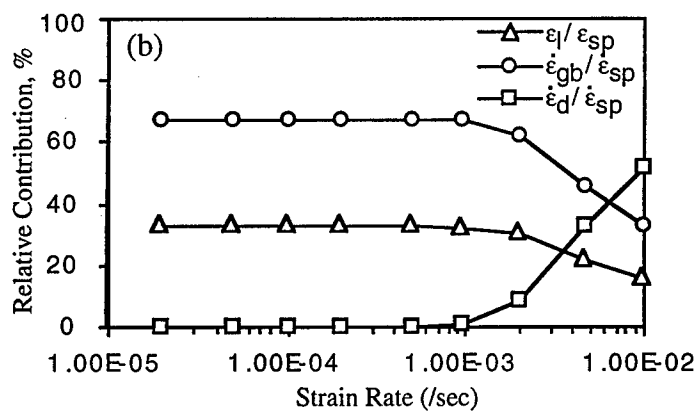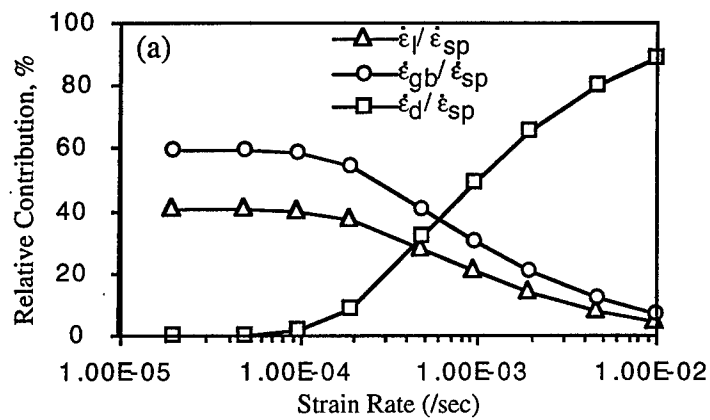
Figure 2.7: Relative contribution to the strain rate in Al 7475 alloy at (a) 700°K and (b) 789°K.
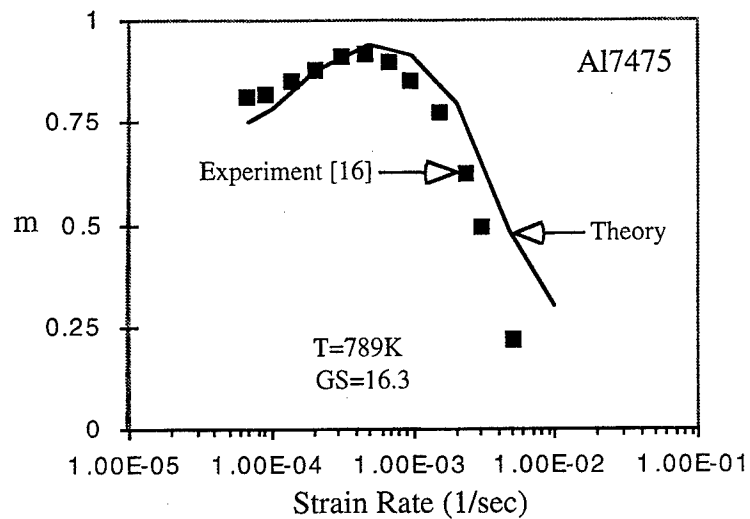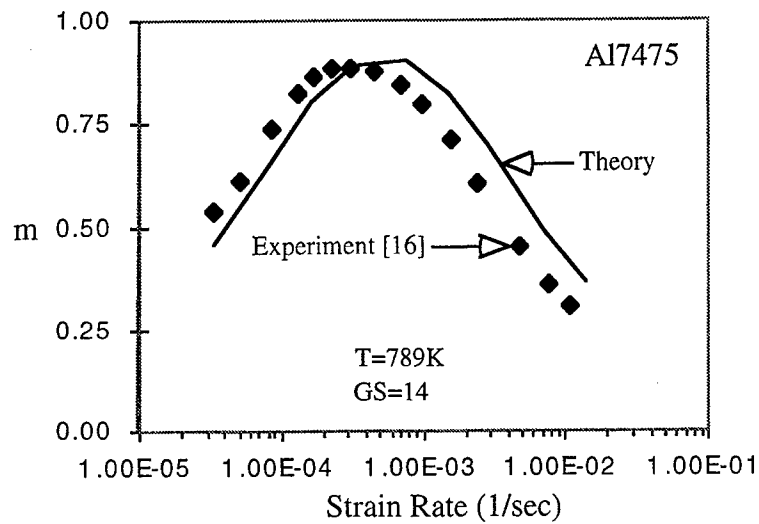
Figure 2.8: Independent prediction of strain rate sensitivity, m curve of Al7475 alloy with different grain size and the corresponding experimental data.
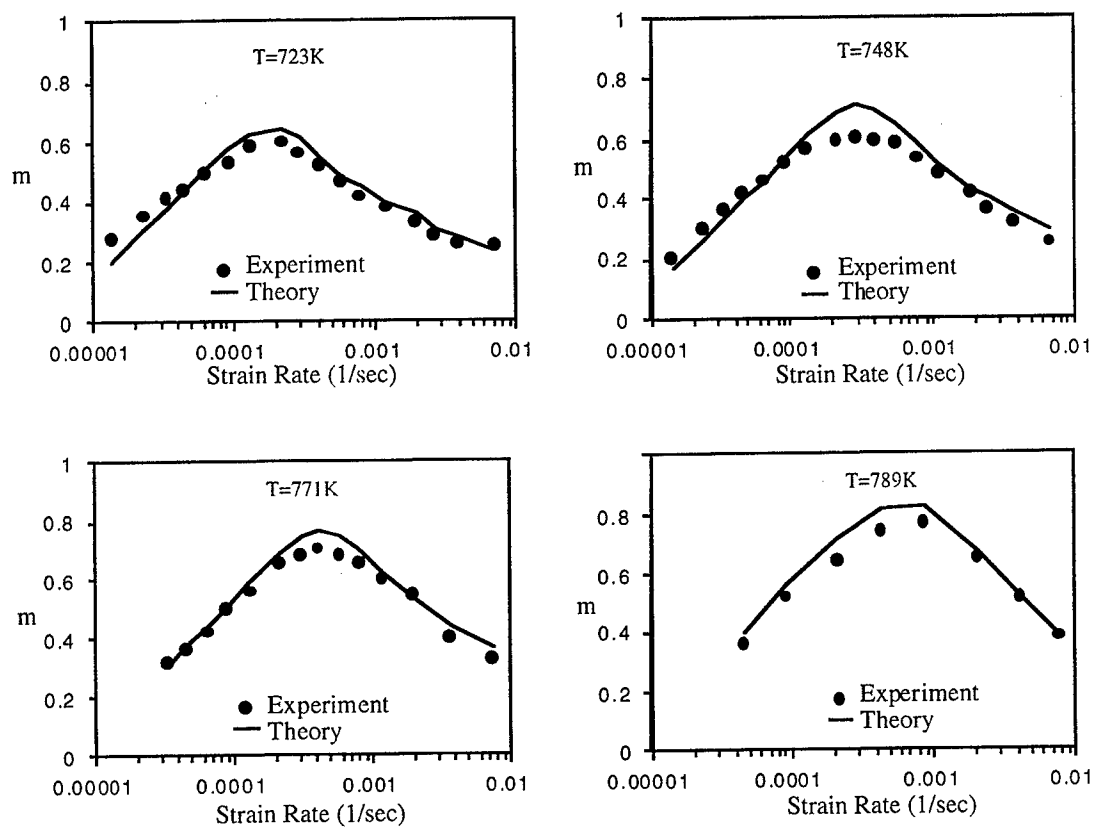
Figure 2.9: Independent prediction of m curve of Al-Zn-Mg-Cu alloy from the micromechanical model and the corresponding experimental data.
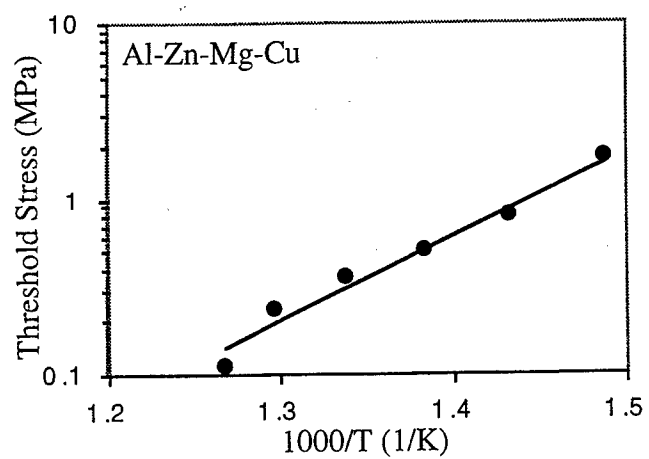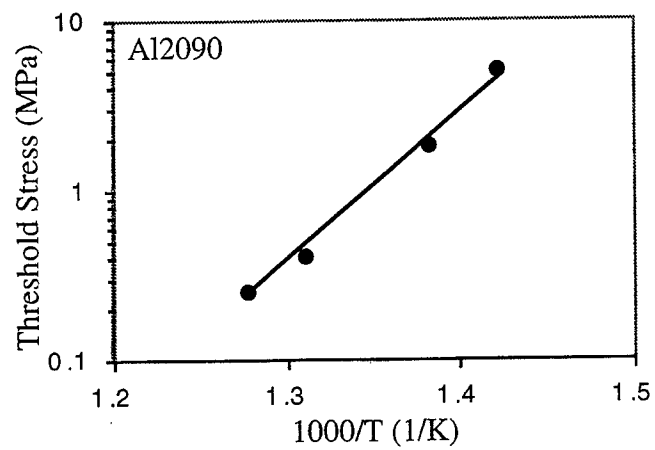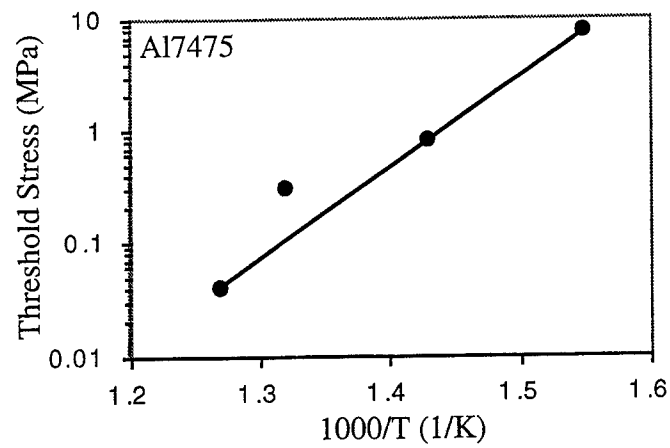
Figure 2.10: Dependence of micro-level threshold stress on temperature.

Chapter 3

A Micro-mechanical Model for Dual-Phase Superplastic Materials

3.1 Introduction

The mechanical behavior of superplastic materials is generally characterized by a sigmoidal curve in the log σ – log $\dot\epsilon$ plot [1]. Chandra and co-workers [2, 3] developed a micro-mechanical polycrystalline model to predict the thermo-mechanical behavior of superplastic deformation in single-phase materials. This model is different from other phenomenological models in that it is developed from the constituent grain level to the level of polycrystalline aggregate in an explicit manner. The model computes the strain fields in individual grains depending on their crystallographic orientation and the corresponding deformation mechanism at the slip plane level. The resulting stress distribution among the grains is accounted for by self-consistant relations. This micro-mechanical polycrystalline model was successfully applied to conventional and high strain-rate single-phase aluminum-based superplastic materials [4, 5]. However, many superplastic materials have two or more phases (e.g. Ti-6Al-4V, Zn-22Al and Pb-Sn). In general, each phase has its own crystal structure (e.g. in Ti-6Al-4V α phase has HCP structure while β phase has BCC structure), elastic properties (e.g. shear modulus and Poisson's ratio), and fundamental thermodynamic properties (e.g. diffusional coefficient and activation energy). The extension of polycrystalline theory from a single phase to two phases is non-trivial since the deformation behavior of each of the phases needs to be independently accounted for while the matrix is already a two phase aggregate.

In this paper, the single-phase Micro-mechanical polycrystalline model is modified to describe the material behavior of dual-phase materials. The developed method considers the individual elastic, inelastic and thermodynamic properties and crystalline structure (and hence the corresponding slip systems) of each of the two phases, and computes the overall response by using self-consistent method. Ti-6Al-4V and Zn-22Al alloys are selected as the model two-phase materials to validate the dual-phase micro-mechanical theory. Numerical solutions are compared with available experimental data, and the theory is used to predict

the effect of grain size and temperature on the superplastic flow behavior in these materials.

3.2 The Dual-phase Micro-mechanical Model

In a polycrystalline micro-mechanical model, two fundamental aspects need to be established. One is the relation between the global stresses (strains) of the multi-phase plolycrystalline aggregate and the local stress (strain) of the constituent phases and grains, and the other is the relation between the local stress and strain rate (strain), i.e. the constitutive equations. In our model, the first relation is developed based on self-consistent method, while the second relation is based on the accommodation processes of grain boundary sliding (GBS) at slip system level.

3.2.1 The self-consistent theory for two phases

During superplastic deformation, the stress distribution inside the polycrystals is highly heterogeneous primarily due to the variation of phases and grain orientations. Stress redistribution among various grains occurs continuously as the deformation proceeds. Since the accommodation activity of a constituent grain depends directly on its local stress, the superplastic deformation of the aggregate depends only on the level of accommodation in the constituent grains. This enable us to use the self-consistent method to derive the stress redistribution among the constituent phases and grains.

In order to generate a dual-phase polycrystal, a single-phase polycrystal is first generated following the procedure described elsewhere [2]. The dual phases (denoted as phase A and phase B) are introduced to the polycrystal by randomly assigning each of the grains to be either phase A or phase B, while keeping the overall fraction of each phase at the desired level (see Figure 3.1). The required principle of stress redistribution among the constituent grains is derived from the self-consistent relation, as illustrated in Figure 3.1. We develop the theory for phase A, while similar derivation can be easily carried out for phase B.

Consider an ellipsoidal inclusion (grain) of phase A embedded in an infinitely extended equivalent matrix (aggregate). The aggregate is subjected to a constant stress. The stress and the superplastic strain tensors of the inclusion are denoted by σ_A and ϵ_A^{sp}, while those of the aggregate are specified by the corresponding barred (averaging) quantities $\bar{\sigma}$ and $\bar{\epsilon}^{sp}$. When the equivalent matrix and inclusion undergo the stress-free incremental strains $d\bar{\epsilon}^{sp}$ and $d\epsilon_A^{sp}$, respectively, the self-consistent scheme can be formulated by the two-step process.

1. We first bring the inclusion out of the equivalent matrix, and let both deform freely by the given amounts. To bring the deformed inclusion back into the deformed matrix compatibly we apply a stress

$$d\sigma_{A_1} = -L_A \left(d\epsilon_A^{sp} - d\bar{\epsilon}^{sp} \right), \text{ or}$$
$$d\sigma_{A_1} = -L_A d\epsilon_A^* \tag{3.1}$$

on the inclusion, where L_A is elastic moduli tensor of phase A; $d\epsilon_A^* = d\epsilon_A^{sp} - d\bar{\epsilon}^{sp}$, is the inelastic deformation of phase A; and

$$d\bar{\epsilon}^{sp} = \frac{1}{n} \left[\sum_{i=1}^{n_A} d\epsilon_{Ai}^{sp} + \sum_{j=1}^{n_B} d\epsilon_{Bj}^{sp} \right]. \tag{3.2}$$

Here n_A is the number of grains of phase A and n is the total number of grains $(n_A + n_B)$.

2. To remove the unwanted layer of surface force we apply a surface traction characterized by $d\sigma^* = -d\sigma_{A_1}$ on the interface. Then the additional stress induced in the inclusion, denoted by $d\sigma_{A_2}$, is given by

$$d\sigma_{A_2} = L_A d\epsilon_A^{pt}, \tag{3.3}$$

where $d\epsilon_A^{pt}$ is the perturbed strain in the inclusion.

Thus, at the end of this operation the induced stress increment in the inclusion is the sum of $d\sigma_{A_1}$ and $d\sigma_{A_2}$, i.e.

$$d\sigma_A = L_A \left(d\epsilon_A^{pt} - d\epsilon_A^* \right). \tag{3.4}$$

Using Eshelby's equivalence principle, this can be written as

$$d\sigma_A = L \left(d\epsilon_A^{pt} - d\epsilon_A^* - d\epsilon_A^{**} \right), \tag{3.5}$$

where L is the elastic moduli tensor of the aggregate, and $d\epsilon_A^{**}$ is the equivalent eigen strain of the inhomogenous inclusion of phase A. The perturbed strain $d\epsilon_A^{pt}$ is related to $d\epsilon_A^* + d\epsilon_A^{**}$ through Eshelby's S tensor, as

$$d\epsilon_A^{pt} = S \left(d\epsilon_A^* + d\epsilon_A^{**} \right) \tag{3.6}$$

The components of the S tensor depend on the Poisson's ratio of the equivalent matrix ν and the aspect ratio (the length/diameter ratio) of the inclusions. From equations (3.5) and (3.6), the induced stress-increment in the inclusion $d\sigma_A$ can be written as

$$d\sigma_A = L \left[S \left(d\epsilon_A^* + d\epsilon_A^{**} \right) - \left(d\epsilon_A^* + d\epsilon_A^{**} \right) \right]. \tag{3.7}$$

From equations (3.4) and (3.6), $d\sigma_A$ can be written as

$$d\sigma_A = L_A \left[S \left(d\epsilon_A^* + d\epsilon_A^{**} \right) - d\epsilon_A^* \right]. \tag{3.8}$$

From equations (3.7) and (3.8), the relationship between $d\epsilon_A^{**}$ and $d\epsilon_A^*$ can be derived as follows:

$$d\epsilon_A^{**} = \left[(L_A - L) S + L \right]^{-1} L_A d\epsilon_A^* - d\epsilon_A^* \tag{3.9}$$

Substituting this back into equation (3.7), $d\sigma_A$ can be written as

$$d\sigma_A = -L \left[I - S \right] \left[(L_A - L) S + L \right]^{-1} L_A d\epsilon_A^* \tag{3.10}$$

24

where I is the fourth-rank identity tensor. When the inclusion is spherical and both the inclusion and equivalent matrix are isotropic, equation (3.10) reduces to

$$d\sigma_A = -2\mu_A \left[1 - \beta\right] \left[\frac{\mu_A}{(\mu_A - \mu)\beta + \mu}\right] (d\epsilon_A^{sp} - d\bar{\epsilon}^{sp}),\qquad(3.11)$$

where μ_A is the shear modulus of phase A, μ is the shear modulus of the aggregate, and $\beta = 2(4 - 5\nu)/15(1 - \nu)$, ν being Poisson's ratio of the aggregate. Equation (3.11) is the self-consistent relation modified for dual-phase materials. A similar relationship can be obtained for the induced stress-increment in grains of phase B, $d\sigma_B$.

During a constant strain rate test, the aggregate is further loaded with $d\bar{\sigma}$ at each incremental step. Then, with the assumed elastic isotropy for each constituent grain, we have,

$$d\sigma_A = d\bar{\sigma} - 2\mu_A \left[1 - \beta\right] \left[\frac{\mu_A}{(\mu_A - \mu)\beta + \mu}\right] (d\epsilon_A^{sp} - d\bar{\epsilon}^{sp}),\text{ and}$$

$$d\sigma_B = d\bar{\sigma} - 2\mu_B \left[1 - \beta\right] \left[\frac{\mu_B}{(\mu_B - \mu)\beta + \mu}\right] (d\epsilon_B^{sp} - d\bar{\epsilon}^{sp})\qquad(3.12)$$

Equations (3.12) provides the self-consistent variation of internal stress in the grain for each incremental step during a constant strain rate test.

3.2.2 Constitutive equations at slip system level

The large tensile elongation observed in superplastic deformation is attributed mainly to grain boundary sliding (GBS). Langdon [6] suggests that almost all the superplastic deformation under optimum superplastic conditions is due to GBS. Since superplastic material is a continuum in three-dimensional comprised of grains, GBS is possible only in the presence of accommodation processes. Furthermore GBS by itself is a high rate process, the overall superplastic deformation rate can be considered to be controlled by these accommodation processes. In this work, the overall strain rate, $\dot{\epsilon}_{acc}$, is considered as the GBS accommodations due to diffusion and dislocational creep as shown below:

$$\dot{\epsilon}_{acc} = \dot{\epsilon}_{diff.} + \dot{\epsilon}_{disloc.}\qquad(3.13)$$

Diffusion flow occurs as a result of the diffusion of atoms through the crystal lattice and along grain boundaries. The resolved normal stress acting on a slip plane has been found to direct the diffusion [7]. On the other hand, dislocation movement (e.g. glide) is directly related to the slip system (such as the resolved shear stress acting on a slip plane along the slip direction). Thus, the behavior of slip systems serve as a convenient method to study the constitutive equations at micro level and the micro-macro transitions in modeling

superplastic deformation. The accommodation due to diffusional flow for kth slip system in each phase is given by

$$\overset{(k)}{\dot{\epsilon}}_{diff.} = a_l\left[\frac{1}{Td^2}exp\left(\frac{-Q_L}{RT}\right)(\overset{(k)}{\sigma_n} - \sigma_*) + r\frac{1}{Td^3}exp\left(\frac{-Q_B}{RT}\right)(\overset{(k)}{\sigma_n} - \sigma_*)\right]. \qquad (3.14)$$

where k varies from 1 to 12 for the FCC $\{111\}$ $<\bar{1}10>$ slip systems, 1 to 12 for the BCC $\{110\}$ $<\bar{1}11>$ slip systems and from 1 to 6 for HCP $\{0001\}$ $<11\bar{2}0>$ and $\{\bar{1}100\}$ $<\bar{1}\bar{1}20>$ slip systems. Q_L and Q_B are the activation energy of lattice diffusion and grain boundary diffusion respectively, T is the absolute temperature, d is the grain diameter, R is the universal gas constant, σ_n is the resolved normal stress acting on the slip plane, σ_* is the threshold stress term at the slip plane level, $r = 3.3\delta D_{0B}/D_{0L}$ is a materials constant [3, 8] and the remaining constant a_l is a fitting parameter to be determined from the experimental data.

The accommodation equation due to dislocation movement can be written as:

$$\overset{(k)}{\dot{\gamma}}_{disloc.} = a_s\frac{1}{T}exp\left(\frac{-Q_L}{RT}\right)(\overset{(k)}{\tau})^n, \qquad (3.15)$$

where τ is the resolved shear stress acting on the slip plane, a_s is a material constant to be determined from experimental data of the specific phase under consideration, and n is the stress exponent.

Both the resolved normal stress σ_n and resolved shear stress τ of the k-th slip plane are related to the local stresses σ_{ij} of the grain being considered:

$$\overset{(k)}{\sigma_n} = b_i b_j \sigma'_{ij}, \qquad (3.16)$$

$$\overset{(k)}{\tau} = \frac{1}{2}(b_i n_j + b_j n_i)\sigma_{ij}, \qquad (3.17)$$

where b_i and n_i are respectively the i-th component of the unit slip direction and slip-plane normal of the κ-th slip system, and σ'_{ij} is the deviatoric component of the local stress field.

Equations (3.14) and (3.15) relate the local stress and strain rate for a given slip system. In these equations, the parameters Q_L, Q_B and r are different for different phases and their values are available in the literature [8]. The remaining fitting parameters a_l, a_s and σ_* are selected by matching the known experimental data. We use the same values of these parameters for both the phases since the superplasticity in dual-phase materials occurs only at a specified combination of the constituent phases while each phase by itself may not exhibit superplasticity, and also the fitted experimental data are obtained from the dual-phase material and not from its single constituent phase.

Once the strain rate due to the k-th slip system is calculated from equations (3.14) and (3.15), the superplastic strain-rate components of the considered grain can be obtained by the summation of the contributions of all the slip systems as following:

$$\dot{\epsilon}_{ij}^g = \sum_k (b_i b_j - \frac{1}{3}\delta_{ij})\overset{(k)}{\dot{\epsilon}}_{diff.} + \sum_k \frac{1}{2}(b_i n_j + b_j n_i)\overset{(k)}{\dot{\gamma}}_{disloc.} \qquad (3.18)$$

26

where k varies depending on the crystalline structure of the phase being considered. The incremental superplastic strain of a grain is given by

$$d\epsilon_{ij}^g = \dot{\epsilon}_{ij}^g dt. \tag{3.19}$$

Once $d\epsilon_{ij}^g$ is determined for all the grains, the incremental superplastic strain of the polycrystalline aggregate can be calculated from the orientational average which is the numerical average of the incremental superplastic strains of all the grains. Symbolically, this average can be expressed as

$$d\bar{\epsilon}_{ij}^{sp} = \{d\epsilon_{ij}^g\}. \tag{3.20}$$

Equations (3.12) and (3.20) are therefore the required relations to describe a dual-phase polycrystalline superplastic behavior.

3.3   Application of Model

The sigmoidal curve showing the relationship between the applied stress and strain rate during superplastic deformation was obtained by numerical simulation of step strain rate test. The polycrystal material was superplastically deformed at a specified constant strain rate, grain size and temperature until the applied stress value reaches a steady state. This steady state stress value is the flow stress at that particular strain rate, grain size and temperature. Then the material is deformed at an increased strain rate resulting in a corresponding flow stress. Thus by numerical simulation, at a particular constant temperature and grain size, the flow stress can be determined for a wide range of strain rates, including the specific strain rates reported in the experimental results. The appropriate material parameters a_l, a_s and σ_* are chosen such that the simulation results match the experimental data for one specific temperature and a grain size. *It should be noted that only one σ-$\dot{\epsilon}$ curve at a specific temperature and grain size is used in the evaluation of constants a_l and a_s.* However, the threshold stress, σ_*, is found to be strongly dependent on temperature.

When the experimental flow stress vs. strain rate data are used to evaluate the material parameters, the parameters are valid for a range of grain sizes, temperatures and phase ratios. Thus when these parameters are significantly far from the test conditions, the model may not be valid. This is especially true if new mechanisms not included in the original formulations become active. As an example, if the phase ratios are very different (e.g. α+90% β) from that observed for superplasticity (e.g. α+50% β) in Ti-6Al-4V alloy, the model will not be valid. In the present model, the overall volume fractions of phases are considered without regard to their specific spatial arrangement.

3.3.1   Modeling flow behavior of Ti-6Al-4V

The model described above is first applied to Ti-6Al-4V, the most widely used superplastic titanium alloy. Nearly all the industrial and the state-of-the-art of titanium SPF is

based on this alloy [9]. In general, there are two phases in this alloy: α (H.C.P. structure) and β (B.C.C. structure). Depending on the processing conditions, the relative amount of each phase can vary from 0 to 100 %. In order to model any dual-phase material, the fitting parameters a_l, a_s and σ_* have to be determined. This was done by applying the model to the (α+50% β) Ti-6Al-4V alloys. Hamilton [9] has reported the experimental results for (α+50%β) alloys with various grain sizes (6.4–20 μm) at 1200 K. In our model, the known parameters are Q_L=150 KJ/mol, $Q_B = 97$ KJ/mol and $r = 1.38e$-6 for α phase and Q_L=153 KJ/mol, $Q_B = 153$ KJ/mol and $r = 9.38e$-10 for β phase respectively [8]. n is taken as 4.4 for both phases as suggested for titanium alloys under the condition of dislocation climb control [8]. The remaining material constants a_l, a_s and σ_* are matched as a_l=8.0e-7, a_s=5.0e0 and σ_*=0.03 MPa based on experimental data and the model. With these materials constants, the overall agreement between the prediction and experimental counterparts for the two phases is reasonable, as shown in Figure 3.2. *It should be noted that the simulation is done by merely inputting the required grain size value in equation (3.14) and using the same materials constants (including σ_*) for all grain sizes.* This demonstrates that the model is able to predict the mechanical behavior of dual-phase superplastic materials with only a limited number of experimentally determined constants.

This model is further applied to study the temperature effect on the $\sigma - \dot{\epsilon}$ relations of ($\alpha + \beta$) Ti-6Al-4V alloys. It is well known that the concentration of the β phase generally increases with temperature, and therefore the phase ratio can change with temperature [9]. The experimental data of $\sigma - \dot{\epsilon}$ relations in Ti-6Al-4V alloys are available at temperatures 1120 K (with 76% α phase), 1145 K (with 70% α phase), 1197 K (with 60% α phase) and 1218 K (with 45% α phase) [9]. In order to model the temperature effect, the phase ratio is taken into account in our model by changing the ratio of numbers of grains for both phases (n_B/n_A). Using the same materials constants (except σ_*) obtained from the simulations of (α+50% β) alloys, the simulation are carried out for the four different temperatures. As shown in Figure 3.3, the predictions appears to be quite reasonable with the adjusting parameter σ_*. In agreement with the experimental observation of the aggregate threshold stress, the micro-level threshold stress (σ_*) used in the model was found to be dependent on temperature. Figure 3.4 shows the effect of temperature on the threshold stress in Ti-6Al-4V alloys. It is seen that the dependence of micro-level threshold stress on temperature can be expressed by a formulation similar to that given by Mohamed and Langdon [10] for aggregate threshold stress as

$$\sigma_* = B_* exp(\frac{Q_*}{RT}), \tag{3.21}$$

where B_* is a constant and Q_* is the activation energy at the slip plane level for micro-level threshold stress.

As mentioned earlier, the superplastic strain rate is accommodated by diffusional and dislocational movement of atoms. The relative contribution of each of these processes can be studied by computing the ratio of strain rate of each of the processes to the total strain rate, expressed as percentage. Let $\dot{\epsilon}_{diff}$ represent the total diffusional contribution towards the total strain rate $\dot{\epsilon}_{sp}$. $\dot{\epsilon}_{diff}$ can be computed from equation (3.14) by summing over all possible slip systems for all grains (phases). Similarly $\dot{\epsilon}_d$, the dislocational contribution

to the strain rate, can be calculated from equation (3.15). Figure 3.5 shows the relative contributions of diffusion and dislocation accommodations in (α+50% β) Ti-6Al-4V alloy. As can be seen from the results, the diffusion contribution to the strain rate is dominant at low strain-rate regions. The dislocational contribution becomes significant as the strain rate increases.

3.3.2 Modeling the flow behavior of Zn-22%Al

The model is also applied to Zn-22%Al alloy for the study of temperature effect on the σ-$\dot{\epsilon}$ curves. The thermo-mechanical property of this material at 423K, 473K and 503K has been reported by Mohamed et al [11]. The two phases in Zn-22%Al alloy that result from the eutectoid reaction are: α-Zn phase (H.C.P. structure) and α-Al phase (F.C.C. structure). The known constants in the model are Q_L=91.7 KJ/mol, Q_B =60.5 KJ/mol, r= 3.30e-9 and n=4.5 for α-Zn phase and Q_L=142 KJ/mol, Q_B = 84 KJ/mol, r = 9.71e-10 and n =4.4 for α-Al phase respectively [7]. To obtain the fitting parameters (a_l, a_s and σ_*), the numerical simulation is carried out for the temperature at 473K and grain size at 2.5 μm. The material constants (a_l=5.0e-2 and a_s=2.0e4) and σ_*=1.0 Mpa (temperature dependent parameter) are obtained which best fit this set of experimental data. The numerical simulation is subsequently carried out for other temperatures by varying only the threshold stress, σ_* and keeping a_l and a_s as constants. The simulation results compared with the experimental data are shown in Figure 3.6. It is seen that the model has predicted successfully both the shape and values of the σ- $\dot{\epsilon}$ curves. As in the Ti-6Al-4V case, the micro-level threshold stress (σ_*) in Zn-22%Al is a temperature-dependent parameter, and the dependence of micro-level threshold stress on temperature can be expressed by a similar formulation given by equation (15), as shown in Figure 3.7.

The sigmoidal curves shown in Figure 3.6 is usually divided into three regions based on the strain-rate sensitivity m, defined as the slope of the curve, i.e., $d(log\sigma)/d(log\dot{\epsilon})$. As can be seen from the figure, m continuously varies throughout the regions, with a maximum value of m occurring in region II (superplastic region). Region I and region III, at the lowest and highest ranges of $\dot{\epsilon}$ respectively, exhibit low values of m. Figures 3.8 compares the computed m curves at T= 423 K and T= 503 K. As can be seen from the figure, both m curves have the expected bell shape. At higher temperature, the maximum m occurs at higher strain rate. Most of the phenomenological models [e.g.12] attempt to model only region II, and hence m vs. $\dot{\epsilon}$ will be a horizontal line (corresponding to $1/n$), contrary to experimental observations.

3.4 Summary and Conclusions

A micromechanical model based on grain-level diffusion and dislocation has been extended to characterize the dual-phase superplastic deformation process. The material constants a_l and a_s are evaluated from a single set of experimental data, while threshold stress

(σ_*) is temperature dependent but grain size independent. The model is successfully applied to two-phase Ti-6Al-4V and Zn-22Al materials. The flow stresses as a function of temperature and grain size and strain rate sensitivity (m) are predicted for a wide range of strain rates. The threshold stress (σ_*) introduced to the diffusional flow at slip system level manifests as experimentally observed threshold stress at the macro level, and was found to be strongly dependent on temperature. The diffusion contribution to the strain rate is dominant at low strain-rate regions, while the dislocational contribution becomes significant as the strain rate increases in both the material systems.

REFERENCES

1. J. Pilling and N. Ridley, *Superplasticity in Crystalline Solids*, The Institute of Metals, London, UK, 1989.

2. K. Murali and N. Chandra, *Acta Metall.*, 43, 1783 (1995).

3. N. Chandra and K. Murali, *Scripta Mater.*, 32, 1429 (1995).

4. N. Chandra, J. Rama and P. Dang, *Mater. Sci. Eng. A*, 134, 231 (1997).

5. N. Chandra and P. Dang, *Scripta Metall.*, 36, 1327 (1997).

6. T. G. Langdon, *Mater. Sci. Eng.*, A174, 225 (1994).

7. M. F. Ashby and R. A. Verrall, *Acta Metall.*, 21, 149 (1973).

8. H. J. Frost and M. F. Ashby, *Deformation-Mechanism Maps*, Pergamon Press, Oxford, 1982.

9. C. H. Hamilton, in *Superplastic Forming*, ed. by S. P. Agrawal, ASM, Metals Park, Ohio, 13 (1995).

10. F. A. Mohamed and T. G. Langdon, *Acta Metall.*, 23, 177 (1975).

11. F. A. Mohamed, M. M. I. Ahmed and T. G. Langdon, *Metall. Trans.*, 8A, 933 (1977).

12. O. D. Sherby and J. Wadsworth, Superplasticity in Metals, Ceramics, and Intermetallics, *MRS Symposium Proceedings*, ed. by M. J. Mayo, M. Kobayashi and J. Wadsworth, Materials Research Society, Pittsburgh, PA, 196, 3 (1990).
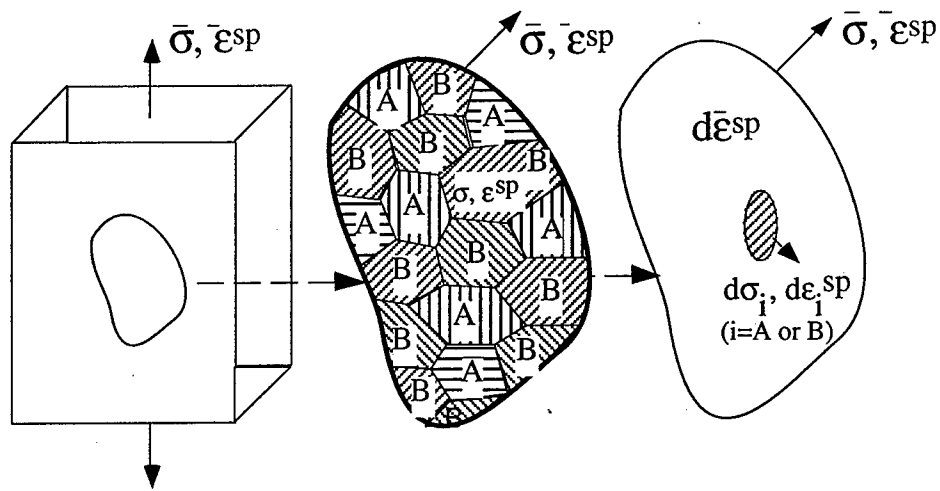
Figure 3.1: Dual-phase polycrystalline model based on the self-consistent relation.
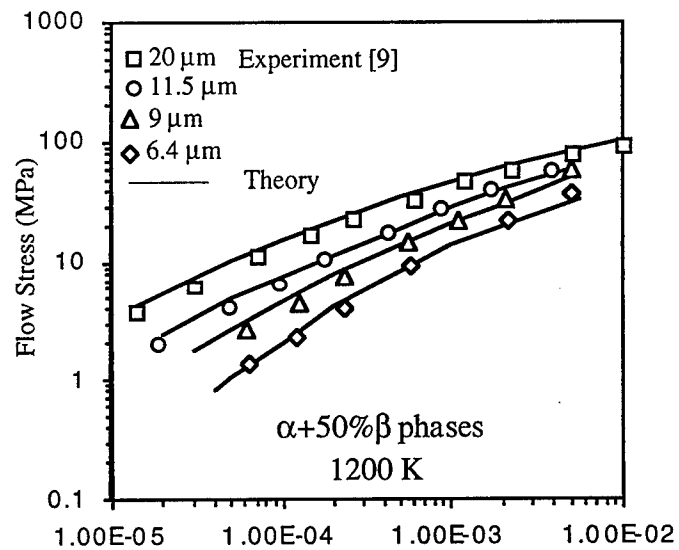
Figure 3.2: Prediction and experimental comparison of grain size effect on the flow behavior of $Ti - 6Al - 4V$ alloy.
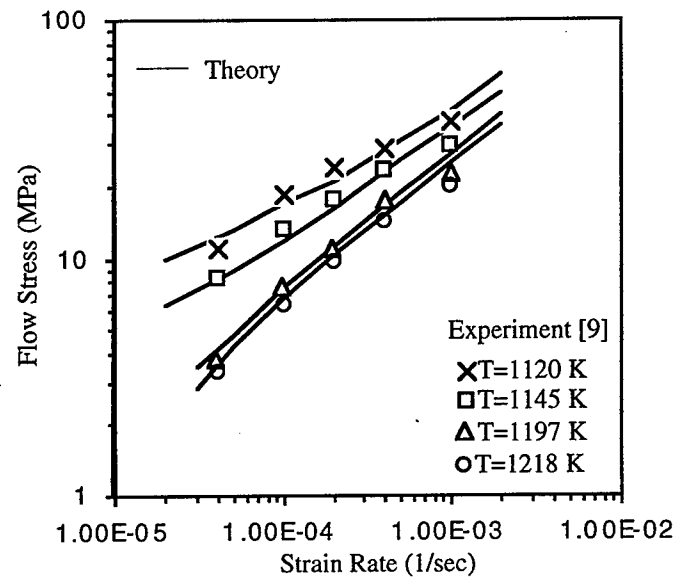
Figure 3.3: Prediction and experimental comparison of temperature effect on the flow behavior of $Ti - 6Al - 4V$ alloy.
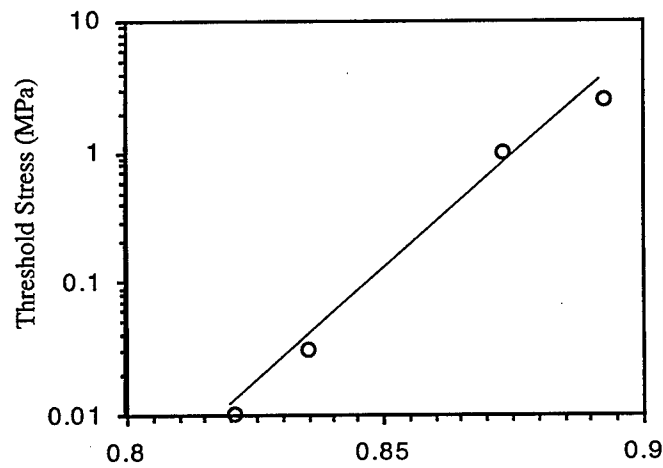
Figure 3.4: Dependence of micro-level threshold stress on temperature in $(\alpha + 50\% \ \beta)$ $Ti - 6Al - 4V$ alloy.
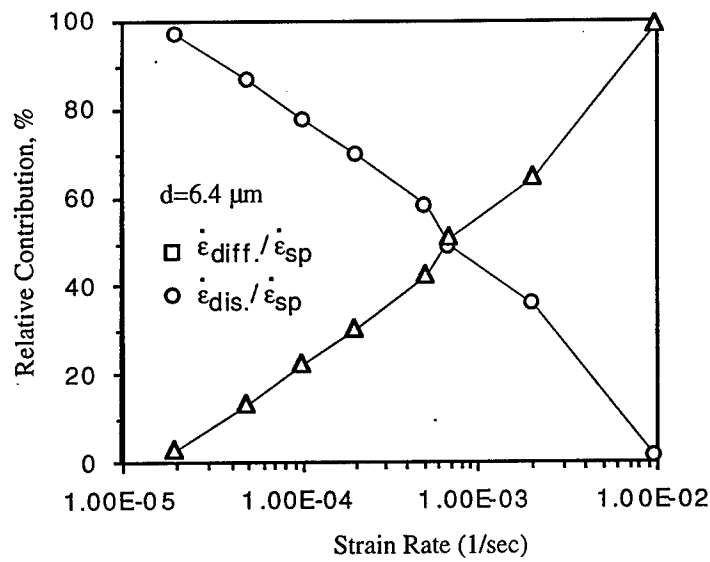
Figure 3.5: Relative contribution to the strain rate in $(\alpha + 50\% \beta)$ $Ti - 6Al - 4V$ alloy.
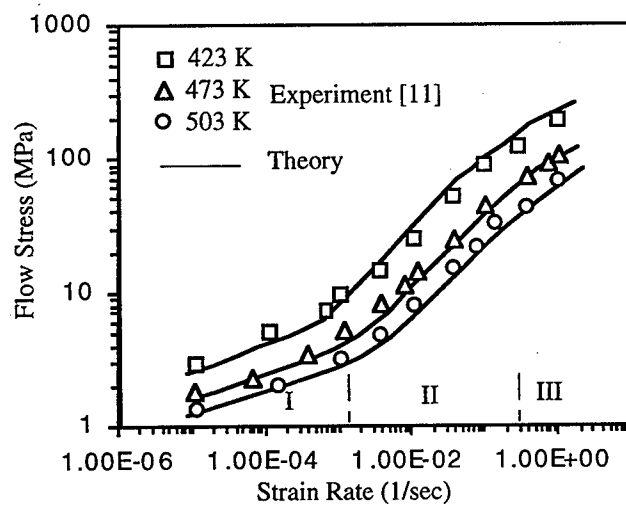
Figure 3.6: Theoretical prediction of the flow stress-true strain rate behavior of $Zn - 22Al$ alloy.
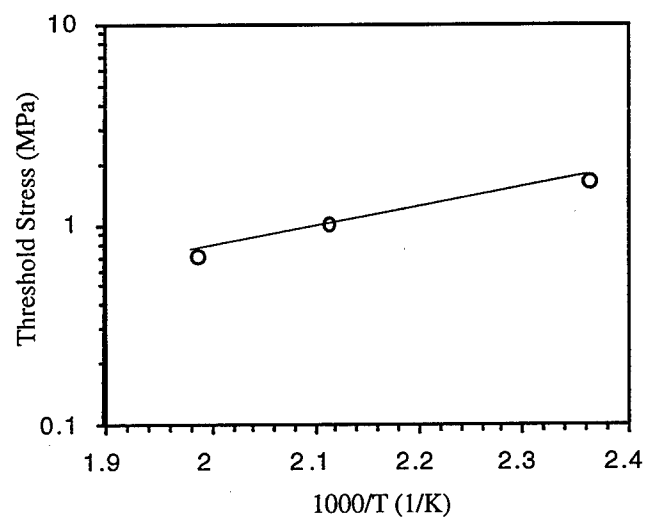
Figure 3.7: Dependence of micro-level threshold stress on temperature in $Zn - 22Al$ alloy.
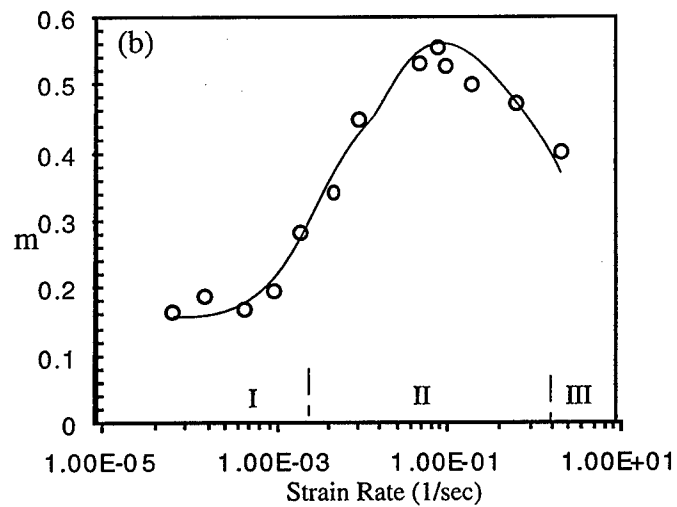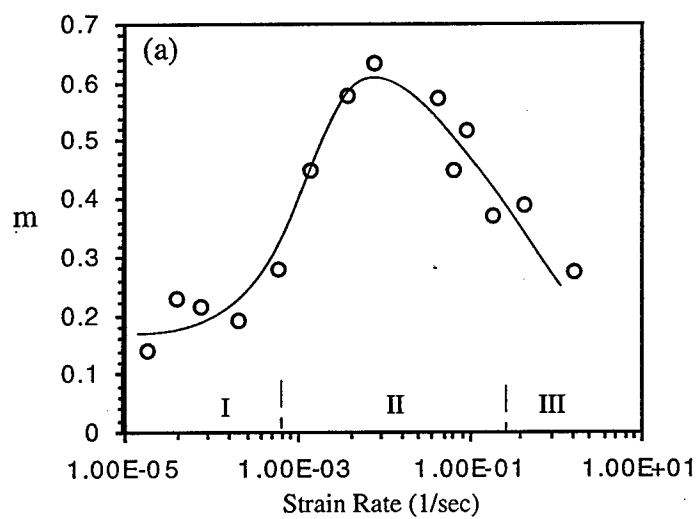
Figure 3.8: Prediction of the strain rate sensitivity m in $Zn - 22Al$ alloy at (a) 423 K and (b) 503 K.

Chapter 4

Atomistic Simulation of Grain Boundary Sliding and Migration

4.1 Introduction

Despite the important role of grain boundaries (GB) in influencing materials properties, such as superplasticity [1], our knowledge of how boundaries actually move at the microscopic level is limited. Much of the difficulty is due to the lack of a suitable means of observing the dynamical process (such as sliding and migration) with sufficient spatial and time resolution. One approach that has provided atomic-level insights in GB in metals is atomistic simulations. As an effective alternative, atomistic simulations are being increasingly used due to the availability of atomistic models and the advent of powerful computers. Though considerable work [2-15] has been done in recent years to study the equilibrium structures of grain boundaries using atomistic simulations, very limited research has focused on the atomistic simulation of grain boundary sliding (GBS) and migration. Yip and coworkers [16-18] studied grain boundary migration and sliding due to high temperature effect using pair-like potentials. They observed both migration and sliding purely due to the applied temperature. In general, however, the driving force for grain boundary movement is the internal strain and stress field [10]. Unfortunately there are very few studies having been done on grain boundary mobility under applied strains or stresses at atomic level. Very recently Molteni et al. [19] conducted an ab initio simulation of grain boundary sliding in germanium in a quasi-static way, by applying constant strain increment to one crystal of the bi-crystal boundaries. The problem with applied strain instead of stress is, as we will see in the present work, that the migration process is prevented. Such a preconstrained process experiences much larger energy barrier than a coupled sliding and migration process.

The main purpose of this paper is to understand the mechanics of deformation of grain boundaries at the atomic level. In order to achieve this, we have first studied the structure and energy of the STGB of aluminum. Based on the equilibrium structure we applied displacements and forces on one of the grain to simulate grain boundary deformation

(sliding and migration). The paper is organized as follows: In section 2, the atomistic simulation methods and the interatomic potentials were first introduced. The equilibrium structure and energy of 17 [110] tile grain boundaries in aluminum were then studied using molecular statics simulations and EAM potential functions. These boundaries were described by coincident site lattice (CSL) with misorientation angles range from 0 to 180 degree. In section 3, based on the equilibrium GB structures obtained in Section 2, grain boundary mobility (sliding and migration) was then simulated under both applied displacement and applied force conditions. The mechanics (stress, displacement and energetic fields) associated with applied displacement and applied stress were examined to elucidate the importance of coupled sliding and migration process.

4.2   Equilibrium Grain Boundary Structures and Energies

Molecular statics and molecular dynamics are used in performing atomistic simulations. Molecular statics is used in determining the equilibrium positions of atoms in a crystal, by minimizing the total energy of the crystal at 0 K. Molecular Dynamics is used to study the time-related phenomena for crystals subjected to external forces. A DYNAMO program developed at the Sandia National Laboratory Livermore [21] incorporated with the EAM model is used in this work. It has been proven that EAM potentials are more reliable in representing atomic interactions in metallic systems [11-15] than traditional pair potentials. The main limitation of the pair potential models is that they fail to take into account the metallic bonds, i.e. coordinate-dependent or many body interactions, while EAM potentials include in an implicit way the many-body effects. The analytical EAM functions developed by Oh and Johnson [20] will be adopted in this work.

Since GBS and GB migration are the interest of this work, grain boundaries are modeled as planar bicrystalline high-angle structures specified by coincident site lattice (CSL) models. High-angle grain boundaries (misorientation angle $\theta > 15^o$) are associated with higher grain boundary energy and are generally thought to promote GBS [1]. CSL grain boundaries are found to naturally occur in all polycrystalline materials, and their frequency of occurrence is strongly dependent on the processing history [22]. As the consequence of the CSL model, the lowest-energy grain boundary structure for a given misorientation (characterized by Σ) is postulated to be the symmetrical configuration. Figure 4.1 illustrates the designations of symmetric tilt grain boundaries (STGB) used throughout this work. In this figure, the rotation axis [uvw] is perpendicular to the plane of the paper (z-direction), consequently, the grain boundary plane (hkl) is x-y plane with y-direction aligned to the grain boundary normal; and the misorientation angle θ is computed from the two [001] directions of each of the bicrystals. Grain boundaries are designated as [uvw] Σ N (hkl), thus the grain boundary shown in Figure 4.1 describes [110] $\Sigma3(1\bar{1}1)$ tilt boundary.

In this work, we examined 17 tilt [110] CSL boundaries: $\Sigma3(1\bar{1}1)$, $\Sigma3(1\bar{1}2)$, $\Sigma9(2\bar{2}1)$,

$\Sigma 9(1\bar{1}4)$, $\Sigma 11(1\bar{1}3)$, $\Sigma 11(3\bar{3}2)$, $\Sigma 17(3\bar{3}4)$, $\Sigma 19(3\bar{3}1)$, $\Sigma 27(1\bar{1}5)$, $\Sigma 27(5\bar{5}2)$, $\Sigma 33(2\bar{2}5)$, $\Sigma 33(4\bar{4}1)$, $\Sigma 33(1\bar{1}8)$, $\Sigma 41(4\bar{4}3)$, $\Sigma 43(5\bar{5}6)$, $\Sigma 43(3\bar{3}5)$ and $\Sigma 51(5\bar{5}1)$. For each of the CSL boundaries, the computational crystal was generated based on the orientation of a given grain and the symmetry between that and the adjacent grain across the boundary plane. Due to the fact that multiple energy minima may exist with very similar energies and very different atomic structures [6], it may be necessary to obtain lower-energy states by removing (or adding) atoms from the boundary plane during construction of the initial unrelaxed structures. Since grain boundaries are extended defects in two dimensions, but inhomogeneous in the direction normal to the grain boundary plane, it is usual to construct a computational crystal that is periodic only in 2-D plane of the interface (x- and z- directions in this work). In the grain boundary normal direction (y-direction), free-surface boundary conditions are imposed. Consequently, the crystals are designed to be large enough in y-direction to remove the free surface effects on the grain boundary structure. The computational crystals used in this work contain about five thousand atoms.

Figure 4.2 shows the final equilibrium structures of selected grain boundaries obtained using molecular statics simulations. It should be noted that only a portion of the whole computational crystal close to the grain boundary is shown. The open and filled circles represent atoms in two adjacent (110) atomic layers, which have been projected in a plane normal to z=[110] direction. It is observed that during the simulation process, most of the atomic movement occurs near the grain boundary plane (in the relaxed state) compared to the initial unrelaxed configurations. Associated with the atomic rearrangement that occurs upon minimization of the grain boundary energy is a relative displacement of grains in the direction perpendicular to the GB plane, Δy^* (see Figure 4.1). Δy^* is one measure of the GB expansion or excess volume per unit GB area [23]. This measurement, if made far away from the GB, is not sensitive to the GB strain field, which decays away from the boundary as ye^{-y} [23], where y is the distance from GB. Table 1 shows a measure of the GB expansion is the relative y displacement of two atomic planes closest to the GB (i.e. the pair of plans with the largest spacing after relaxation). It is seen that the local grain boundary expansion ($\Delta y^* > 0$) is apparent for all the boundaries. It is also seen from the data that the lower Δy^* in general corresponds to a lower GB energy configuration. The equilibrium configurations shown in Figure 4.2 were compared to other available computational and experimental results. The key aspect to be compared is the micro-facet structural details near the boundary which includes the relative positions of atoms in the boundary and neighboring planes. The present results for two of the CSL structures $\Sigma 9(2\bar{2}1)$ and $\Sigma 11(1\bar{1}3)$ agree well with the experimentally observed tilt boundaries using high-resolution transmission electron microscopy (HRTEM) [7, 11, 15].

The distribution of energy across the equilibrium grain boundaries is next computed. Figure 4.3 shows the energy associated with atoms as a function of distance from the grain boundary plane (x-axis zero being at the grain boundary). The energy increases as the grain boundary is approached from either side of the bicrystal. There is significant variation in the energy levels for the different boundaries considered. The width of the grain boundary can be defined when the energy of atoms equals to the value of energy in a perfect crystal (-3.58

eV for aluminum). By this definition, the width of grain boundaries varies with different boundary structures (see Figure 4.3), from a maximum 10 $\overset{o}{A}$ to almost zero in $\Sigma3(1\bar{1}1)$ structure.

The energy of the individual atoms (plotted in Figure 4.3) can be used in the evaluation of grain boundary energy, which is equal to the energy of atoms within the width of the grain boundary in the defective system less than that for the perfect crystal, divided by the area of the grain boundary plane. Figure 4.4 (a) shows the grain boundary energy (E_{gb}) for all the tilt grain boundaries studied in this work, plotted as a function of the misorientation angle θ. As can be seen from the plot, three energy cusps for "special" angles are observed in this work, which correspond to three twin boundaries: $\Sigma3(1\bar{1}1)$, $\Sigma3(1\bar{1}2)$ and $\Sigma11(1\bar{1}3)$.

Our simulation result is reasonably consistent with the experimental result conducted by Otsuki and Mizuno [22], as shown in Figure 4.4 (b). The evidence for the existence of all the three energy cusps is shown though the $\Sigma3(1\bar{1}2)$ is not so apparent. Comparing these two sets of results, besides the excellent agreement of the shape of the energy vs. misorientation plots, the absolute value are also in a close range. Wolf [2, 13] and Hasson et al. [5] have conducted similar grain boundary simulations for copper and aluminum using pair potentials. However, they only observed energy cusps for the $\Sigma3(1\bar{1}1)$ and $\Sigma11(1\bar{1}3)$ orientations but not for the $\Sigma3(1\bar{1}2)$ orientation. Since $\Sigma3(1\bar{1}2)$ is also a twin boundary it is reasonable to expect the $\Sigma3(1\bar{1}2)$ boundary to be also a low-energy defect. The observation of the new low energy configuration $\Sigma3(1\bar{1}2)$ can be ascribed to the use of EAM potentials in this work compared to the pair potentials used in the earlier works. In the EAM calculations, the configuration energy is composed of a simple pair interaction term plus an "embedding" function which specifies the dependence of energy on local coordination. The ability to treat deviations in local coordination has been shown to be crucial in obtaining reasonable agreement with the relaxation at interfaces and free surfaces. Thus atoms interacting across the interface experience an electron density different from that of atoms interacting with each other on the same side of the interface. This intrinsically anisotropic character of the atoms near the interface is not taken into account by any pair potential. In general, the choice of interatomic potentials has less effect on grain boundary structures than on grain boundary energies [2, 11].

4.3 Grain Boundary Sliding and Migration

Molecular statics/dynamics simulation is next performed to study grain boundary mobility under applied displacement and forces, as shown in Figure 4.5. The computational crystal composed of about 5000 atoms with approximate 35 atomic layers (in y-direction) in each grain. In order to eliminate the effect of free surfaces associated with the grain boundary plane during the grain boundary sliding, periodic boundary conditions were applied in plane of the interface (i.e. x- and z- directions in this work). When applying displacement,

specified levels of incremental displacements are applied to each of the atoms in the top grain and all the atoms in the bottom grain remain free. It is adequate to use free-surface boundary conditions in the grain boundary normal direction (y-direction). When forces are applied on all the atoms in the top grain, it simulates the actual motion of the top grain as a single unit over the bottom grain. In this case, it is necessary to restrict the motion along the two surfaces in y-direction, which is achieved by setting y-displacement to zero on the atoms near the upper surface (four outmost layers in y direction) and fixing the bottom surface (four outmost layers in -y direction). These boundary conditions assure the molecular dynamics simulation were performed at a constant volume condition. As will be evident later, application of displacements and force yield different responses; displacement causes "pure" GBS whereas force induces sliding and migration. For brevity, only the results for $\Sigma 3(1\bar{1}1)$ and $\Sigma 9(2\bar{2}1)$ were given and discussed below.

4.3.1 Applied Displacement

Under the applied displacement conditions, grain boundary migration (atomic movement in the direction normal to the applied displacement direction) was virtually constrained. A "pure" GBS process is thus implemented by applying constant displacements, each increment followed by a complete relaxation (energy minimization) of the boundary structure. Since the CSL grain boundary structure studied in this work can be obtained by repeating the CSL cell in x- and z-directions, the structure with a displacement of a_{CSL} (a_{CSL} is the lattice parameter of the CSL cell in x-direction) is equivalent to the initial undisplaced structure under the periodic conditions described above. Therefore the total displacement in each case is limited to the value of a_{CSL} for the given grain boundary. The increments (described in percentage of a_{CSL}) are selected to be small enough ($2.5\% a_{CSL}$) to capture all the energy jumps. After each increment the configuration is relaxed to its local equilibrium state and the grain boundary energy is computed. The grain boundary energy profile associated with the GBS process then provides the tool necessary to predict the grain boundary mobility. Figures 4.6 and 4.7 give such results for two typical grain boundaries: a twin boundary $\Sigma 3(1\bar{1}1)$ and a $\Sigma 9(2\bar{2}1)$ boundary.

Figure 4.6 shows the energy profile of "pure" GBS process in $\Sigma 3(1\bar{1}1)$ twin structure. It is seen from Figure 4.6 that there are two energy peaks and a energy valley between them. The first peak occurs when the shear displacement is about 17% a_{CSL} (case II in the figure), where the atoms represented by open (and filled) circles are directly above the filled (and open) circles across the boundary. This configuration corresponds to a set of atoms in adjacent (110) planes displaced by d_{220} amount in the z-direction. When the shear displacement is about 66% a_{CSL} (case IV in the figure), the atoms across the interface plane are at positions directly facing each other, and furthermore these atoms facing each other are in the same (110) plane. It can be seen that open circle is the exactly above open circle (filled circle is exactly above filled circle). In case IV, the separation distances between atoms across the boundary is the smallest, and the corresponding energy value is the largest as seen in the energy plot. Between these two high energy states (cases II and IV), there is

an energy valley at the 33% a_{CSL} shear displacement (see case III). The atomic arrangement at this displacement forms a twin structure equivalent to the initial structure. Though the interface of the twin has shifted (from AA to BB) with d_{111} amount in the y-direction, this boundary has an energy equal to the initial twin structure. It is interesting to notice that though we intent to simulate "pure" GBS, a one-layer migration cannot be prevented for a specific displacement as shown in case III. This demonstrates the geometrical necessary of coupling between migration and sliding. This aspect will be discussed in details in section 3.3.

In the case of $\Sigma 9(2\bar{2}1)$ boundary shown in Figure 4.7, the energy barrier in the initial phase of the GBS process (from 0 to 52% a_{CSL}) is relatively small. A big energy jump appears when the atoms across the boundary face each other (52-58% a_{CSL} shear displacements, case II). After the short jump the GBS process proceeds easily. The atomic configuration corresponding to case II represents the worst stability of the grain boundary structure. Atoms across the interface plane in this case are at positions directly facing each other and in the same (110) plane (open circle is the exactly above open circle, and filled circle is exactly above filled circle). When comparing the GBS process in $\Sigma 9(2\bar{2}1)$ boundary with that in $\Sigma 3(1\bar{1}1)$ boundary, though the magnitude, width and distribution of the energy barriers are quite different for the two GB structures, the energy diagrams during the GBS show a general pattern: 1) The initial CSL structure and the final displaced structure with $100\% a_{CSL}$ displacement have the lowest energies, any structure between them have equal or high energies. GBS process destroys the CSL arrangement of the initial equilibrium grain boundary structure and increases the grain boundary energy; and 2) Energy jumps (energy barriers) occur when the displacement is such that some atoms in the two adjacent (hkl) planes across the grain boundary interface (one in each of the bicrystal) are directly above (or below) each other. As declared earlier, the (hkl) interplanar spacing (all less than $0.6a_e$) are substantially less than the nearest-neighbor distance in the perfect crystal ($0.707a_e$ in FCC structure), all atoms facing each other across the grain boundary interface repel each other. In the configurations with energy peaks, some atoms across the interface are too close to each other and hence have very high energies.

4.3.2   Applied Forces

To study grain boundary mobility under applied force conditions, a force of specific value (ranging from 0.01 to 0.04 eV/$\overset{o}{A}$) is applied in the x direction (to the right) on the atoms in upper-half of the bicrystals. Figure 4.8 shows the simulation result for $\Sigma 3(1\bar{1}1)$ twin boundary. It can be seen that applied forces cause relative motion across the boundary between two grains leading to GB sliding. This is evident from the relative position of atoms numbered R, 1 and 2. Atom R is in the bottom grain, atom 1 is on the GB and atom 2 in the top grain away from the boundary. It should be noted that the periodic boundary condition fills in new atoms from the left as atoms slide to the right of the computational crystal. Apart from sliding, GB also migrates, i.e. the interface that forms the boundary

between two grains moves perpendicular (in y-direction) to the original GB plane. Such motion can be observed at 2 ps where the GB interface has moved one atomic layer (dotted line), and by about 3 atomic layers at 5 ps (see Figure 4.8).

To get a quantitative understanding of the grain boundary sliding, the average x-displacement of atoms lying along y axis are plotted in Figure 4.9. As seen from this figure, the displacement field shows a sharp discontinuity across the interface indicating relative motion of atoms across the boundary resulting in GB sliding. The figure also shows that the magnitude of GB sliding increases with time. Thus Figure 4.9 (showing sliding) and Figure 4.8 (showing migration and sliding) demonstrate that sliding and migration are coupled in this system.

GB energy during the deformation process is plotted as a function of time in Figure 4.10. This figure indicates that the energy continuously varies with a few peaks and valleys, which corresponds to the evolving GB structure during the deformation. For example a peak is observed at 1.5 ps because the atoms in the layer just above the interface directly face the atoms in the interface (see also Figure 4.8 at 1.5 ps). In this case, the interplanar spacing in y-direction ($0.577a$) is substantially less than the equilibrium nearest-neighbor distance in the perfect crystal ($0.707a$ in FCC structure). This occurs since the atoms facing each other across the grain boundary are too close to each other and hence repel each other. Several energy valleys (at 2, 3.5 and 5 ps) correspond to new twin configurations (with different interface positions). However, as shown in Figure 4.10, their energies are still much higher than the energy of stress-free twin structure (0 ps).

Similar process was observed in $\Sigma 9$ grain boundary, as shown in Figure 4.11. Due to its incoherent interface and higher grain boundary energy, the initial grain boundary sliding appears earlier than that of $\Sigma 3$ case. The migration distance at each step is shorter due to the smaller d_{221} interplanar spacing in y-direction of this boundary. The sliding occurs first (Figure 4.11, 0.5 ps); When the sliding displacement in x direction reaches d_{114}, the grain boundary interface migrates one atomic layer (d_{221}) up along y direction (Figure 4.11, 1 ps). Thus coupled sliding and migration process appears very similar to that in $\Sigma 3$ case. However, as also shown in Figure 4.11, the change in grain boundary energy during the simulation process is very different. In contrast to $\Sigma 3$ case, the energy barrier in this case is much smaller (about $0.1 \times 10^{-2} eV/\overset{o}{A}^2$). It is therefore to be expected that the GBS and GB migration are much easier in the $\Sigma 9$ (high energy GB) than that of $\Sigma 3$ (low energy twin GB).

4.3.3 Comparison Between Applied Displacement and Applied Stress Conditions

From the foregoing discussions, it is clear that in STGB, when forces are applied GB sliding is always accompanied by grain boundary migration and they are proportional to each other. Such coupled process has been observed by Ashby [25] based on the bubble raft

model and by Bishop et al. [17, 18] based on purely geometric considerations for STGB. This coupling process is of practical importance, and hence examined from geometry, energy and stress field considerations in the following sections.

Geometrical Consideration of Coupled Sliding and Migration

For understanding the geometrical aspects of coupling migration with sliding, it is easier to analyze the motion in terms of displacement shift completed (DSC) lattice vectors. Translations of one crystal with respect to another by a DSC lattice vector (the finer mesh in Figure 4.1) restore the coincidence pattern, although the coincidence sites will shift to a different location. This GB shift corresponds to the GB migration. For example, $\Sigma 3(1\bar{1}1)$ boundary has following DSC lattice parameters: $a_{DSC} = 1/3a_{CSL} = d_{112}$, $b_{DSC} = 1/3b_{CSL} = d_{111}$ and $c_{DSC} = c_{DSC} = d_{110}$. When the relative translation of the crystals is a_{DSC} in the x direction, the boundary migrates by b_{DSC} in the y direction. The CSL structure is reestablished one unit away in the y direction. The ratio (R) of migration distance (M) to sliding displacement (U) is

$$R = \frac{M}{U} = \frac{b_{DSC}}{a_{DSC}} = \epsilon tan\frac{\theta}{2} \qquad (4.1)$$

Here the misorientation angle θ is defined as the angle between the two [001] directions of each of the bicrystals (see Figure 4.1), ϵ is a integer whose value depends on the details of geometry. Equation (1) is valid for all symmetric tilt boundaries as pointed out by Ashby [25]. It should be noted that this geometric argument is truly valid only for STGB [18]. However, it does not preclude coupling to occur in other types of boundaries.

In the applied displacement case, after a displacement of a_{DSC} to the top grain, GB moves by b_{DSC} (see III in Figure 4.6). However, when the displacement is further applied (including layer BB), GB interface moves back to the original position (line AA). When forces are applied, GB migrates upwards continuously after each a_{DSC}. This difference will be clear from energy consideration discussed below.

Energetic Consideration of Coupled Sliding and Migration

The energy necessary to couple sliding and migration can be readily seen by comparing the grain boundary energy profiles shown in Figures 4.6 and 4.10 for $\Sigma 3(1\bar{1}1)$ boundary and Figures 4.7 and 4.11 for $\Sigma 9(2\bar{2}1)$ boundary. Let us first consider $\Sigma 3(1\bar{1}1)$, i.e. Figures 4.6 and 4.10. The initial energy profiles in both cases (0-40%a_{CSL} displacement in Figure 4.6 and 0-2ps in Figure 4.10) are similar. This indicates that the deformation processes are same at this stage regardless of whether force or displacement is applied. Also, when the structures are examined it is seen that the grain boundary shown in Figure 4.10 only experienced GBS without migration similar to Figure 4.6, leading to the two energy profiles being very similar. However, the energy profiles are very different in the subsequent stages. The results

shown in Figure 4.10 (applied force) confirm that when sliding is accompanied by migration, boundary structure never passes through a highly perturbed configuration (e.g. Case IV in Figure 4.6). By virtue of the coupling between sliding and migration, the energy barrier for grain boundary motion is greatly reduced from about $2.5 \times 10^{-2} eV/\overset{o}{A}^2$ in Figure 4.6 to $0.5 \times 10^{-2} eV/\overset{o}{A}^2$ in Figure 4.10. Simulation of a perfect crystal with the same orientation as shown in in Figure 4.6 indicated that an peak energy of $9.3 \times 10^{-2} eV/\overset{o}{A}^2$ is required to displace one portion of the crystal against the other. This indicates that the high energy peak in Figure 4.6 (applied displacement) corresponds to sliding in a less defect region (line AA) rather than along the new GB interface (line BB). The effect of coupled sliding and migration on energy is more obvious in $\Sigma 9(2\bar{2}1)$ boundary, where the energy barrier is dropped from about $3.5 \times 10^{-2} eV/\overset{o}{A}^2$ in Figure 4.7 to $0.1 \times 10^{-2} eV/\overset{o}{A}^2$ in Figure 4.11. This results indicate that the high energy state during the pure GBS (e.g. Figure 4.9 II) is never reached in the coupled GBS and migration process.

Displacement and Stress Fields of Coupled Sliding and Migration

In the applied force conditions, both the sliding and migration displacement fields are directly related to the magnitude of applied force, and also affected by the grain boundary structures themselves. Figure 4.12 shows the displacement field changes under three levels of applied forces for $\Sigma 3(1\bar{1}1)$, and Figure 4.13 shows the data for $\Sigma 9(2\bar{2}1)$. The sliding displacements were computed from the relative position of two grain across the interface (see Figure 4.9). The migration displacements were the difference in y-direction between the positions of new interface and the original equilibrium position of the interface. As can be seen from these two figures, as the applied force increases (from 0.01 to 0.04 $eV/\overset{o}{A}$), both the sliding and migration displacements increase but in quite a different fashion. Sliding displacements increase monotonically with time. Migration displacement increases in steps, each step indicating that the interface has migrated one atomic layer along the y-direction. However, the sliding and migration are coupled and proportional, and anything which inhibits sliding also inhibits migration.

It is also noted from Figures 4.12 and 4.13 that the structure of the grain boundary has great influence on GBS. To understand this effect, we examined the GBS displacement for four different grain boundaries with increasing energy levels under same total applied force per unit volume. The consolidated displacement (sling and migration) vs. GB energy response are shown in Figure 4.14. It is clearly seen that GBS displacement is proportional to the grain boundary energy associated with a given structure. For example, at 5 ps, $\Sigma 3(1\bar{1}1)$ boundary slides 3.3, 5.5 and 7.2 angstroms at applied forces 0.58, 1.17 and 2.32 (in unit of $\times 10^{-3} eV/\overset{o}{A}^4$ per volume) respectively, while $\Sigma 9(2\bar{2}1)$ slides 5.9, 7.4 and 8.5 angstroms under the same levels of applied forces. These results are consistent with the energy profile during the simulation (Figures 4.10 and 4.11), that is, higher energy boundary such as $\Sigma 9(2\bar{2}1)$ has lower energy barriers for grain boundary movements and hence produces more sliding and

45

migration displacements. Though it is tempting to write that grain boundary displacement u_d and migration u_m is proportional to GB energy E_{gb}, we need to understand energy and stress distribution across the GB plane in three dimensions.

In order to analyze the internal stress fields resulted from the applied force and applied displacement, the $\alpha\beta$ components of the local stress tensor $\sigma^i_{\alpha\beta}$ associated atom i is calculated as follows:

$$\sigma^i_{\alpha\beta} = \frac{1}{V} \sum_{j, i \neq j} (F'_i \rho'^\alpha_j + F'_j \rho'^\alpha_i + \phi'_{ij}) \frac{r^\alpha_{ij} r^\beta_{ij}}{r_{ij}} \quad (\alpha, \beta = 1, 2, 3) \tag{4.2}$$

where V is the volume of the computational crystal, r^α_{ij} the αth component of the relative position vector of atom i and j and F'_i, ρ'_j and ϕ' are the derivations of the EAM functions (details given in Ref. [12]). For brevity, only the results of $\Sigma 3(1\bar{1}1)$ is given and discussed below.

Figure 4.15 shows the local stress field near the grain boundary (σ_{11}) for the atomic configurations under applied displacement (Figure 4.6, case IV) and applied force (Figure 4.8, 5 ps). The lengths of the arrows in Figure 4.15 initiate at the atomic positions and scale with the magnitude of the local stresses and the direction of the arrow shows the sign of the local stresses. It is to be noted that due to the use of the periodic boundary conditions, the stresses are same for all the atoms that reside in the same atomic layer in the y-direction. In the applied displacement case (Figure 4.15 a), the stresses are much higher in the grain boundary region. In the applied force case (Figure 4.15 b), the stresses are more uniformly distributed around the GB interface. σ_{11} changes direction across the interface indicating the presence of large shear stresses necessary for force equilibrium. This shear stress opposes GBS motion.

Finally, in order to understand the relations between the internal stress and external applied force, the overall stress distribution for the whole computational crystal was computed. Figure 4.16 shows the results of $\Sigma 3(1\bar{1}1)$ at the applied force of 0.04 eV/$\overset{o}{A}$. As the simulation proceeds, the internal stresses were build up and increases gradually. The σ_{11} stress discontinuity was found in the region close to the interface, indicating the shear resistance to the grain boundary movements. The integration of the stress (times the distance from the interface) across the whole computational crystal was calculated and normalized to the internal force to one atom. This normalized force has values (in unit of eV/$\overset{o}{A}$) of 0.0027 (at 1 ps), 0.0031 (at 2 ps), 0.0091 (at 3 ps), 0.015 (at 4ps), 0.028 (at 5 ps), 0.031 (at 8ps) and 0.029 (at 10 ps) at corresponding simulation times. It is seen that as the simulation time increases, the integration of the stress (i.e. the force) increases towards to the value of applied force (0.04 eV/$\overset{o}{A}$). Lack of static force balance, indicates transient conditioning in which a state of dynamic equilibrium is present. The external forces do match at 8 ps, when the internal stress distribution induced resistive forces. It is thus clear from the stress distribution that the relative displacement is restricted to a small region around the interface, and is proportional to the energy associated with the GB interface.

Summary

46

Interatomic potentials using Embedded Atom Method (EAM) are used in conjunction with molecular statics and dynamics calculations to study the sliding and migration of (110) symmetric tilt grain boundaries (STGB) in aluminum, under both applied displacement and force conditions. Three low energy configurations (corresponding to $\Sigma3(1\bar{1}1)$, $\Sigma3(1\bar{1}2)$ and $\Sigma11(1\bar{1}3)$ twin structures) are found in the [110] STGB structures when grain boundary energies at 0 K are computed as a function of grain misorientation angle. *"Pure"* GBS without migration is implemented by applying external displacement. The propensity for *"pure"* GBS is evaluated by computing the energy associated with incremental equilibrium configurations during the sliding process, and the magnitude of the energy barriers is found to be much higher than that with migration. In contrast, in the applied stress conditions, the energy barriers are reduced due to the fact that grain boundary sliding of STGB is always coupled with apparent migration. Thus the study clearly shows that in these special grain boundaries(STBGs), migration is coupled with sliding during GBS. It is seen that when the free energy in the grain boundary decreases (more specialized boundaries approaching twin boundaries), the boundary offers more resistance to sliding and, consequently, migration. The computational results indicate that if we can engineer grain boundary, we can decrease the GB energy to decrease deformation rate (e.g. creep resistance) and increase GB energy to promote sliding (e.g. superplasticity).

REFERENCES

1. T. R. McNelly and M.E. McMahon, Mater. Trans. A, 27 (1996) 2252.
2. D. Wolf, Acta Metall., 32 (1984) 245.
3. Y. OH and V. Vitek, Acta Metall., 34 (1986) 1491.
4. D. Wolf, Acta Metall., 32 (1984) 245.
5. G. Hasson, J. -Y. Boos, I. Herbeuval, M. Biscondi and C. Goux, Surf. Sci., 31 (1972) 115.
6. G. J. Wang, A. P. Sutton and V. Vitek, Acta metall., 32 (1994) 1093.
7. U. Dahmen, C. J. D. hetherington, M. A. O'Keefe, K. H. Westmacott, M. J. Mills, M. S. Daw and V. Vitek, Phil. Mag. Letters, 62 (1990) 327.
8. A. P. Sutton and R. W. Balluffi, Acta Metall., 35 (1987) 2177.
9. J. Wang and V. Vitek, Acta Metall., 34 (1986) 951.
10. A. P. Sutton and R. W. Balluffi, Interface in Crystalline Materials, Oxford University Press, 1995.
11. M. S. Daw, S. F. Foiles and M. I. Baskes, Mater. Sci. Reports, 9 (1993) 251.
12. P. Dang and M. Grujicic, Modeling and Simulation in Mater. Sci. and Eng., 4 (1996) 123.
13. D. Wolf, J. Appl. Phys., 68 (1990) 3221.
14. D. Wolf, J. Appl. Phys., 69 (1990) 185.
15. M. J. Mills, Mater. Sci. Eng., A166 (1993) 35.
16. J. M. Rickman, S. R. Fillet, D. Wolf, D. L. Woodraska and S. Yip, J. Mater. Res., 6 (1991) 2291.
17. G. H. Bishop, Jr, R. J. Harrison, T. Kwok and S. Yip, J. Appl. Phys., 53 (1982) 5609.

18. G. H. Bishop, Jr, R. J. Harrison, T. Kwok and S. Yip, J. Appl. Phys., 53 (1982) 5596.

19. C. Molteni, G. P. Francis, M. C. Payne and V. Heine, Mater. Sci. Eng., B37 (1996) 121.

20. D. J. Oh and R. A. Johnson, Atomistic Simulations of Material: Beyond Pair Potentials, Edited by V. Vitek and D. J. Srolovitz, Plenum Press, 223, 1989.

21. S. F. Foiles, private communication, 1996.

22. G. Palumbo, E. M. Lehockey and P. Lin, JOM, 50 (1998) 40.

23. C. P. Chen, D. J. Srolovitz and A. F. Volter, J. Mater. Res., 4 (1989) 62.

24. A. Otsuki and M. Mizuno, Proc. Symo. on Grain Boundary Structure and Related Phenomena, Thans. Japan Inst. Metals, Suppl. 27 (1986) 789.

25. M. F. Ashby, Surf. Sci., 31 (1972) 498.
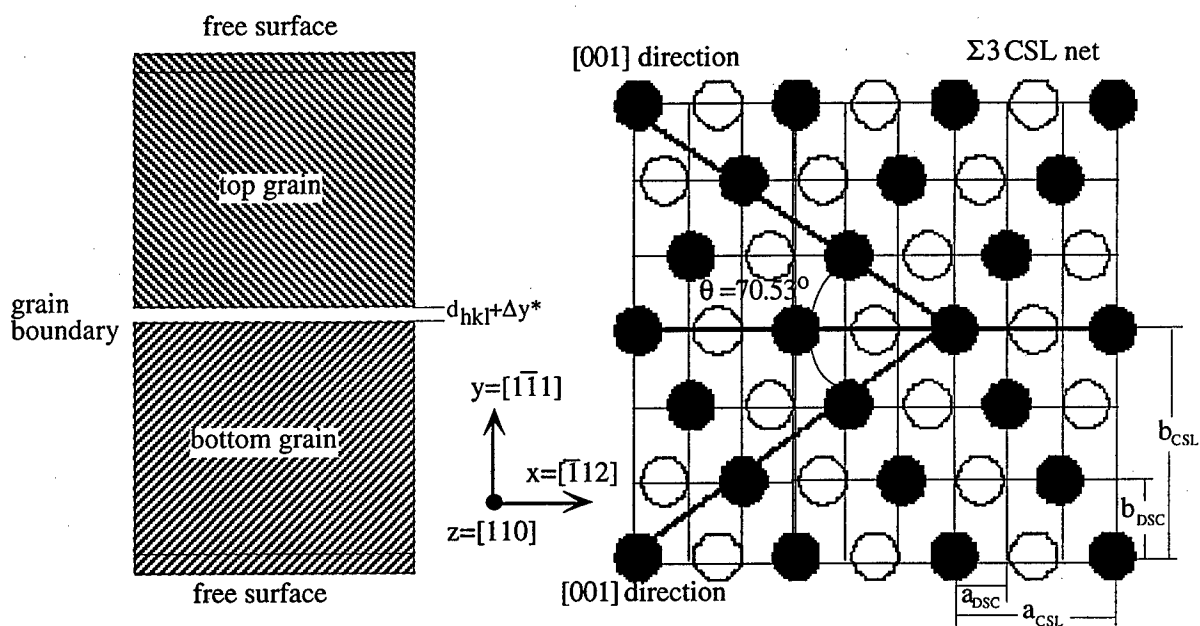
Figure 4.1: Schematic of the construction and notation of CSL/DSL tilt grain boundaries.
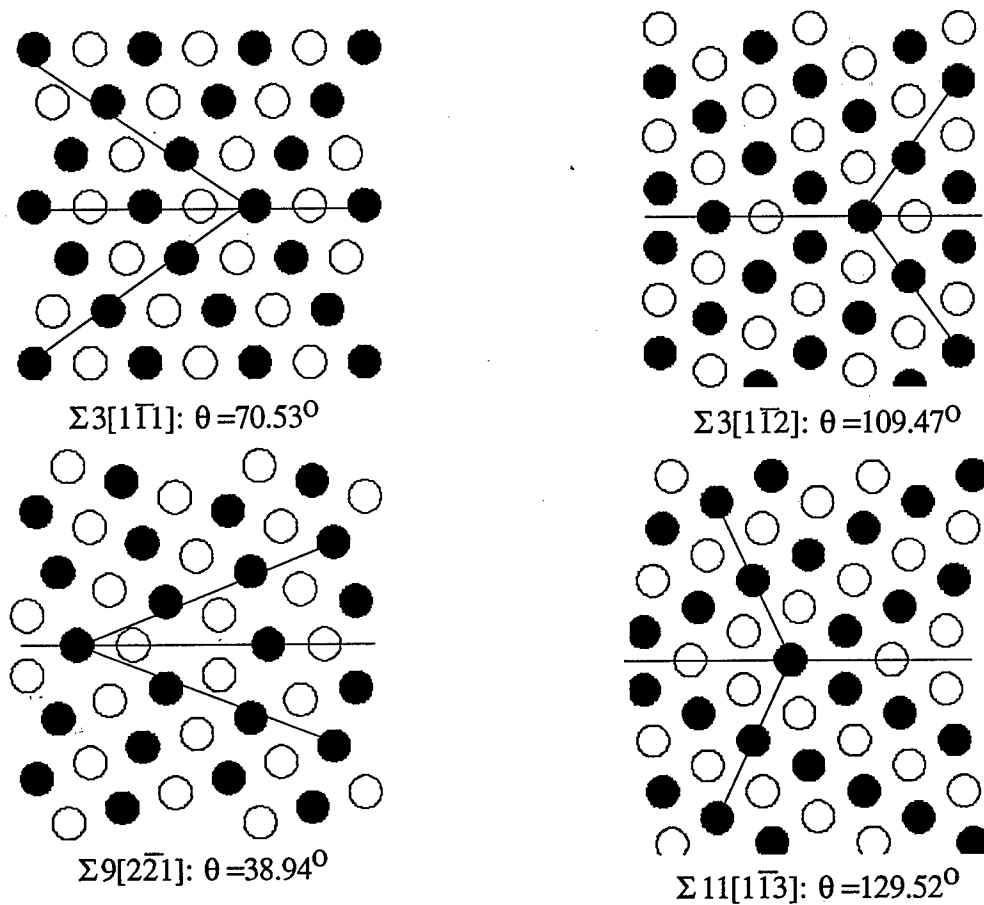
Figure 4.2: Equilibrium structures of selected tilt CSL grain boundaries about [110] axis of aluminum
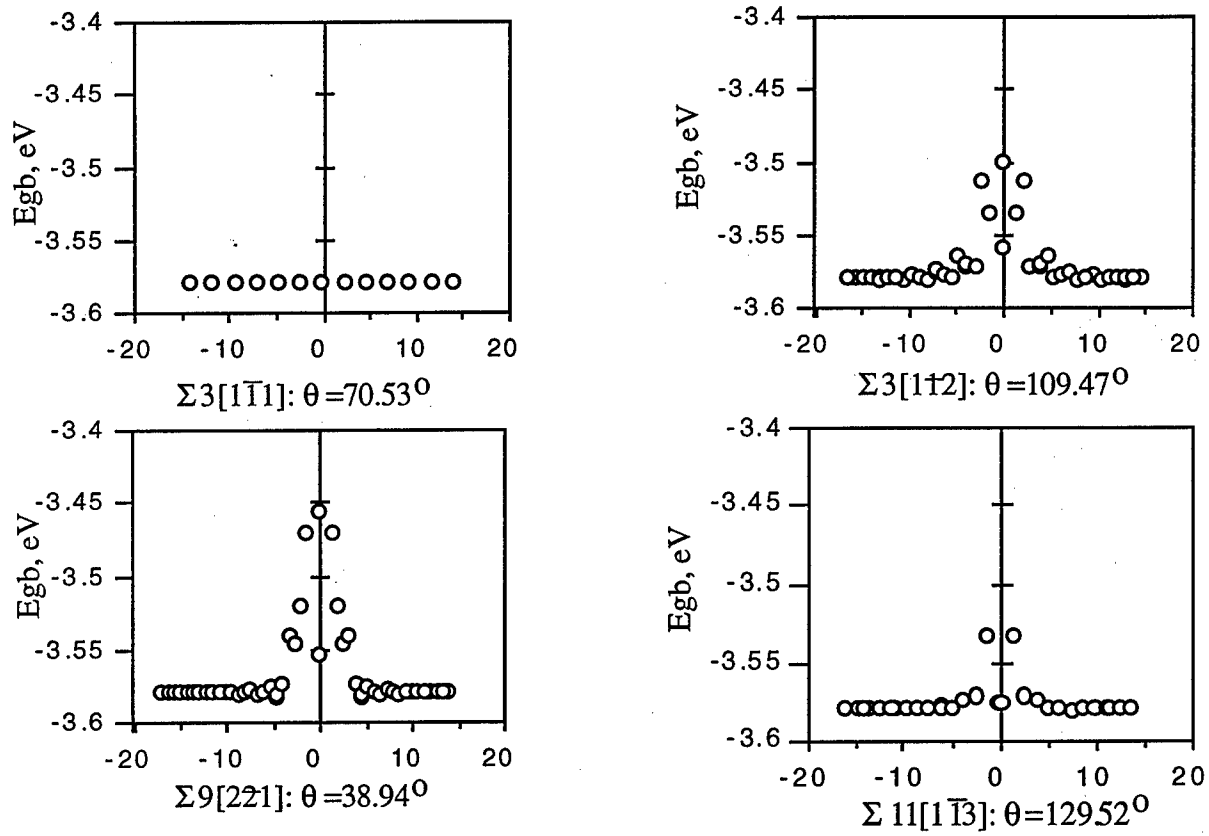
Figure 4.3: Energy distribution in equilibrium structures of tilt CSL grain boundaries.
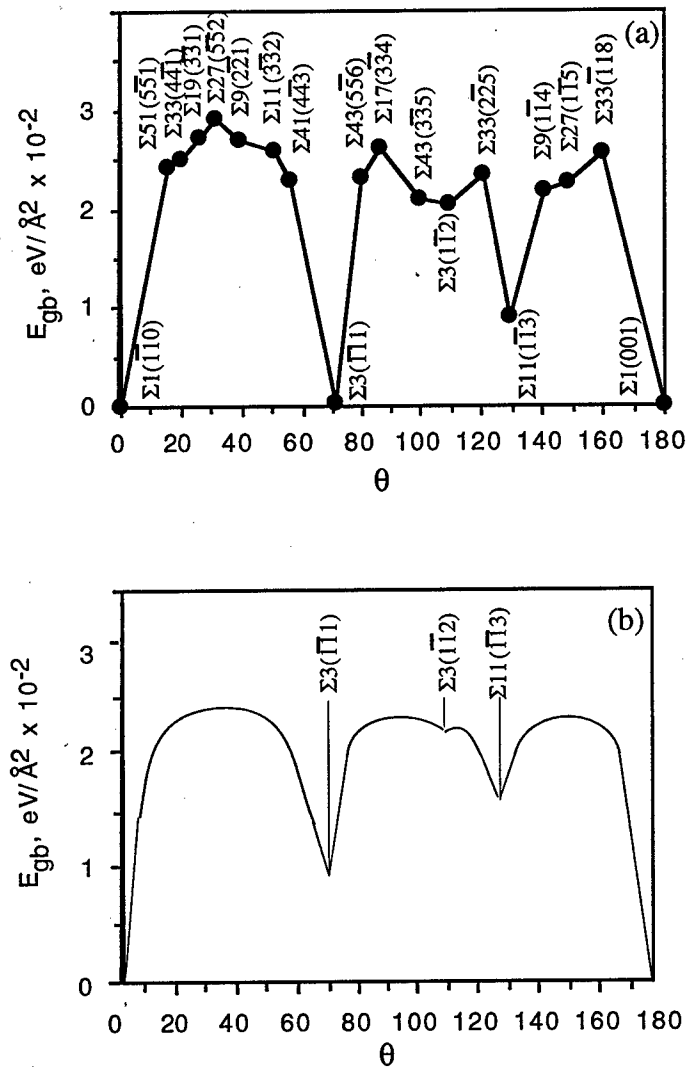
Figure 4.4: (a) Caculated grain boundary energy, E_{gb} of tilt CSL grain boundaries about [110] in aluminum as a function of misorientation angle, θ; (b) Corresponding experimental results [24].
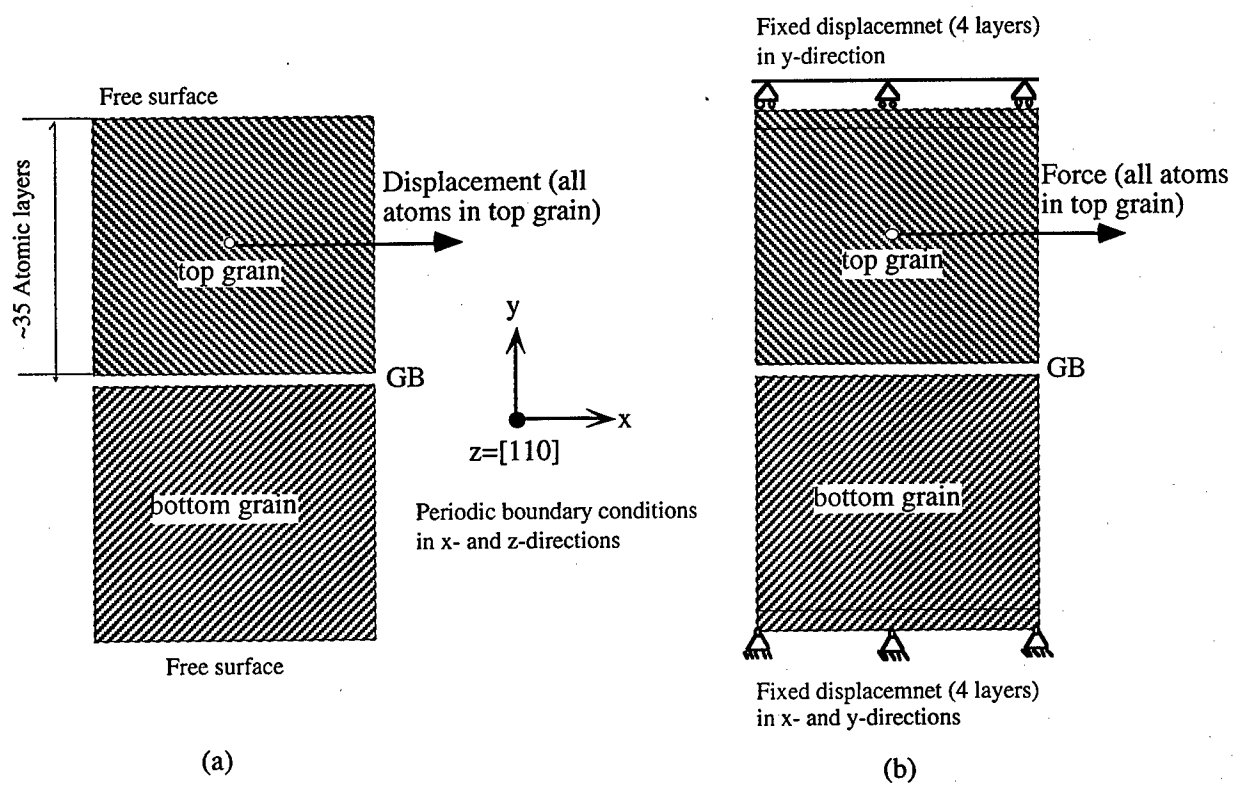
Figure 4.5: Boundary conditions of the computational crystals under (a) applied displacement and (b) applied force
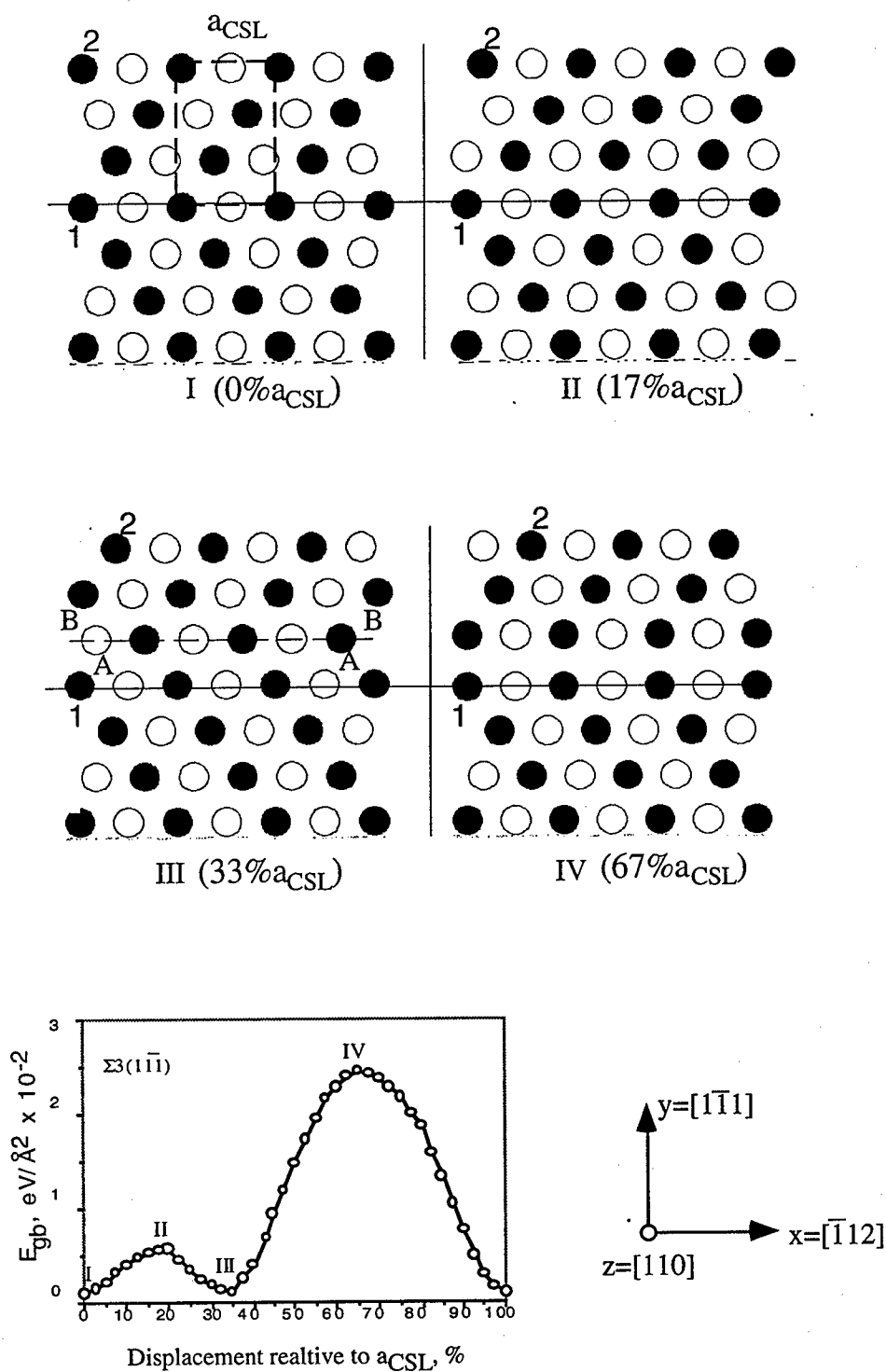
Figure 4.6: Energy evolutions during GBS process of $\Sigma 3[1\ \bar{1}\ 1]$ tilt CSL boundary
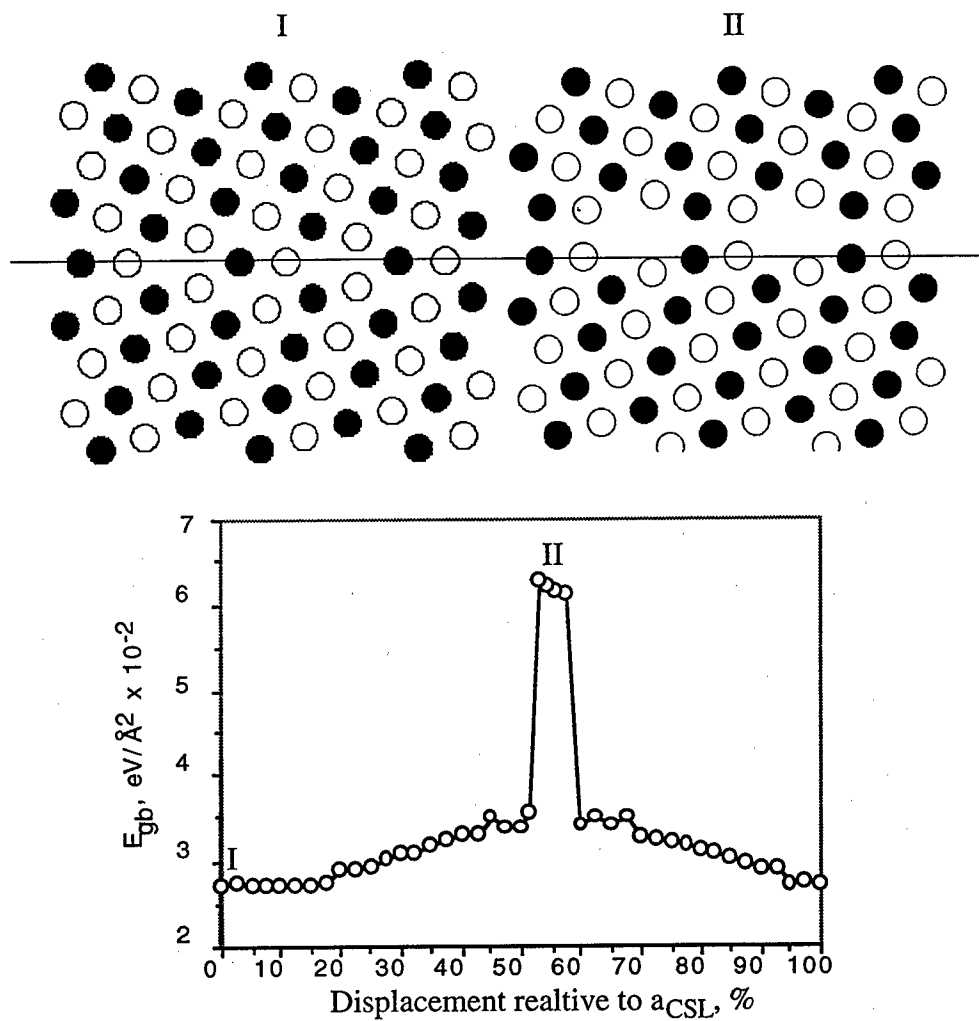
Figure 4.7: Energy evolutions during GBS process of $\Sigma 9[2\ \bar{2}\ 1]$ tilt CSL boundary.
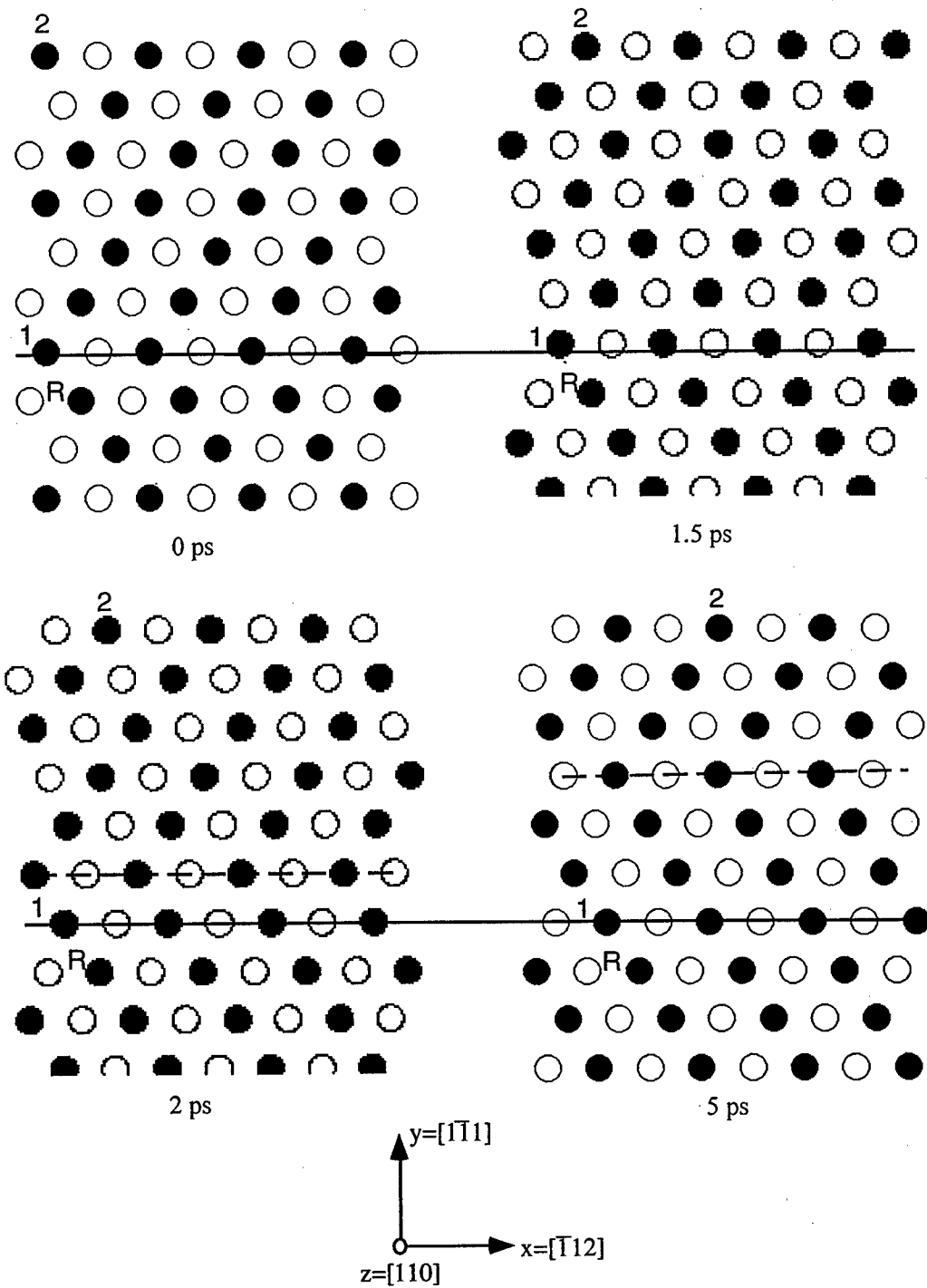
Figure 4.8: Evolution of $\Sigma 3[1\ \bar{1}\ 1]$ grain boundary structure under applied force
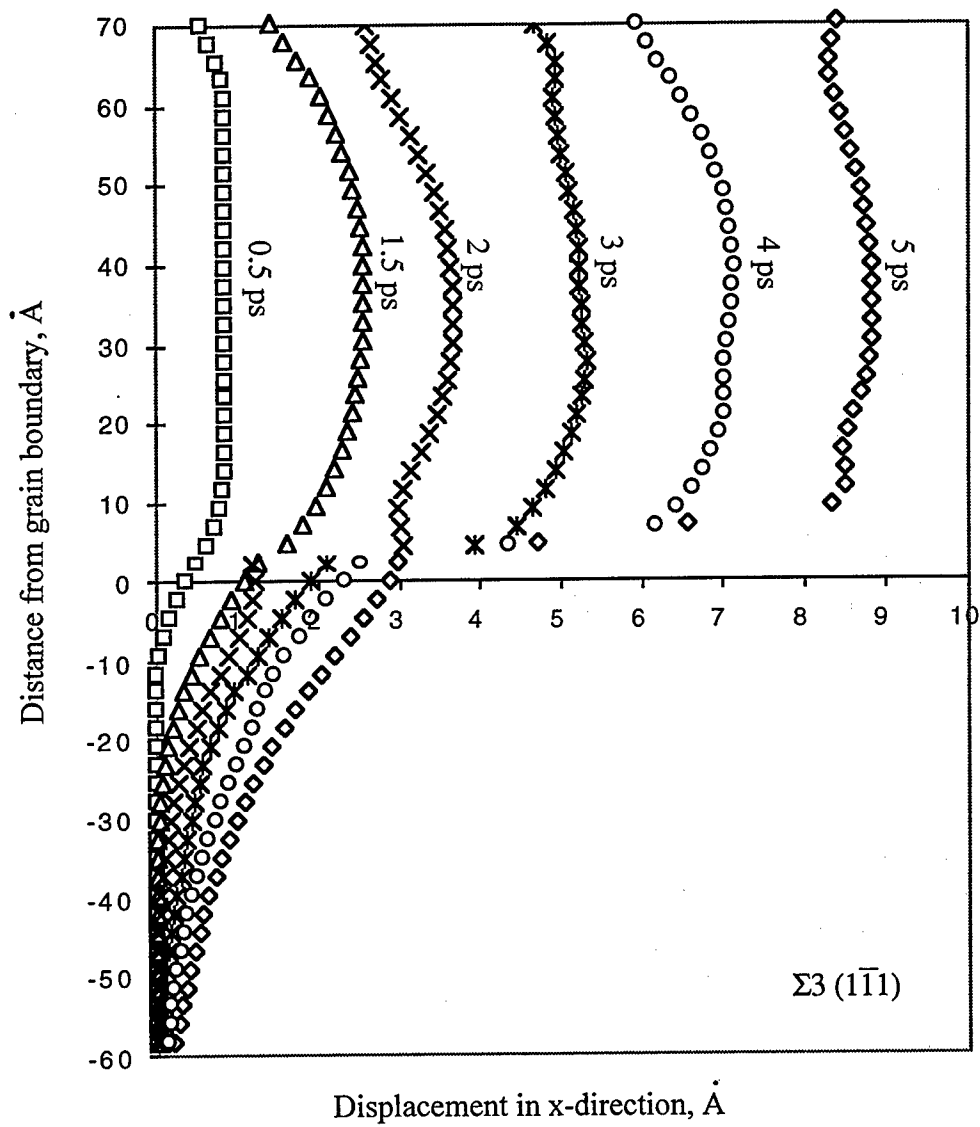
Figure 4.9: Relative displacement in x-direction as a function of time.
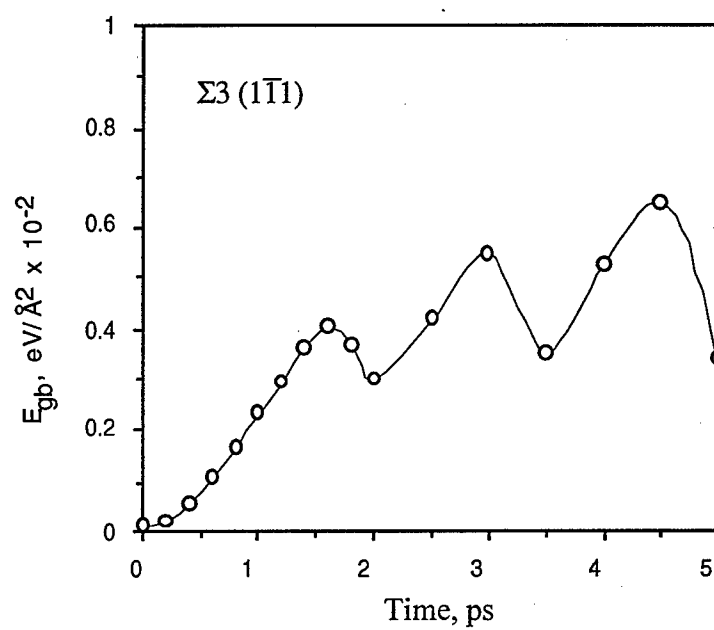
Figure 4.10: Grain boundary energy change during the simulation
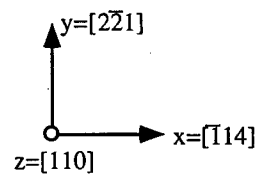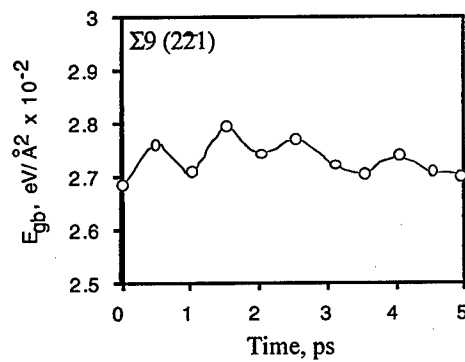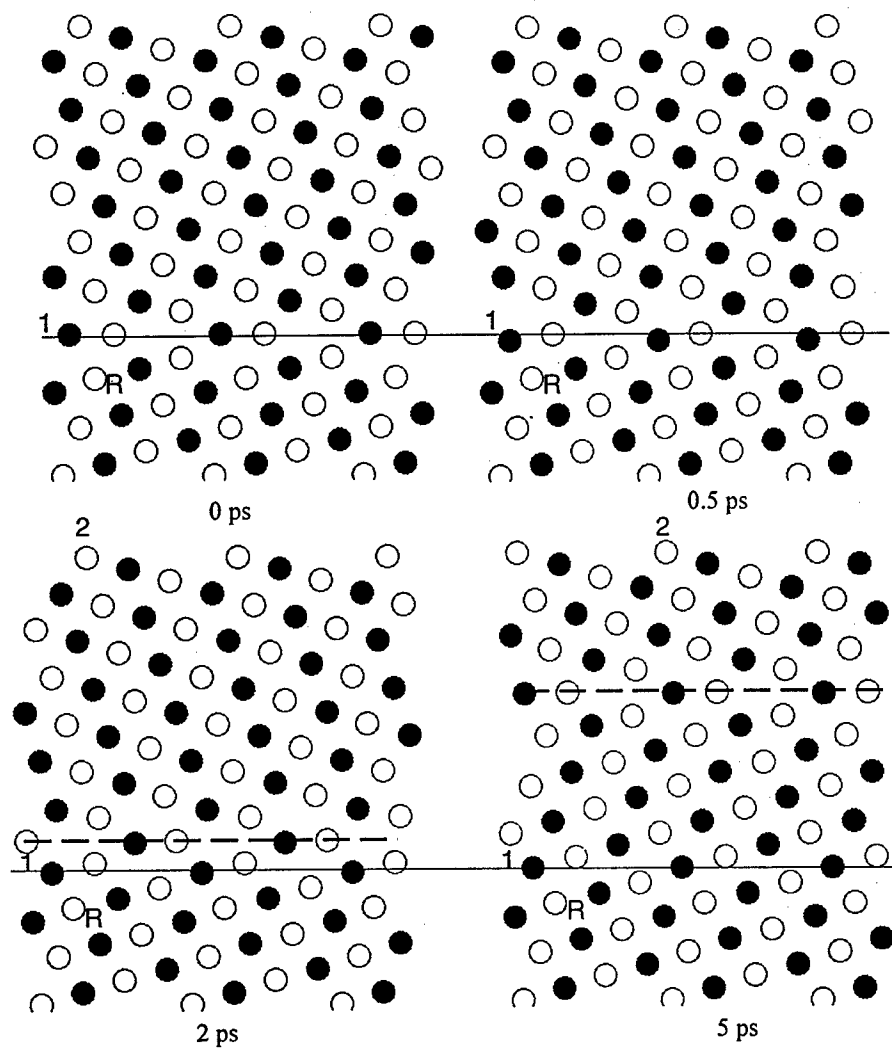
Figure 4.11: Evolution of $\Sigma 9[2\bar{2}1]$ grain boundary structure and energy under applied force
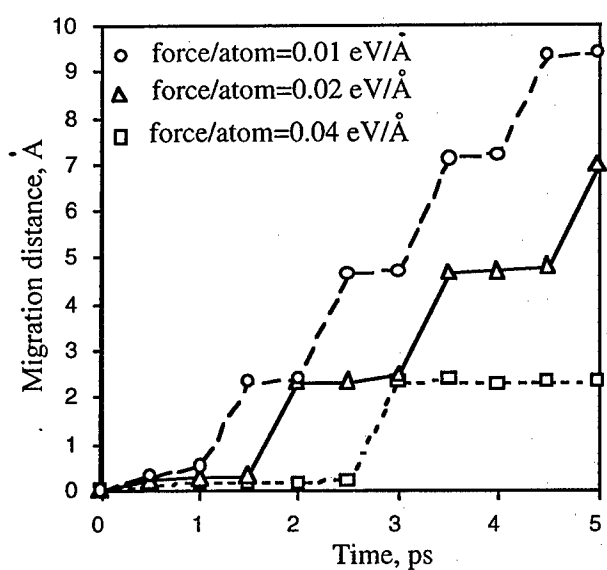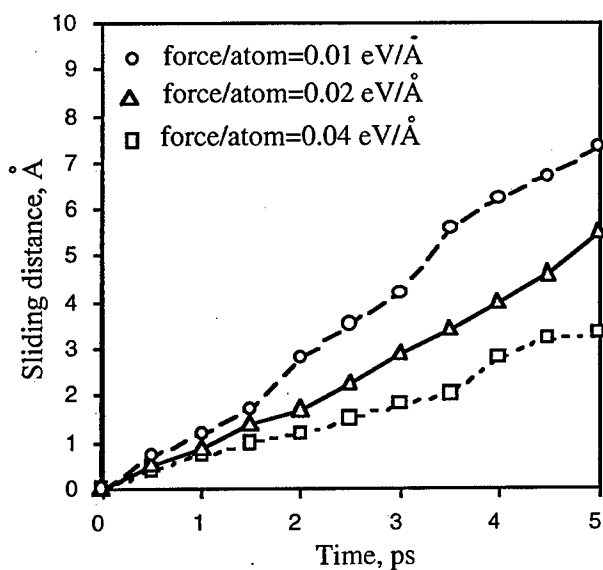
Figure 4.12: The displacement fields in $\Sigma 3$ $(1\ \bar{1}\ 1)$ grain boundary
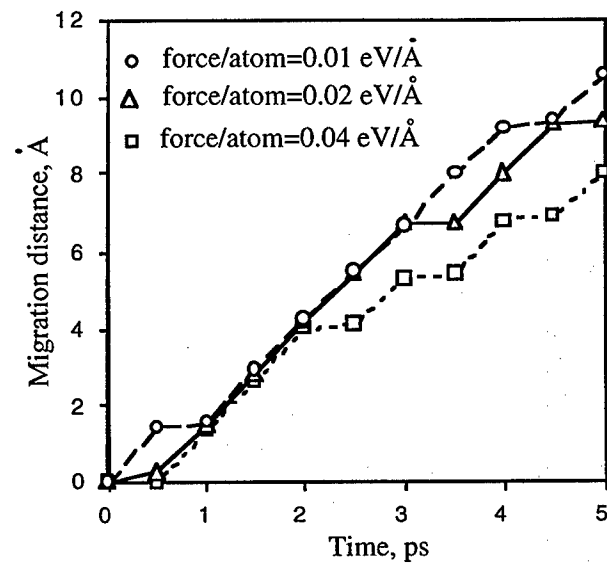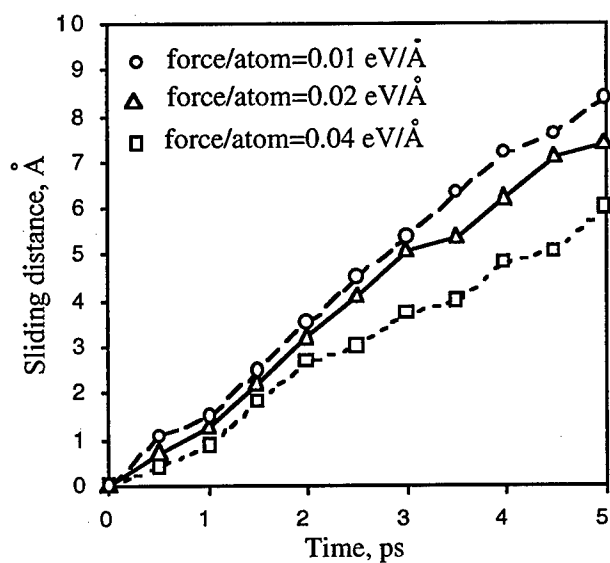
Figure 4.13: The displacement fields in $\Sigma 9(2\ \bar{2}\ 1)$ grain boundary
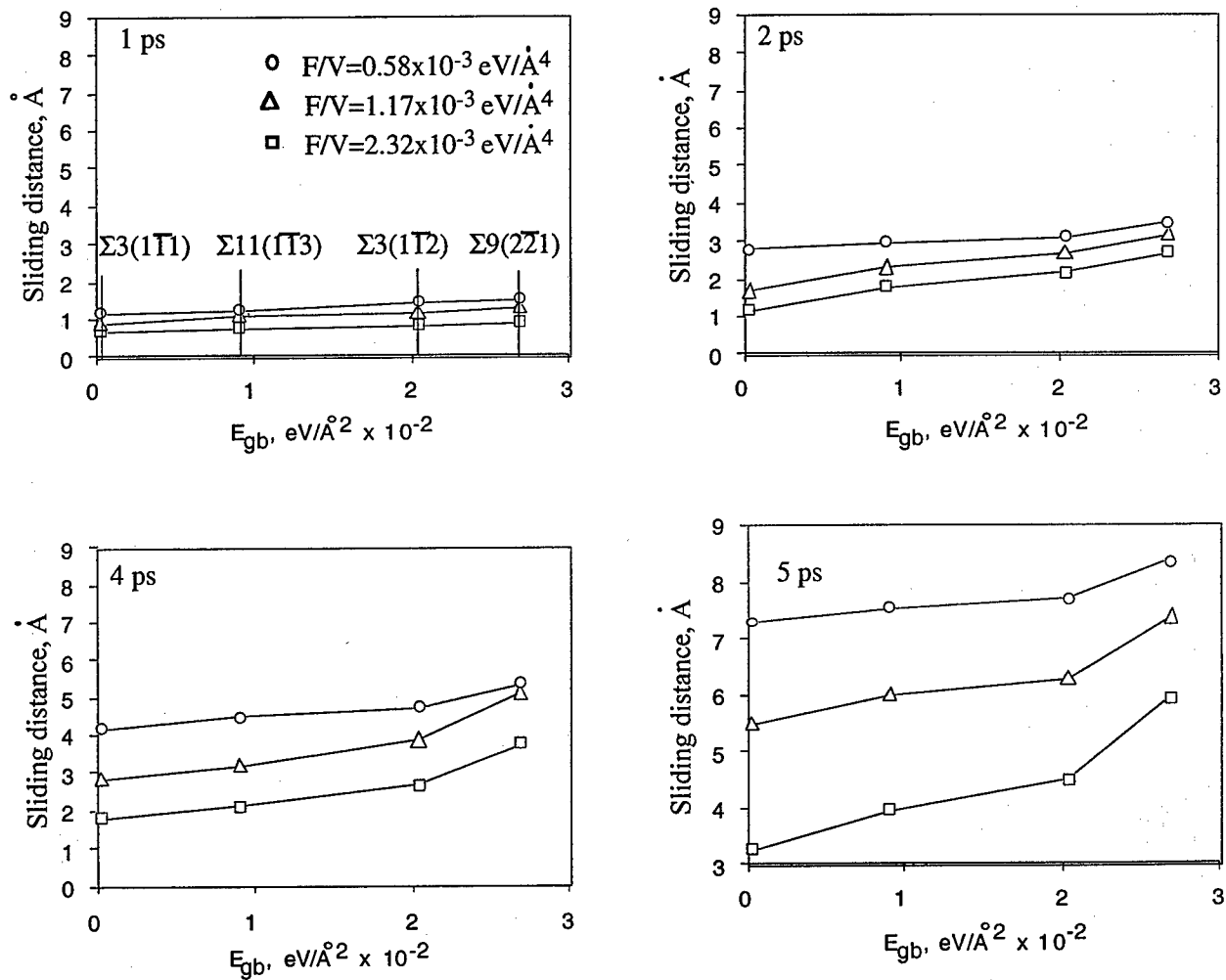
Figure 4.14: Grain Boundary energy effect on GBS (F/V is the total force per unit volume)
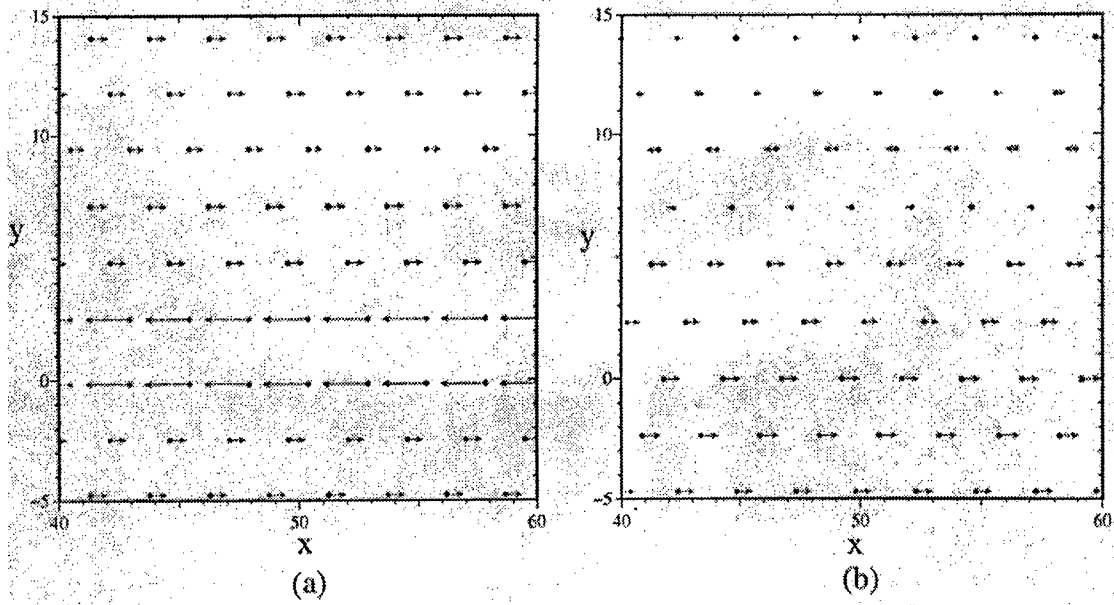
Figure 4.15: Local stress (s11) distribution in $\Sigma 3$ ($1\ \bar{1}\ 1$) boundary under (a) applied displacement (case IV in Figure 4.6) and (b) applied force (5 ps in Figure 4.8)
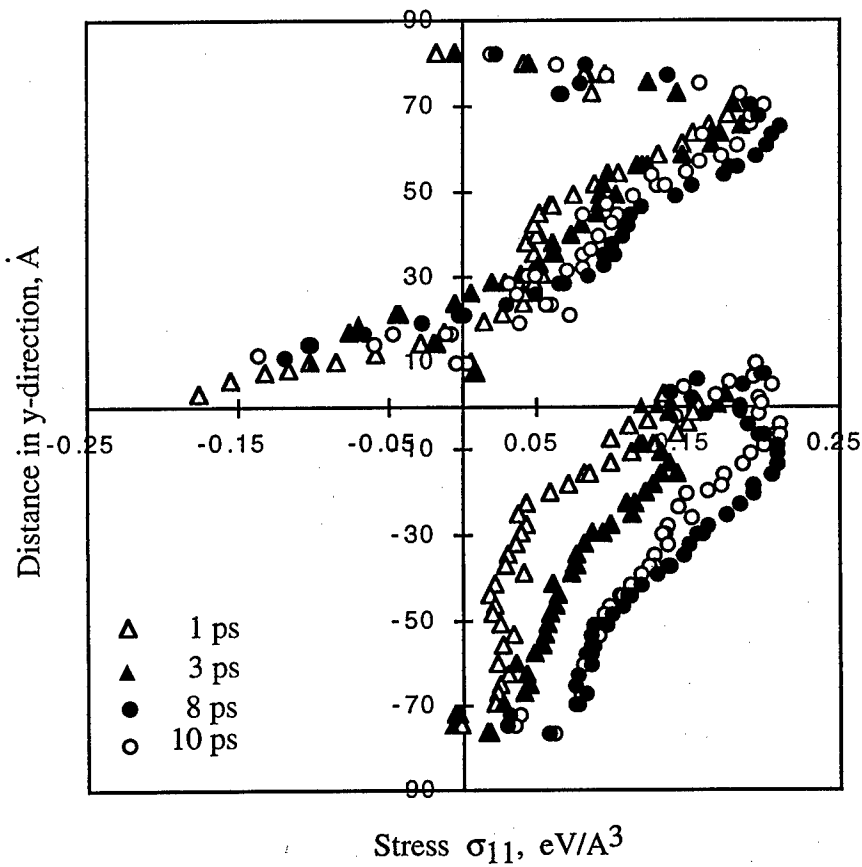
Figure 4.16: Stress (s11) fields in $\Sigma 3$ ($1\ \bar{1}\ 1$) grain boundary under applied stress (0.04 eV/A)

Chapter 5

Pre-existing Cavities in Superplastic Al 5083 and Al 7475 Alloys

5.1 Introduction

Presence or absence of pre-existing cavities during thermo-mechanical processing of superplastic sheet production is subjected to controversy. Some researchers have assumed that there should be pre-existing cavities because the manufacturing processes of superplastic materials involve extensive plastic deformation during thermo-mechanical processing [1], and a few have actually observed pre-existing cavities [2-4]. Others argued that pre-existing cavities are totally absent from superplastic metal sheets since they could not observe cavities in as-received materials [5-7], and also that very small cavities ($< 0.5\mu m$) may be sintered during the thermal exposure.

Cavitation behavior of a superplastic sheet metal depends on alloy chemistry, especially the second phase particles, and thermo-mechanical processing [8]. Intermetallic dispersoids are intentionally introduced into base aluminum alloys by adding Mn, Ti, and Zr. The purpose of introduction of such dispersoids (Al_2Mg_2Cr in Al 7475 and $AlMn_6$ in Al 5083) is mainly to prevent grain growth during superplastic forming process, thereby, retaining a fine grain size and equi-axis grain structure. Because dispersoids have both beneficial and deleterious effects, they must be chosen in such a way that they are effective in preventing grain growth while resisting nucleation of cavities.

In this paper we examine the origin of cavities during the thermo-mechanical processing of Al 5083 alloy, the alloy being a serious contender for automotive applications. Origin of preexisting cavities in the other popular Aluminum based superplastic alloy Al 7475 is also briefly addressed in this paper. We have examined in detailed as received materials using optical microscopy, to study the presence of cavities and the role of particles in determining the size of the cavities. We have numerically simulated the final cold rolling process to understand the origin of cavities and the effect of matrix, particle and particle-matrix

interfacial mechanical properties on the size of the cavities. We also developed an expression to relate the cavity size to the final thickness reduction based on a simplified analysis. The analysis and the experimental observations lead us to some conclusion regarding the size of observable cavities in relation to size of the particles and the strength of particle-matrix interfacial bonding.

5.2 Experimental results on Al 5083 and Al 7475

Al 5083-SPF is a relatively new solid solution strengthened alloy for superplastic forming application. The Al 5083 metal sheet used in this work was obtained from Sky Aluminum, Japan. In the base Al-Mg-Mn alloy, Cr, Zn, Ti and Zr are added for strengthening the alloy and producing second phase particles. During thermo-mechanical processing of Al 5083-SPF sheets, the ingot undergoes extensive plastic deformation at elevated temperatures with a final finish rolling at room temperature. The heat treatment cycle is designed to obtain fine and equi-axed grain structure, a prerequisite for superplastic deformation. The details of the therm-mechanical processing can be found elsewhere[10]. In the present context, we focus our attention on the final cold-roll from 10 mm to 2 mm with a thickness reduction of 10-15% per pass and its effect on the formation of cavities. Like Al 5083, Al 7475 is also a statically recrystallized alloy with a similar thermo-mechanical processing (including the final cold roll) aimed to achieve fine equi-axed grain structure for superplastic applications[11]. In both the alloys, grain growth during subsequent high temperature superplastic forming is retarded by the introduction of sub-micron dispersoids.

In this work, samples were prepared for optical examination, from the as-received material in three different orientations as shown in Figure 5.1. Observations were made on facial, transverse and longitudinal sections on both the material systems. The samples were polished upto 0.05 μm solution but with no subsequent any chemical etching to avoid black chemical marks which may interfere with the observation of cavities. In Al 5083 superplastic alloy, second phase particles are uniformly distributed throughout specimens, with a size of 0.1 to 2 μm under optical microscope. It should be noted that the lower limit of optical examination (with a magnification of 500) is about 0.1 to 0.5 μm, i.e., any particle (or cavity) smaller than this value even if present cannot be observed. A few large particles of size as much 5 to 10 μm were observed in some locations.

Figure 5.2(a) shows a large pre-existing cavity in Al 5083, where rolling direction is horizontal and thickness direction is vertical. It can be seen that cavities are present both ahead and behind the particles with respect to the rolling direction. This observation of cavities on either side of particles (along rolling direction) is very typical. Also, the size of the cavities depended on the size of the particles, larger cavities accompanying larger particles. Some large particles were broken into pieces and cavities usually surrounded (along rolling direction only) the broken pieces. The tapered section of the cavity can be attributed to the healing of the cavities during subsequent thermo-mechanical rolling where the matrix (aluminum) freely flows into the cavities. After heating the specimen to 555°C

for 40 minutes, the size and the number of pre-existing cavities in the specimen were seen to be reduced due to sintering. Figure 5.2(b) shows cavities in Al 5083 specimen after the heat treatment using scanning electron microscopy (SEM). SEM was used to obtain high magnification much more than the optical limits. The conclusion here is that though the size of the cavities are reduced significantly due to the heat treatment process, pre-existing cavities are not completely eliminated. Figure 5.2(c) shows the presence of pre-existing cavity in Al 7475, with very similar features as that of Al 5083.

An important question is the role of preexisting cavities in the cavity growth and eventual fracture during superplastic deformation. Caceres and Silvetti [???] while studying the cavitation damage of Zn-22% Al superplastic alloy concluded that cavities grew from the pre-existing microvoids. However, Chokshi and Langdon argued against preexisting cavities contributing to damage since they did not observe them in the as-received material, and also that the microvoids may be sintered during the thermo-mechanical conditions of superplastic deformation. In addition they observed that cavities were aligned along the rolling direction rather than being uniformly distributed in consonance with particle distribution. We tend to agree with Caceres and Silvetti for the following reasons. When the Al 5083 was superplastically deformed, the density measurements indicated that in the grip region (subjected to thermal excursion and compressive stress), was almost the same as that of as-received material (ratio being 0.9994). This contrast to the superplastically deformed regions where the density varied by about 5%. Cavitation damage is the primary mechanism of final fracture in these materials; in most of the cases, the cavitation is in the vicinity of particles. Though we cannot unequivocally state that preexisting cavities cause the final fracture, we know that both preexisting cavities and the fracture inducing cavities are associated with particles. This can be attributed to the vastly differing flow properties of the particles and matrix material (eg. Aluminum). The fact that cavities preexist at least in some materials system is indisputable. The question then is whether these cavities heal (or disappear) completely before superplastic deformation starts cannot be clearly answered. Since we observe cavities in the preexisting stage as well as final fracture stage around the same region (mostly in the rolling direction) leads us in the direction that the preexisting cavities do play a role in the growth. Duality of reporting the absence or presence of cavities (or micro voids) then may be related to the inability or ability to observe them under a given set of conditions; when in fact the microvoids always exist. This statement will be further clarified when we look at the results of the numerical simulations.

5.3 FEM Simulation of the rolling process

Since it was suspected that cavities may originate during the final cold-rolling process during the SPF sheet manufacture, a numerical simulation of this stage was conducted using a nonlinear finite element model (FEM. **include reference and figure of thermo-mechanical process.** According to sheet metal manufacturing process, the last step of thermo-mechanical process is cold-rolling with a reduction in thickness of 10-15% [10-11]. Since the final cold rolling process in the manufacture of superplastic sheet is the most vul-

nerable step this rolling step was analyzed in the FEM. It was assumed that the material was completely cavitation free prior to this step. A 15% reduction in thickness was applied during the FEM analysis. Mechanical properties of Aluminum at room temperature were used as the matrix material, whereas the particle was assumed to be a rigid elastic with the Young's modulus about ten times that of aluminum. Both the matrix and the particle were assumed to be isotropic. As shown later, the mechanical/fracture properties of the particle-matrix interface plays a critical role in the debonding and the initiation of cavities. Though interfaces can be modeled using shear based (debond strength), or energy based (fracture toughness) criteria, interfacial stiffness E_i is used in this work to describe its behavior. This concept can be easily implemented in the code as a spring element separating the particle and the matrix. A high value of E_i (equal to that of matrix, E_m) signifies a strong bond, whereas a low value $E_i = 0.05 \ E_m$ denotes a weak bond. The effect of variation of E_i on the results are also analyzed.

The rolling process was simulated for a single pass with a reduction in thickness as a given parameter. Rolling friction between the work (sheet metal) and the die (roller) was assumed. Feeding was forced initially at one end at a give rate after which the sheet is automatically fed due to frictional condition between the work and the die. The model was implemented using MARC/MENTAT FEM package. Young's modulus of Al matrix was assumed to be 10 GPa with a initial yield value of 140 MPa and work-hardening afterwards. Four node plane strain element was used. There are 2434 nodes and 2324 elements in the model, as shown in Figure 5.3(a) where 46 elements are used as a particle. Further, MARC contact algorithm was implemented to prevent two materials (the Al matrix and the particle) from penetrating each other and more dense meshing was used along particle/matrix interface, see Figure 5.3(b). A total of 65 increments were necessary to achieve the thickness reduction process.

In the initial simulation a very low bond strength was used and the results are shown in Figure 5.4. During the early stages of deformation (increment 20), cavities are seen to form as shown in Figure 5.4(a). With further deformation of the sheet, cavities change both in size and in shape. However, the cavities are always associated with the particle at the both ends along the rolling direction. This is not surprising considering the fact that tensile stresses at the particle-matrix interface occurs only along that direction. At increment 25, pre-existing cavities grow and can now be clearly seen in Figure 5.4(b). Further deformation continues to grow the cavities. When the rolling is finally completed (increment 50), the cavities are fully developed, Figure 5.4(e) indicating the origin of processing induced preexisting cavities.

5.4 Effect of particle-matrix interface and particle size on cavities

The size of the particles plays a critical role in determining the cavity initiation and further growth and coalescence. Though shapes may also play some role, they have not been analyzed in this paper. In modeling a sheet metal of 2-10 mm thick with size of the particles ranging

from sub-microns to a few microns, it is important to understand the effect of scales. There are three orders of magnitude difference between the thickness of the sheet and that of the particle. However, for most of the rolling process in the thickness direction a homogeneous state of deformation was observed in the thickness direction for a single material system. Also the strain and stress fields were affected only a few length scales from the particle location as shown later. Thus when the size effect was studied the particle to sheet thickness was so chosen that edge effects do not play a role. Same original sheet thickness was selected with particles of different sizes by varying the number of elements from 1, 2 to 6. Under identical rolling conditions the results of the simulations were examined. In this case, the interface bonding was constant for $E_i = 0.05E_{Al}$.

It is observed that even for one element particle cavitation occurs. Figure 5.5 shows the effect of thickness reduction and particle size on cavity fraction in terms of the area fraction of particle. At low spring constant (0.05% Young's modulus of matrix), area fraction of pre-existing cavity linearly increases as increasing thickness reduction. When particle size decreases, area fraction of pre-existing cavity also decreases slightly.

Increasing interface Young's modulus E_i to 50% Young's modulus of matrix prevents the occurrence of pre-existing cavities. Figure 5.6 shows that there is no cavity if using a spring constant of Young's modulus of matrix. The higher spring constant, the better interface bonding between particles and matrix. Therefore, it is understandable that a better interface bonding will prevent cavities to occur during thermo-mechanical process. Figure 5.7 shows detailed numerical results of the effect of spring constant on area fraction of pre-existing cavity for a 6-element particle. With a spring constant of 50% Young's modulus of matrix, area fraction is only 0.3%, which is virtually zero. Decreasing spring constant will increase cavity area fraction.

5.5   Discussion

Although presence or absence of pre-existing cavities has been a controversial topic for decades, several models were established on the assumption of the presence of the pre-exist cavities generated during the thermo-mechanical process, but very few experimental evidence are available [9], owing to the small size of pre-existing cavities and low resolution of optical microscope.

In our experimental observation on Al 5083 and Al 7475, we have obtained a direct evidence to support that there are pre-existing cavities arising from the thermo-mechanical processing cycles during manufacture of Al 5083 and Al 7475 sheet metals. The pre-existing cavities are found to be always associated with second phase particles. Intuitively we can conclude that the origin and distribution of preexisting cavities depend on the size, shape, distribution of particles, chemical and mechanical properties of matrix and second phase particles, and more importantly interfacial bonding between matrix and particles. For large size of second phase particles, pre-existing cavities are not avoidable. To eliminate pre-

existing cavitation, submicron particle size is prerequisite.

During the cold rolling process, these particles break up and align into particle stringers parallel to the rolling direction. This particle stringers are most obvious on longitudinal section. It is possible the previous reported researches might have paid attention only to the face section, and not to the longitudinal or transverse sections. The plasticity of the matrix is not so high that the discrepancy or void produced at the interface was rehealed. The broken brittle particles will also induce pre-existing cavities between the parts. These cavities with the radii up to 5 μm were only observed around very large particles, and these large cavities were significantly sintered during the process of static recrystallization prior to superplastic deformation.

FEM simulation of cold rolling, the last step during the thermo-mechanical process, shows the possibility of occurrence of pre-existing cavities. Pre-existing cavities are always started on the matrix/particle interface. Since there is virtually no bonding between matrix and particle if the spring constant is 0.05% Young's modulus of matrix, cavity occurs in where there is a tensile stress state rather than in a zone of compressive stress. In other words, cavities are associated with particle in both ends along rolling direction where tensile stress predominate.

On the other hand, pre-existing cavities initiate immediately whenever there is a permanent plastic strain. As the strain increases, cavities develop and cavity size increases. At the final increment, the relationship between them is linear, see Figure 5.5. The area fraction of pre-existing cavities increases as thickness reduction or plastic deformation increases. A simple model for one element particle can explain this, see Figure 5.8. In the FEM model meshing, rectangular elements with height (h_0) and width (w_0) are used. Particle occupies one element. After rolling deformation, the meshes are deformed and distorted. We here neglect small elastic deformation of particle. It is further assumed that the elements directly above and below particle keep rectangular. From the definition of thickness reduction (δ),

$$\delta = \frac{h_0 - h}{h_o} \times 100\%.$$

Since the area of each element keeps constant during plastic deformation, we have $wh = w_0 h_0$. Therefore,

$$w = \frac{w_0 h_0}{h} = \frac{w_0}{\frac{h}{h_0}} = \frac{w_0}{1 - \delta} = \left(1 + \delta + \delta^2 + \delta^3 + ...\right) w_0$$

or the area fraction of pre-existing cavity as defined above,

$$\text{Cavity Area Fraction} = \left(\frac{w h_0 - w_0 h_0}{w_0 h_0}\right) = \left(\delta + \delta^2 + \delta^3 + ...\right)$$

If we neglect higher order components, we get the area fraction of pre-existing cavity is approximately equal to the thickness reduction. The numerical results are consistent with this simple model for 6-element particle. However, the area fraction is below the value from the model for 1- or 2-element particle, see Figure 5.5.

Particle size plays in an important role in pre-existing cavitation. With smaller particles, it is difficult to find pre-existing cavities. From our simple model, the area fraction of pre-existing cavities is the same order as thickness reduction. If particle size is submicron, pre-existing cavities have only tenth of particle size. Only under SEM can we observe cavities. If there are particles with size larger than $5\mu m$, it is very much likely pre-existing cavities to be easily observed with optical microscopy.

If there is strong enough bonding between particles and matrix, we expect no pre-existing cavities. As shown in Figure 5.6, using E_i of 50% Young's modulus of matrix will avoid cavities. When the bonding deteriorates, pre-existing cavitation will prevail.

5.6 Summary and Conclusions

Although the subject of pre-existing cavitation is controversial, it does exist in the two important Aluminum based superplastic materials we have examined. The evidence is provided by the direct observation of as-received Al 5083 and Al 7475 sheet metal samples. The occurrence of pre-existing cavities is associated with second phase particles, especially those of a larger size. Numerical simulation verifies that there is a possibility of introduction of pre-existing cavities during single pass rolling process and that the occurrence depends on thickness reduction, particle size and bonding between particle and matrix.

References

1. M. J. Stowell, *Superplastic Forming of Structural Alloy*, The Metallurgical Society of AIME, ed. by N. E. Paton and C. H. Hamilton, pp 321-336, 1982.
2. C. H. Caceres and D. S. Wilkiinson, *Acta Metall.*, 35, p. 897-906, 1987.
3. S. H. Goods and L. M. Brown, *Acta Metallurgia*, 37, p. 35, 1984.
4. K. Kannan, C. H. Johnson and C. H. Hamilton, *Materials Science Forum*, 243-245, p. 125-130, 1997.
5. A. H. Chokshi and A. K. Mukherjee, *Materials Science and Engineering*, A110, p. 49-60, 1989.
6. A. H. Chokshi and T. G. Langdon, *Acta Metallurgica*, 37, p. 715-723, 1989.
7. X. Jiang, J. Cui and L. Ma, *Superplasticity in Metals, Ceramics, and Intermetallics*, Vol. 196, MRS, ed. by M. J. Mayo, M. Kobayashi and J. Wadsworth, pp. 51-56, 1990.
8. C. C. Bampton and R. Raj, *Acta Metallurgica*, 30, p. 2043 - 2053, 1982.
9. C. C. Bampton and J. W. Edington, *Metallurgical Transactions A*, 13A, p. 1721 - 1727, 1982.
10. H. Iwasaki, K. Higashi, S. Tanimura, T. Komatubara and S. Hayami, *Superplasticity in Advanced Materials*, ed. by S. Hori, M. Tokizane and N. Furushiro, The Japan Society for Research on Superplasticity, pp. 447-452, 1991.
11. J. Pilling and RN. Ridley, *Superplasticity in Crystalline Solids*, The Institute of Metals,

p. 20, 1989.
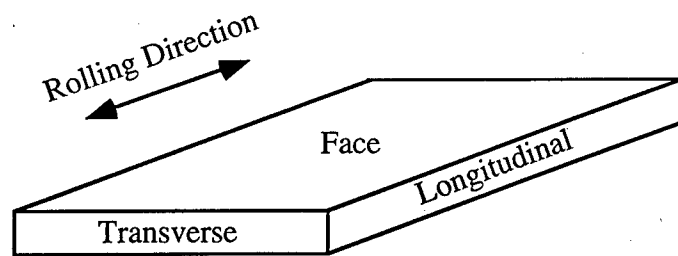
Figure 5.1: Sampling section terminology.
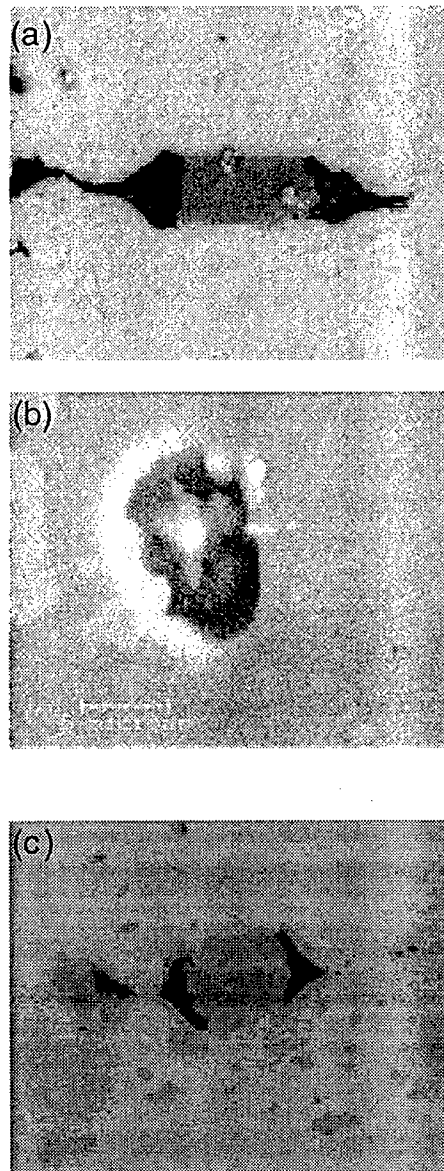
Figure 5.2: Pre-existing cavity in as-received (a) Al 5083, (c) Al 7475, longitudinal section and (b) SEM Al 5083 after annealing, showing cavities associated with both sides of particle along rolling direction.
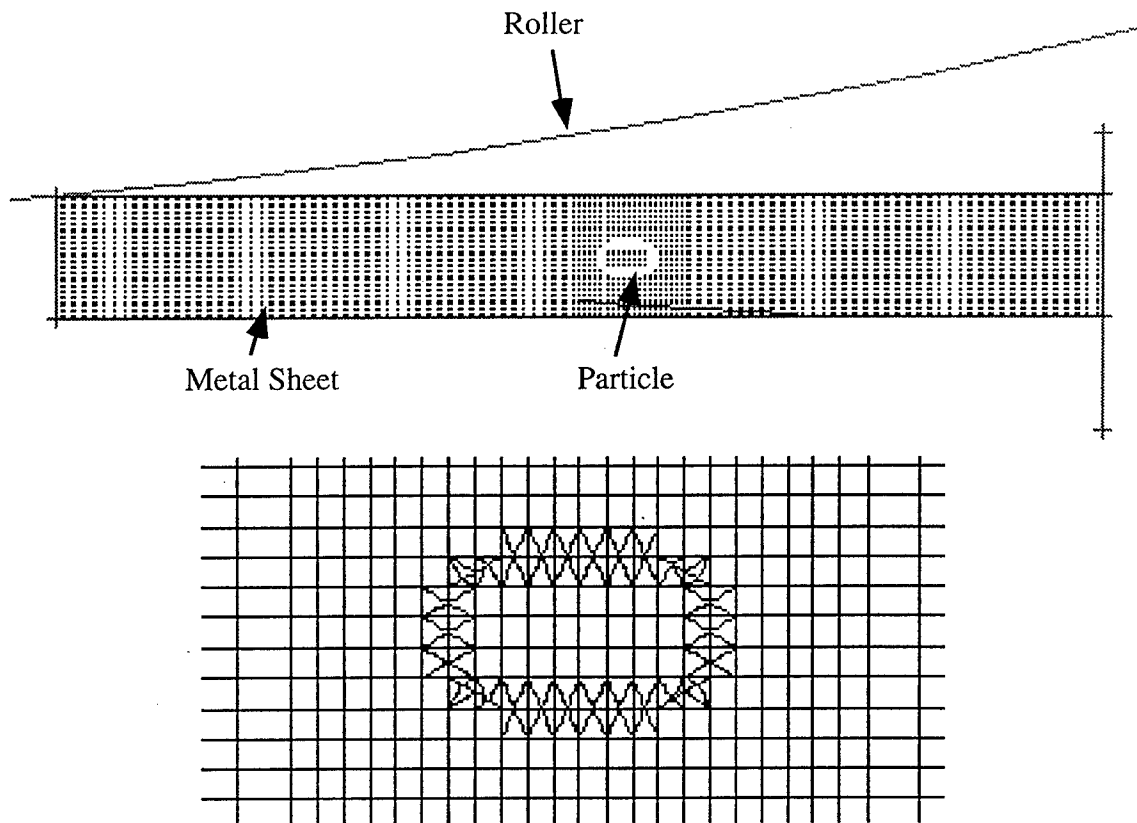
Figure 5.3: FEM model for simulating for a single pass rolling (a) during cold rolling and (b) local FEM meshing surrounding particle.
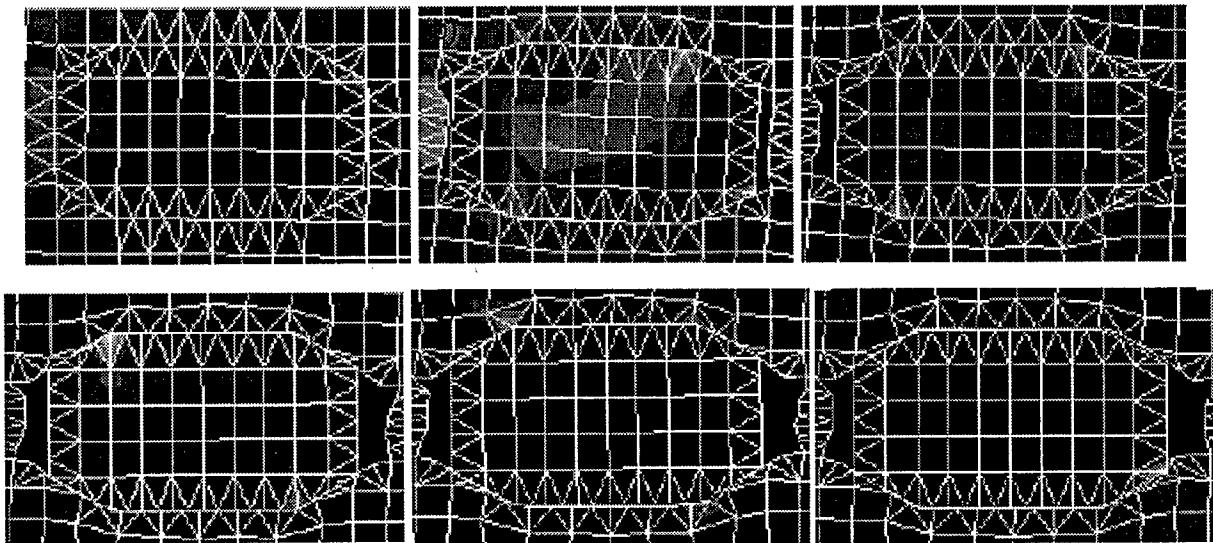
Figure 5.4: Post-FEM processing showing pre-existing cavities formed during a single pass rolling process, 46-element particle. (a) Increment 20, (b) Increment 25, (c) Increment 30, (d) Increment 35, (e) Increment 50 and (f) Increment 65.
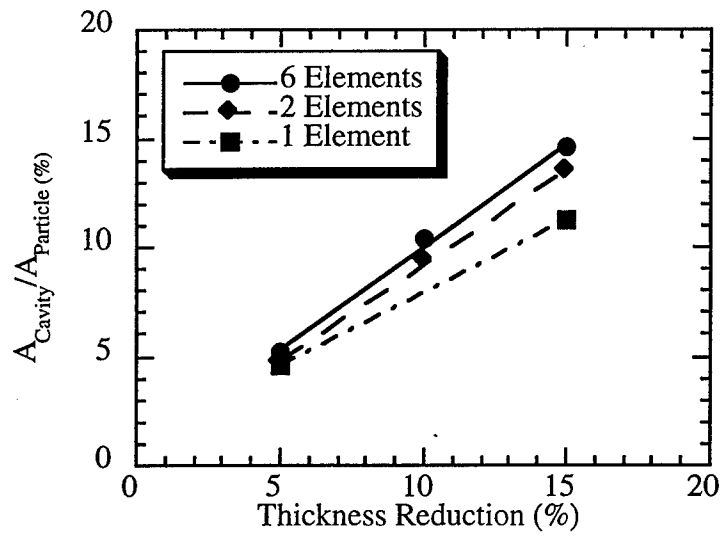
Figure 5.5: The effect of thickness reduction and particle size on pre-existing cavity, with E_i of 0.05% E_{Al}.
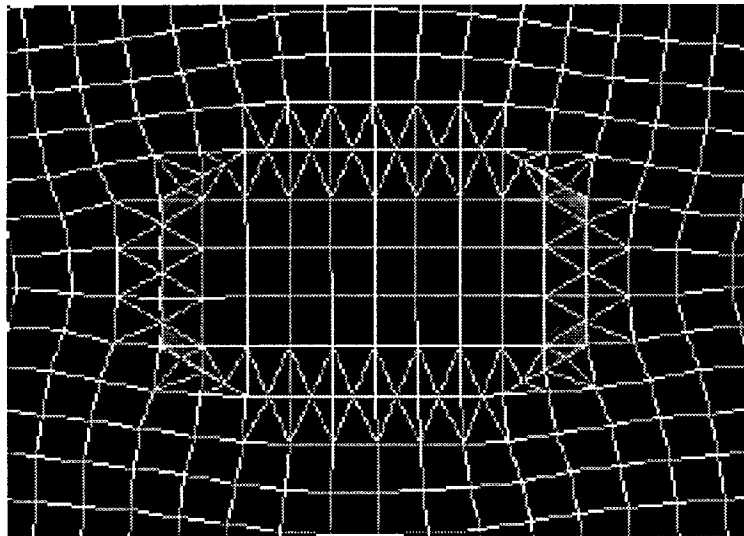
Figure 5.6: Higher E_i (50% E_{Al}) prevents pre-existing cavity.
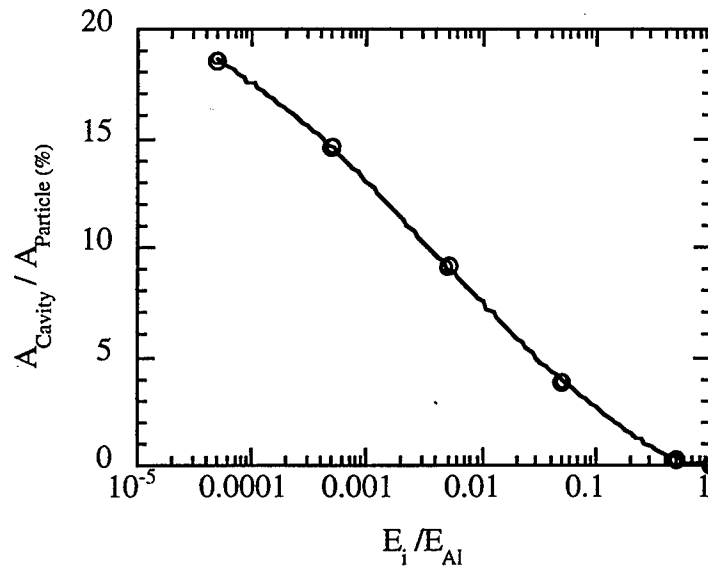
Figure 5.7: Variation of area fraction of pre-existing cavity with E_i for 6-element particle.
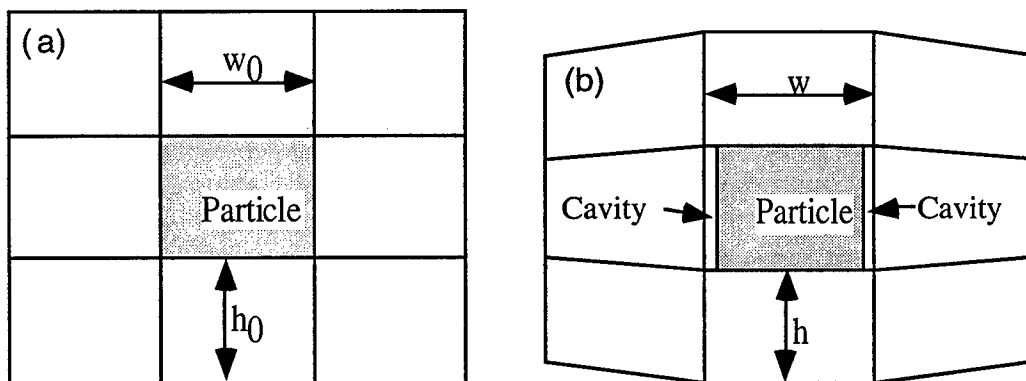
Figure 5.8: Schematic relationship between cavity area fraction and thickness reduction, (a) before and (b) after rolling deformation.

Chapter 6

The Cavitation Behavior of Superplastic Al 5083 Alloy under Multiple Stress States

6.1 INTRODUCTION

It is well established that cavitation may occur in most quasi-single and micro-duplex superplastic alloys during tensile superplastic flow. This may limit the applications of superplastically formed parts in industries due to the deleterious effect of cavities on service properties (e.g. tensile, creep, fatigue and stress-corrosion performances). As a consequence, the cavitation behavior has received increasing study in the recent years [1].

Cavitation is most likely to develop at grain boundary particles in quasi-single phase alloys according to the previous experimental observations. Cavities may pre-exist from the thermo-mechanical process applied to produce the fine grain size. Stowell [2] has proposed that the volume fraction of pre-existing cavities can be determined experimentally as a function of strain. However, Chokshi [3] and Jiang [4] reported that there were no obvious evidences to support the concept of pre-existing cavities.

Two cavity growth mechanisms were established: vacancy diffusion-controlled growth and plasticity-controlled mechanism. For diffusion-controlled mechanism, the cavity growth occurs by diffusion of vacancies into cavities through grain boundaries, which results in small spherical cavities. For the plasticity-controlled mechanism, cavity growth operates by deformation of the surrounding matrix. Both experimental evidences and theoretical models show that the plasticity-controlled growth mechanism is responsible for most of the cavity growth in superplastic alloys.

The overall level of cavitation at a given strain will be decreased as temperature increases and the strain rate decreases. But, there was also a report for Al 5083 that increasing

the temperature leads to the increasing of cavitation [5]. The influence of grain size, rolling direction and particle distribution were also investigated [6-8] and the superimposition of hydrostatic pressure will retard the cavity nucleation by increasing the size of a stable cavity nucleus [9].

Cavity stringers were formed either along the tensile axis or along the rolling direction in a few superplastic alloys. In Cu - 2.8Al - 1.8Si - 0.4Co alloy [13] and Zn - 22% Al alloy [14], changing the direction of gauge length aspect to the tensile axis did not influence the alignment of cavity stringers along the tensile axis. However, Caceres and Wilkinson [23] tested Coronze CDA 638 alloy with the tensile axis machined perpendicular to the rolling direction and reported the formation of cavity stringers perpendicular to the tensile axis. The difference between these two alloys is the existence of Co-rich particles in CDA 638, whereas particle-free in Zn - 22%Al alloy. Hence, the role of particles in cavitation behavior needs to be evaluated.

In Al 7475, Bampton and Raj [15] tested under multiaxial stress and reported that the increases in cavitation with plastic strain for all the stress states are nearly the same. The data were limited to $\epsilon_e < 1.4$, and the cavity volume fraction was less than 0.5%. By contrast, a recent investigation of the superplastic Al 5083 showed that under the biaxial stress state, cavity volume fraction was higher than that in the uniaxial stress state [16]. It suggests from these results that a possible difference in cavitation behavior between multiaxial stress states at different strain levels may exist.

Despite these progresses, more work is needed to understand cavitation behavior of aluminum alloys. In particular, the distribution and development of cavities under various stress states are required. Al 5083 has been mostly studied under uniaxial superplastic conditions, and some quantitative information has been reported [5]. In the present study, the behavior of an Al 5083 alloy is investigated under biaxial superplastic conditions by means of a detailed quantitative metallography. A FEM model was also used to calculate the pressure profile so as to maintain the constant strain rate during balance-biaxial superplastic forming. The specific objectives of this research were four-folded.

- To evaluate the influence of the rolling direction on the formation of the cavity stringers in this alloy

- To identify the pre-existence and concurrent nucleation sites for cavitation in Al 5083

- To compare the difference of cavity growth rate between different stress states, the diffusion-controlled cavity growth and the power-law controlled cavity growth operate independently and dominate at the different strain levels

- To examine the cavity interlinkage behavior under different stress states

6.2 Experimental Procedures

Al 5083 alloy used in this study was produced by Sky Aluminum, Japan and received in the form of a cold rolled sheet with a thickness of 2.0 mm. The nominal chemical compositions are showed in Table 6.1. The as-received alloy shows large elongated grains with the appearance of the dendritic structure (Figure 6.1). Complete static recrystallization can be reached by heating up to 555°C in 40 minutes to produce an equiaxed grain structure with an average grain size of $17\mu m$ (Figure 6.2).

Table 6.1: Chemical composition of Al 5083 alloy (wt.%)

Mg	Mn	Cr	Fe	Si	Ti	Al
4.70	0.65	0.13	0.04	0.04	0.03	bal

The uniaxial superplastic testing was performed under a constant strain state of $5x10^{-4}s^{-1}$ at the temperature of 555°C and Al 5083 was expected to exhibit maximum superplastic elongation under that condition. Tensile specimens with a gauge length 12.5 mm were machined from the as-received material with a tensile axis either parallel or perpendicular to the rolling direction. Tensile tests were performed in a vacuum furnace attached to the MTS machine. Tests were interrupted before fracture to measure the growth of cavitation damage with plastic strain. Cavitation was studied in detail by pulling different specimens up to the elongation of 100, 150, 200, 250, 320 (failure), respectively. Unless noted, all the experimental data reported here are for specimens whose rolling direction is parallel to the tensile axis. A few additional experiments were performed in which tensile axis is perpendicular to the rolling direction.

Equibiaxial samples were blow-formed cones in different diameters and trays with stepped geometry. Metallographic samples were cut from bottom centers of both trays and cones, and the 3D corners of a tray were selected to represent an equibiaxial state of stress. FEM simulation was used to calculate the pressure-time profile to maintain the constant strain rate during the biaxial deformation. Uniaxial samples were sectioned parallel to the tensile axis, and biaxial samples were cut in the region formed in the equibiaxial state of stress identified by means of the FEM modeling as well as the shape change of the meshes etched on the sheet surface prior to forming.

The uniaxial and biaxial specimens were metallographically polished, and microstructurally examined for cavitation after the cavity measurement by desitometrical technique. Great care was taken in the polishing process to provide the scratch-free surface that is suitable for the quantitative measurement of cavitation. Because the distribution of cavities changes with thickness and fewer cavities shows in the outer layer (Figure 6.3). A substantial amount of materials were removed to show the cavitation in the center part. The final stage of polishing was conducted with $0.05\mu m$ diamond paste using a very low pressure. Metallographic examination of cavitation was performed using both scanning electronic microscopy (SEM) and optical microscopy. Several sections from each metallographic specimen were

examined by SEM and 10 - 15 photographs taken from it were analyzed for quantitative evaluation and averaging. IMIX image analysis system was used to give the information of cavity dimension, shape, orientation, and number, in which the minimum cavity radius was set as 1.7 μm. Densitometry was also used to measure the extent of cavitation. To identify the nucleation site and grain boundary features, some of the polished specimens were anodized with 50% methynol, 48% water, and 2% HF, 30 A DC current in 1 min. X-ray diffractometer was used to identify the composition of particles.

6.3 EXPERIMENTAL RESULTS

The development of cavitation was studied at the constant strain rate of $5 \times 10^{-4} s^{-1}$. The samples that were deformed to a different strain level were examined by SEM and optical microscopy in terms of size, shape and distribution of cavities. In the following sections, we first discuss the results from the uniaxial specimens with the tensile axis parallel to the rolling direction.

6.3.1 The micro-structural observation of cavity nucleation

To obtain the information of the preferred nucleation site of cavities, several specimens tested to different strains both biaxially and uniaxially were anodized and examined by scanning electronic microscope and optical microscope.

Figure 6.4 is the optical microphotograph of the as-received material after thermal-mechanical treatment for grain refinement. Particles with the biggest radius up to 10 μm are aligned in a direction parallel to the rolling direction. The particles were identified as Al_6Mn by Philips Xpert X-ray diffractometer. Higher magnification indicates that the large particles were broken up, and cavities were formed (A) between the crashed sections, as well as (B) around the large particles. These pre-existing cavities are aligned in a direction parallel to the rolling direction.

After complete static recrystallization by heating to 555°C in 40 minutes, the size and the number of pre-existing cavities were reduced. Density measurement of this specimen shows 0.06% less than that of the specimen cut from grip area where the static hydraulic pressure was applied under which the pre-existing cavities could be eliminated. Figure 6.5 shows the same specimen observed by scanning electronic microscope after recrystallization without deformation. It can be noted that cavity was generated in the vicinity of large particles, but absent around the small precipitate particles. There are clear evidences that cavities pre-existing around particles. However, detailed observation indicates that the pre-existing cavities are not very common owing to the generation of cavities only around some of the large particles. Considering the population of cavity after deformation, the pre-existing cavity does not play an important role.

Figure 6.6 is an optical microphotograph from a specimen anodized and observed with DIC. It indicates that when the alloy was deformed to the strain of ϵ=0.66 biaxially, cavities were observed at the triple points of grain and on the grain ledge. Inspection at higher magnification with scanning electronic microscope, the microphotograph (Figure 6.7) of the specimen pulled to an elongation of 260% shows that the particles distribute along the cavities which developed along the grain boundaries. Detailed observation suggests that large particles existed inside the grain without the appearance of cavities, and there was no evidence for cavity pre-existing around particles with size of $< 0.5\mu$m(???) after heating to 555^oC in 40 minutes, during which static recrystallization completed.

Scanning electronic microscope was used to observe the preferred nucleation site for cavities at different strain level under both stress states and Figure 6.8 is a montage of a specimen biaxially stretched to the strain level of ϵ=0.75(Figure 6.9), where a large particle labeled A was located on the grain boundary. Detailed inspection indicates that large particles in the grain were not associated with the presence of cavity shows that cavities were generally related to the particles located on the grain boundary

subsectionThe formation of cavity stringers and the development of cavity under different stress state

Several specimens were examined to determine the influence of the rolling direction, the tensile axis, and the stress states on the cavity stringers. Essentially, similar trends were found under both stress states. General comments concerning the appearance of cavitation in these samples: For all of the samples examined microscopically, there was a maximum level of cavitation near to the fracture tip and a decrease in the extent of cavitation with increasing the distance from the point of fracture under both stress state. Cavity stringers can be identified as parallel to the rolling direction in all the cases. On the other hand, cavity growth rate, density of number, and morphology appears different in uniaxial stress state from those in biaxial stress state.

Figure 6.9 shows the montage of the polished specimen stretched to $\epsilon = 0.4$ under the equibiaxial stress state, in which the rolling direction is horizontal. The formation of cavity stringer is very evident, and the cavities are essentially rounded with the maximum radii of 8 - 10 μm. Inspection at higher magnification gave limited evidence for cavity interlinkage along a direction both parallel and perpendicular to the rolling direction. Figure 6.10 depicts the development of cavitation of tensile specimens pulled to, (a) $\epsilon = 0.8$ with the gauge length parallel to the rolling and (b) $\epsilon = 0.6$ with the gauge length perpendicular to the rolling direction. The tensile axis is horizontal in both of these two microphotographs. Cavity stringers parallel to the rolling direction still could be identified in both of these two microphotographs.

In all these three pictures, the alignment of cavities in stringers parallel to the rolling direction can be observed. It is noted that at lower strain levels ($\epsilon < 0.6$), under both of the stress states the morphology of the cavities appear to be spherical and limited interlinkage along the rolling direction can be observed in Figure 6.9 and Figure 6.10 (b). At higher strain level, $\epsilon = 0.8$, the cavity interlinkage occurs along both direction. Comparing the

three photos it can be found that with the increasing of strain levels the cavity stringers become more and more unclear.

The appearances of cavity at higher strain, $\epsilon = 0.85$, under (a) uniaxial stress state, and (b) biaxial stress state are presented in Figure 6.11 with the rolling direction horizontal. The cavity stringers are masked due to the interlinkage of cavities, which can be observed in both microphotographs. It can be also noted that the interlinkage appears not only in the direction parallel to the rolling direction (A-A), but in the transverse direction (B-B). A comparison of (a) and (b) reveals that the interlinkage is more serious in uniaxial state than that in the biaxial state, but the number density of cavities appears more in the biaxial stress state.

The quantitative data obtained using densitometry, and IMIX image analysis are summarized in Figure 6.12 (a) in the form of cavity area fraction versus equivalent true strain, and Figure 6.12 (b) the top ten cavities mean area versus equivalent true strain for specimens deformed in both stress states. Top ten cavities mean size can represent the growth rate. Essentially, the data for biaxial state are higher than that in the uniaxial stress state. The growth rate in both plots shows faster in biaxial stress state. Figure 6.13 illustrates the variation of the density of cavity number with strain. Cavity number continuously increases with strain, and at a specific strain level, cavities are more in biaxial state.

Figure 6.14 illustrates the cavity size distribution at a specific strain level, $\epsilon = 0.7$. It is clear that at both stress states, small cavities are more. The two plots intersect at radius of 4.2 μm, exhibiting higher in biaxial stress state, and the size distribution shows that more small cavities. The size distribution line in uniaxial state intersects with that of in the biaxial state, suggesting that more large cavities appearing in uniaxial state, which is consistent with the result showed in Figure 6.6.

Figure 6.15 is an optical photomicrograph near the fracture tip and shows the occurrence of grain boundary cracking in a uniaxial specimen elongated to failure. Higher magnification scanning electronic photomicrograph (Figure 6.16) illustrates clearly the development of cavities at particles along with the occurrence of the grain boundary cracking. It is important to note that, as observed in copper and Al Cu Li - Zr alloys [3,14], the grain boundary cracking was not observed at the early stage of deformation but only at the later stage. Comparison of the two stress states indicates that the crack-like cavities occurs at lower true strain than that in the biaxial state.

By comparing the cavity morphology under both stress states at different strain levels, it can be noticed that more cavities were generated at biaxial state, but the interlinkage occurred earlier at uniaxial state. This observation is constant with the plots in Figure ??. Microsection taken from the uniaxial fracture tip shows that a small number of cavities were generated in uniaxial stress state, but the cavities do interlink to very large sizes leading to failure. On the other hand, microphotographs taken from the biaxial near fracture tip appears more and the same large cavities. This may suggests that more cavities were nucleated in the biaxial stress states. Measurement of the thickness at both fracture tips indicates that the failure thickness are 0.87, 0.69 for uniaxial and equibiaxial stress state

respectively.

6.4 DISCUSSION

6.4.1 Pre-existing cavities and cavity nucleation

Several models was established on the assumption of the presence of the pre-exist cavities generated during the thermal-mechanical process used to refine grain, but very few experimental evidence were provided [19], owing to the small size of pre-existing cavities and low resolution of optical microscope. In previous work, the presence of large pre-existing cavities ($> 1\mu m$) were found in Al-4.5Mg-0.5Cr and Pb - Sn alloys [20]. Most of the superplastic alloys did not show the large pre-existing cavities, but the presence of smaller pre-existing cavities with the dimensions less than $0.1\mu m$ can not be ruled out.

The present work shows the clear evidence of the existence of the pre-existing cavities at the interface between matrix and Al_6Mn particles. During the cold rolling process, these particles break up into stringers parallel to the rolling direction. The plasticity of the matrix is not so high that the discrepancy was produced at the interface, and the broken of the brittle particles induced the pre-existing cavities between the particles. These cavities with the radii up to 5 μm ware only observed around very large particles, and these large cavities were significantly sintered during the process of static recrystallization prior to superplastic deformation. As noted by Chokshi and Mukherjee [9], the sintering of the cavity is essentially the reverse process of the diffusion controlled cavity growth. Therefore, the equation 6.1 used to determine the total time necessary to complete sintering was deduced from the diffusion controlled growth equation.

$$t = \frac{\Phi k T r^4}{\Omega \gamma \delta D_{gb}} \qquad (6.1)$$

where K is the Boltzmanns constant; T is the absolute temperature; Ω is the atomic volume; δ is the width of the grain boundary; γ is the surface energy; D_{gb} is the coefficient for the grain boundary diffusion and Φ is a constant having a value of ~ 0.6. For aluminum based alloys, taking $\Omega = 1.66 \times 10^{-29} m^3$, $\gamma = 1.1 Jm^{-2}$, $\delta D_{gb} = 5 \times 10^{-14} exp(-84,000/RT)m^3s^{-1}$, and $T = 828K$. Assuming a pre-existing cavity with $r = 0.5\mu m$, the calculation using equation 6.1 reveal the complete sintering time of this cavity is $\sim 3520s$. This sintering time is close to the period of time used to uniform the testing temperature. But, for the cavities with $r = 5\mu m$, the total sintering time will be $\sim 3.5 \times 10^7$. The calculation from Jiang et al. for Al 7075 alloy shows that the total sintering time for a cavity with $r = 0.05$ is $\sim 0.03s$ [4]. It can be suggested from above analysis that small pre-existing cavities observed in the post recrystallization samples will be completely sintered out at the superplastic temperature before deformation. The pre-existing cavities with $r > 0.5\mu m$ could act as nucleation site in the subsequent superplastic deformation. In the present test, large cavities were observed around the coarse constituent particles, which can be considered as the nucleus of the cavitation.

It is important to note, however, that the pre-existing cavities are not the only nucleation source and probably not the main one. There are three evidences revealing that the cavities continuously nucleated during the deformation process.

First, it can be observed from Figure 6.4 and Figure 6.10 (a) that number of the pre-existing cavities with $r > 0.5\mu$m in the undeformed sample are significantly less than total cavity number in deformed. Figure 6.13 shows that the cavity number density increases with strain and the cavities show a wide range of size (Figure 6.10 (b)). This implies that the cavities are nucleated continuously throughout the deformation.

Second, the predicted results by using

$$V = V_0 exp(\eta\epsilon) \tag{6.2}$$

where V_0, the pre-existing cavity volume fraction, was measured as 0.06 for Al 5083 by desitometry, and h, the material constant, equals 1.47 at 555°C. Figure 6.12 (a) shows that the experimental result is higher than the calculated result. Equation 6.2 was established on the assumption that all the cavities are pre-existed. This discrepancy may suggest there are additional nucleation mechanism.

From the experimental results, it can be noticed that in tensile test, a change in the in orientation of the rolling direction with respect to the tensile axis will lead to a corresponding change in the direction of alignment of the cavity stringers. In the biaxial stress state, cavity stringers are also aligned in a direction parallel to the rolling direction. So, it suggests that the concurrent nucleation mechanism is also related to the particles. A possible mechanism for the formation of cavity stringers parallel to the rolling direction was proposed by Chokshi and Mukherjee [9]. In this mechanism, the sliding along the grain boundary will lead to the large elastic stress concentration at the apices of the particles which hinder sliding. Due to the rapid intercrystalline diffusion creep processes, small particles will generally not experience any significant stress concentrations and, consequently will not prone to nucleate cavities. At superplastic temperature, the localized Coble diffusion creep around the large particles involves the interphase diffusion coefficient and not the intercrystalline grain boundary diffusion coefficient. Since the interphase diffusion coefficient may be several orders of magnitude smaller than the grain boundary diffusion coefficient. The large stress concentration may not be relaxed around these particles and, thereby the cavities were nucleated. The mechanism is essentially consistent with the present observations. Both optical (Figure 6.6) and scan electronic microscope microphotograph (Figure 6.16) show the cavities located at the triple points and grain ledge.

6.4.2 The influence of stress states on the cavity growth rate(behavior)

A fundamental issue for cavity growth is whether the criterion for intergranular cavitation should be described in terms of the mean stress or the maximum principal stress. Theories suggest that the diffusion dominated cavity growth is controlled by maximum principle stress,

which differs little in uniaxial and balanced-biaxial, therefore in this stage the cavity growth rate is essentially identical in both stress states; whereas the power-law dominated cavity growth, which is the main cavity growth mechanism, was controlled by the mean stress that vary by a factor of two between uniaxial and balanced-biaxial stress state, therefore the cavity growth rate should be higher in the biaxial state of stress. The cavity growth rates per unit strain, $\frac{dr}{d\epsilon}$, for these two mechanisms are given by the following expressions: (a) diffusion cavity growth in superplasticity [21]:

$$\frac{dr}{d\epsilon} = \frac{\Omega \delta D_{gb} \left(\sigma - \frac{2\gamma}{r}\right)}{5r^2 kT\dot{\epsilon}} \tag{6.3}$$

(b) power-law growth [6]:

$$\frac{dr}{d\epsilon} = \frac{\eta}{3}(r - \frac{3\gamma}{2\sigma_e}) \tag{6.4}$$

The parameter η in equation 6.4 can be readily extended to multiaxial states of stress. It can be shown that [6,22]:

$$\eta = \frac{3}{2}\left(\frac{m+1}{m}\right) sinh \left[\frac{2}{3}\left(\frac{2-m}{2+m}\right) k_s\right] \tag{6.5}$$

where, the geometric constant, k_s, changes with stress states. It has been shown that if 50% of superplastic strain is attributable to grain boundary sliding, then $k_s = 1.5$ and 2.25 for uniaxial and equibiaxial straining. Based on this, the parameter, η, can be calculated as 2.25 and 3.59 for uniaxial and equibiaxial stress sate respectively. By using parameters shown in 4.1 and η, equation 6.3 and equation 6.4 were evaluated for $\sigma = 6MPa$, and the results are shown in Figure 6.17 as a logarithmic plot of $\frac{dr}{d\epsilon}$ vs. r.

Since these two mechanisms operate independently, cavity growth is controlled by the one having the highest value of $\frac{dr}{d\epsilon}$. Inspection of Figure 6.17 reveals that the power -law controlled mechanism started to dominate earlier in biaxial stress state with the critical cavity radius ($\sim 1\mu m$) smaller than that in uniaxial stress state, and the growth rate is higher. Since the low resolution of the optical microscope and the minimum cavity radius was fixed as 1.7μm in image analysis system, the morphology data was in the range of power-law controlled growth, thereby, the diffusion controlled mechanism is not important in this experiment. It can be noticed in Figure 6.12 (a) that both the cavity volume fraction and the increasing rate of it are higher in equibiaxial stress state than those in the uniaxial stress state. This is consistent with the prediction the Figure 6.17.

6.5 CONCLUSIONS

1. An Al-Mg-Mn-Cr alloy were deformed under both uniaxial and equi-biaxial stress state at a constant strain rate of $5x10^{-4}s^{-1}$ to compare the difference of cavity nucleation, growth and interlinkage behavior.

2. The pre-existing cavities were observed in the vicinity of Al_6Mn particles in the post recrystallization material. The increase in the number density of cavities with strain and the wide range of cavity size at different strain levels suggests that the cavities nucleated continuously around the particles on the grain boundary during superplastic deformation, and the pre-existing cavities did not play an important role.

3. In the early deformation stage, the alignment of cavity stringers formed always in a direction parallel to the rolling direction due to the Al_6Mn particles lying in a stringer parallel to the rolling direction. At large strain level, the concurrent nucleated cavities and the interlinkage of cavities tends to mask the alignment of the cavity stringers.

4. Cavity volume fraction obtained from density measurement, and number density, size distribution obtained from image analysis indicated that the cavity growth rate is higher in the equibiaxial stress state than that in the uniaxial stress state.

5. The failure of the material occurred earlier in the uniaxial stress state than that in the equibiaxial stress state since in the uniaxial stress state, cavities were more prone to interlink. Stress analysis indicated that in the interlinkage area, higher stress concentration can be produced in the uni-axial stress state.

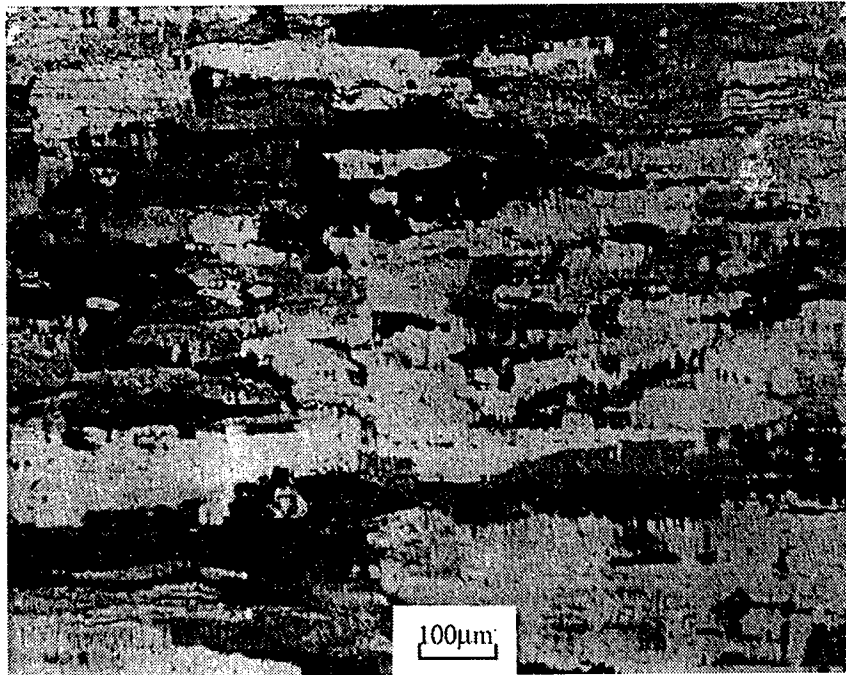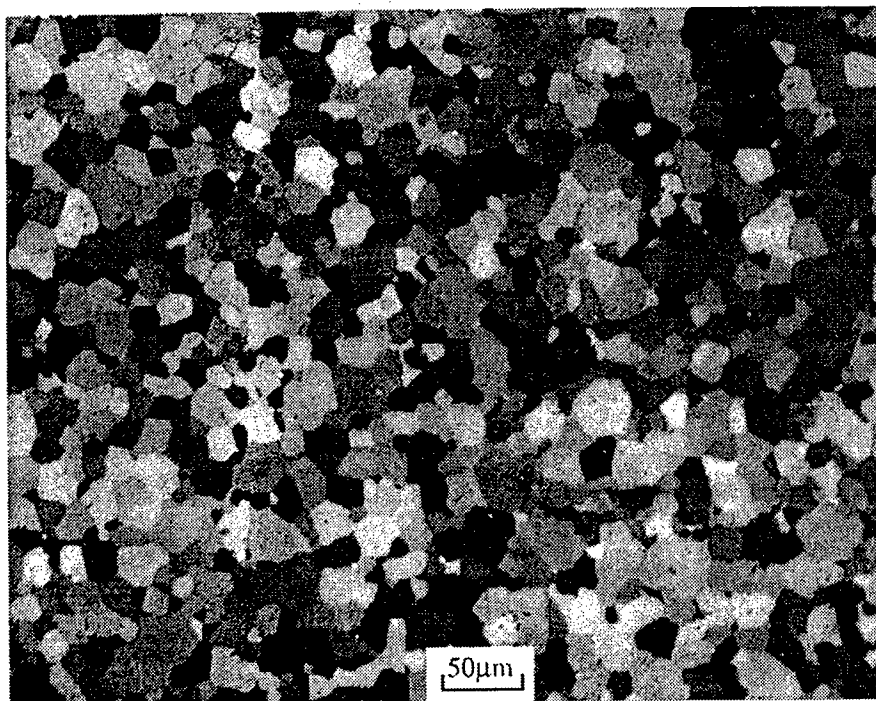Figure 6.1: DIC optical microphotograph of the as-received material showing elongated dendritic structure.

Figure 6.2: DIC optical microphotograph showing equiaxed grain with the diameter of $17\mu m$ after recrystallization, 40 minutes, heating to 555^oC.
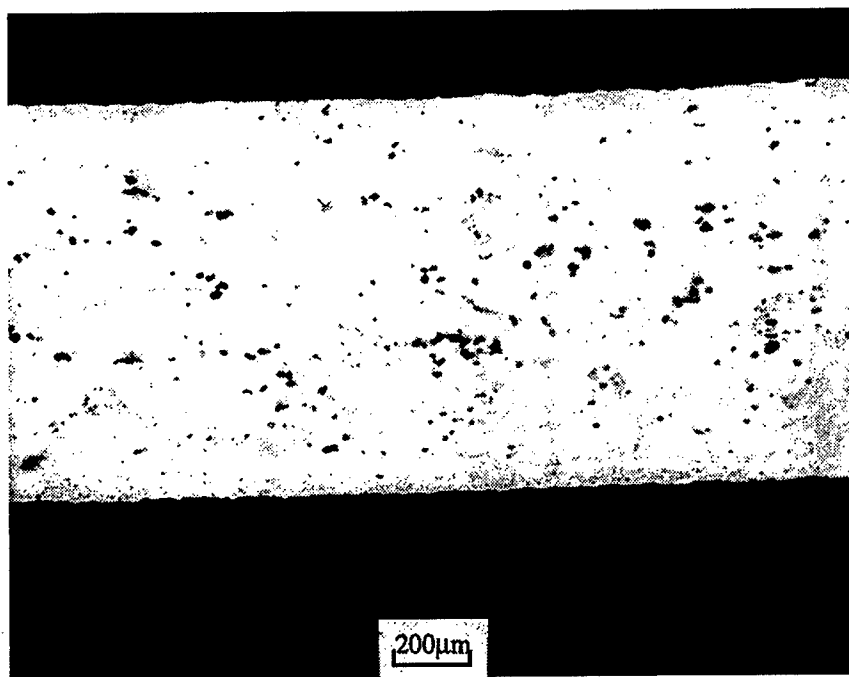
Figure 6.3: The disuniform distribution of cavities along the thickness direction indicates more cavities in the center.

Figure 6.4: Particles alignment in a direction parallel to the rolling direction, pre-existing cavities can be found both around the large particles (a), and between the broken sections of large particles (b). The rolling direction is horizontal.
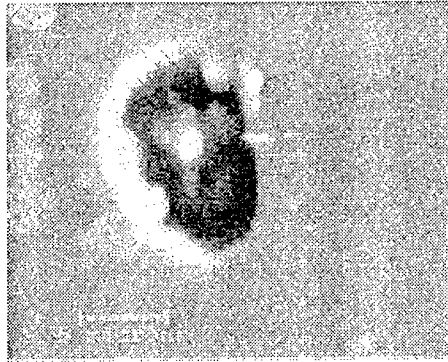
Figure 6.5: SEM microphotograph shows that the pre-existing cavity was not completely sintered out after recrystallization.
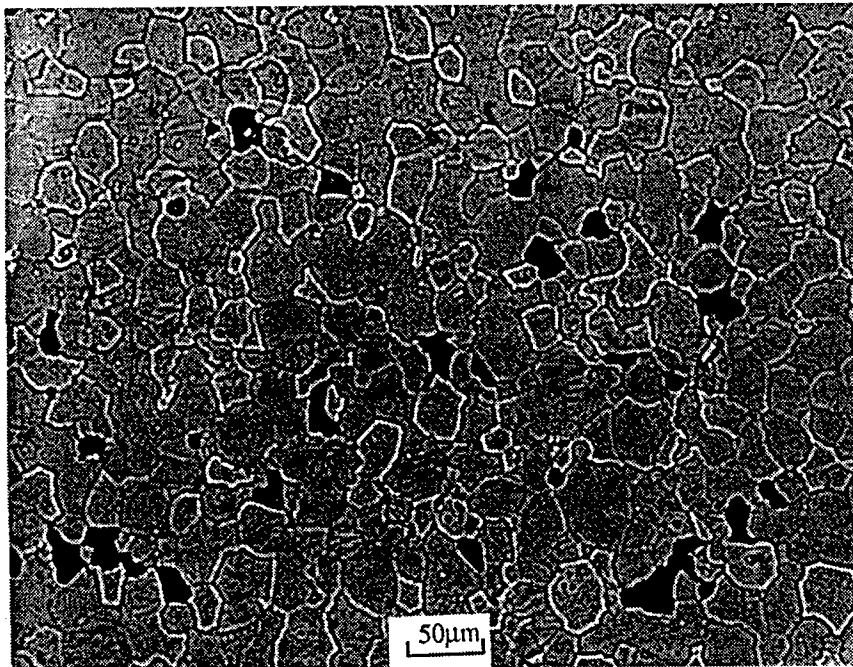
Figure 6.6: DIC optical microphotograph, equibiaxially formed to e=0.66, revealing cavities developing at the triple points and the grain ledge.
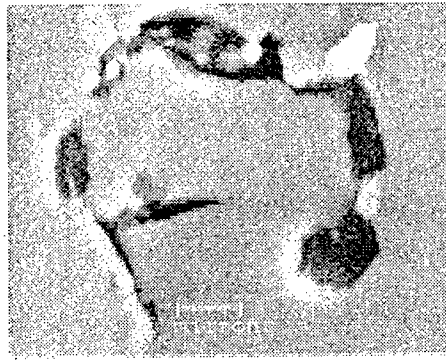
Figure 6.7: SEM micro photograph showing that the cavity developed along the distribution of particles.
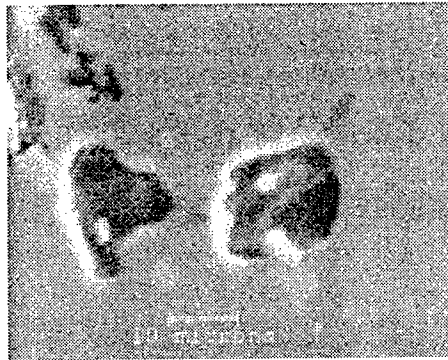
Figure 6.8: SEM microphotograph shows cavity developing around the large particles.
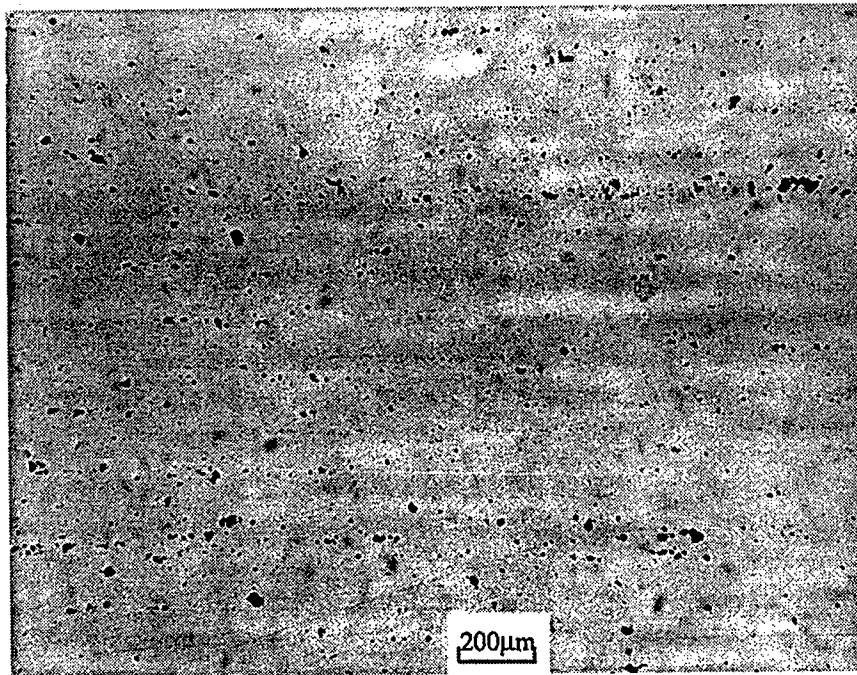
Figure 6.9: Cavitation after equibiaxially formed to $\epsilon = 0.4$, showing cavities stringers aligned in a direction parallel to the rolling direction. The rolling direction is horizontal.
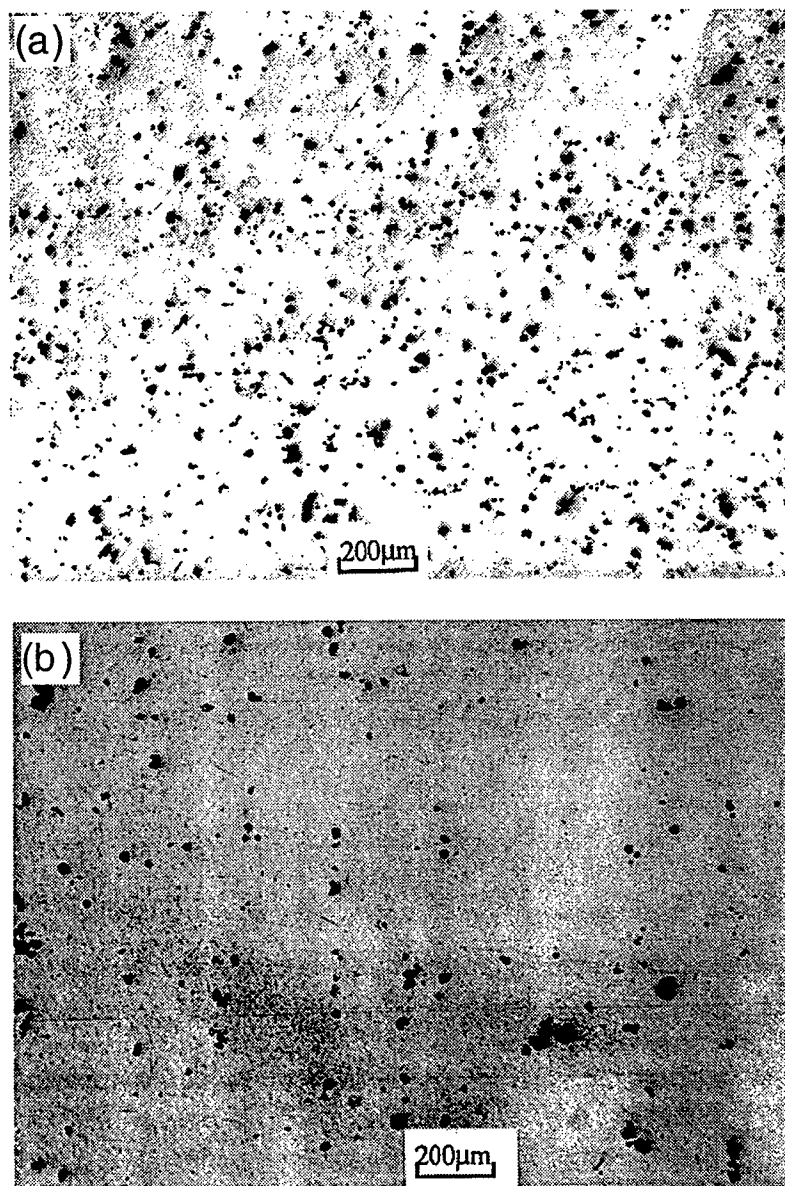
Figure 6.10: Microphotograph of tensile specimen pulled to (a) $\epsilon = 0.8$ with gauge length parallel to the rolling direction, (b) $\epsilon = 0.6$ with the gauge length perpendicular to the rolling direction, revealing that the cavities always aligned in the rolling direction.
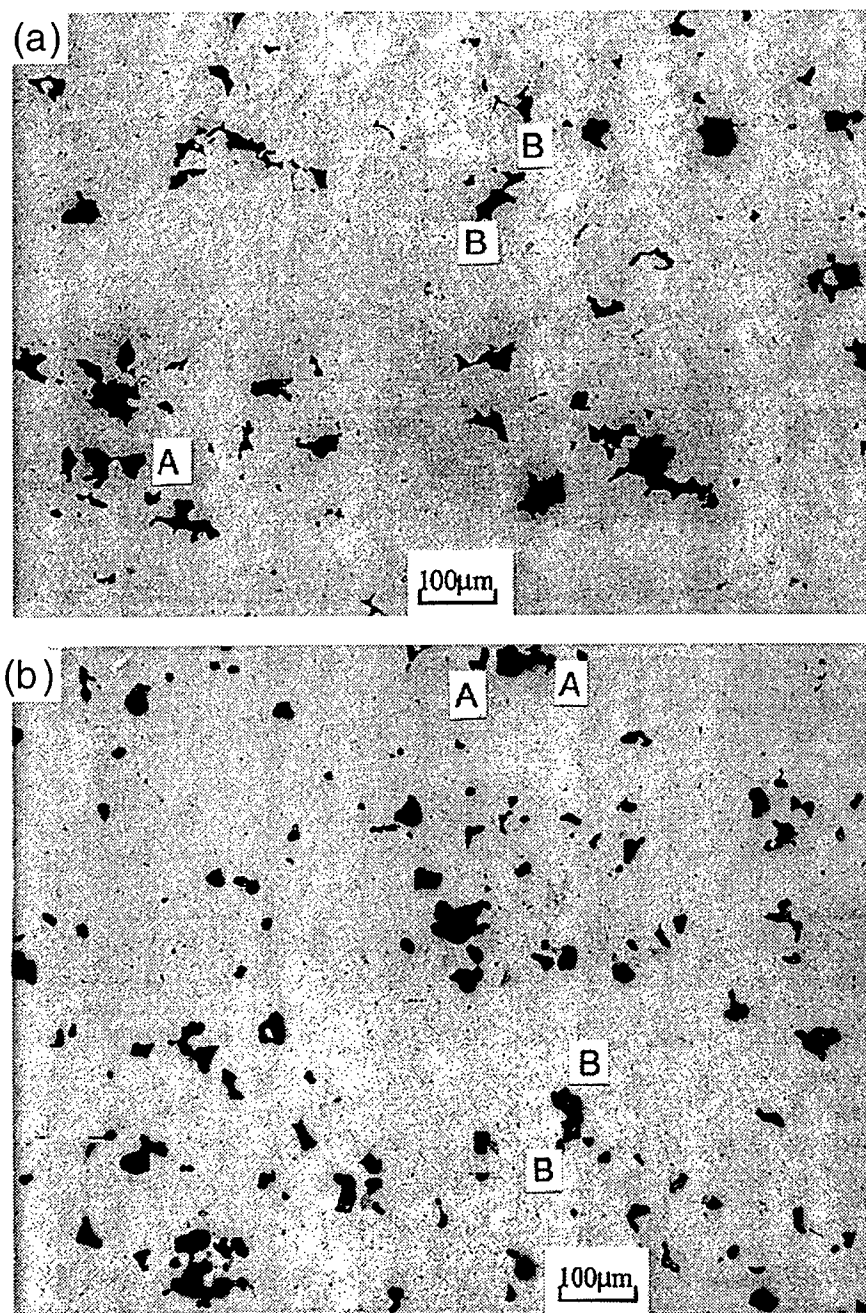
Figure 6.11: After a strain of e=o.85 under (a) uniaxial stress state, and (b) biaxial stress state, cavity interlinkage occurred in directions both parallel and perpendicular to the rolling direction. The rolling direction is horizontal.
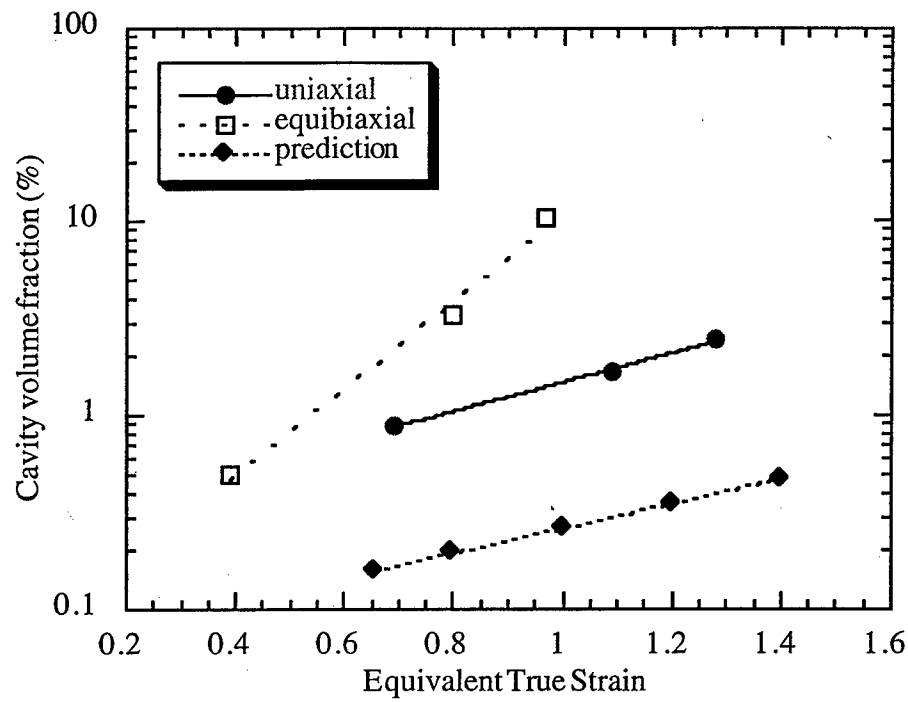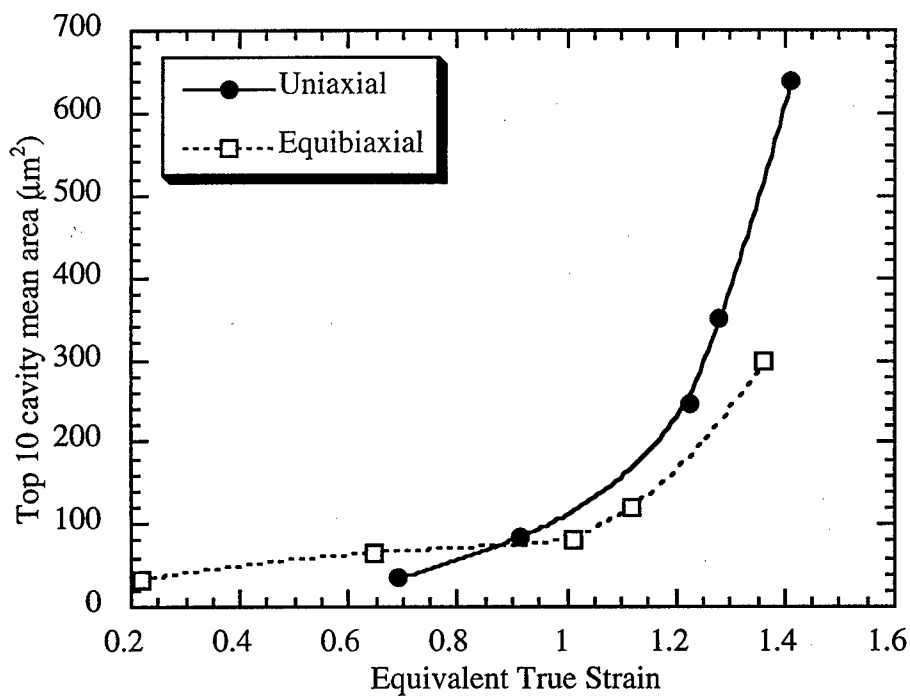
Figure 6.12: Cavity growth rate showing difference under unaxial and biaxial stress by (a). the variation of cavity volume fraction with strain, and (b). the variation of top 10 cavities mean ares with strain.
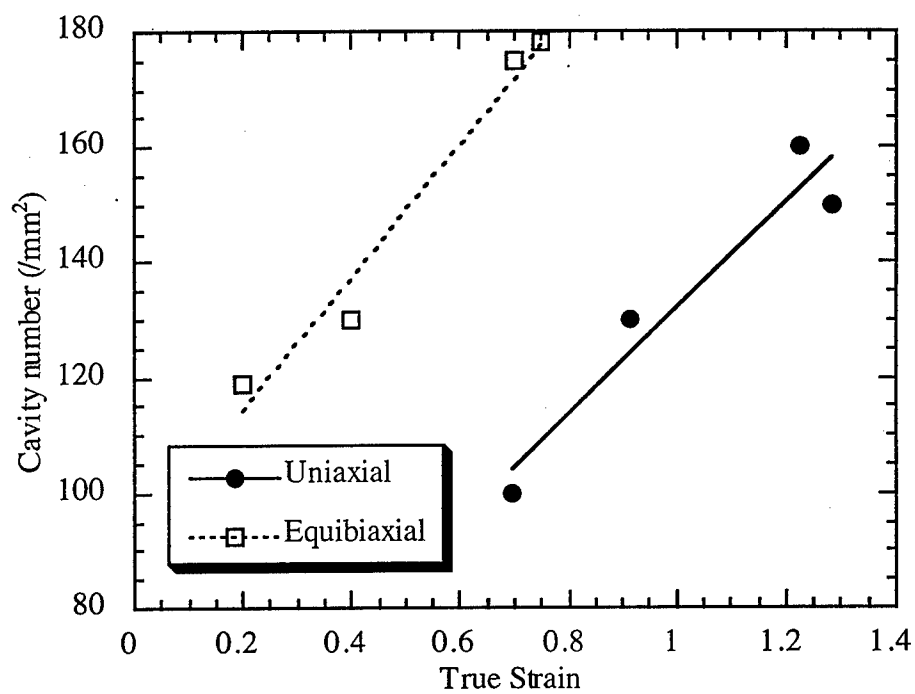
Figure 6.13: The population of cavity increasing with strain but showing different increasing rate under unaxial and equbiaxial stress rate.
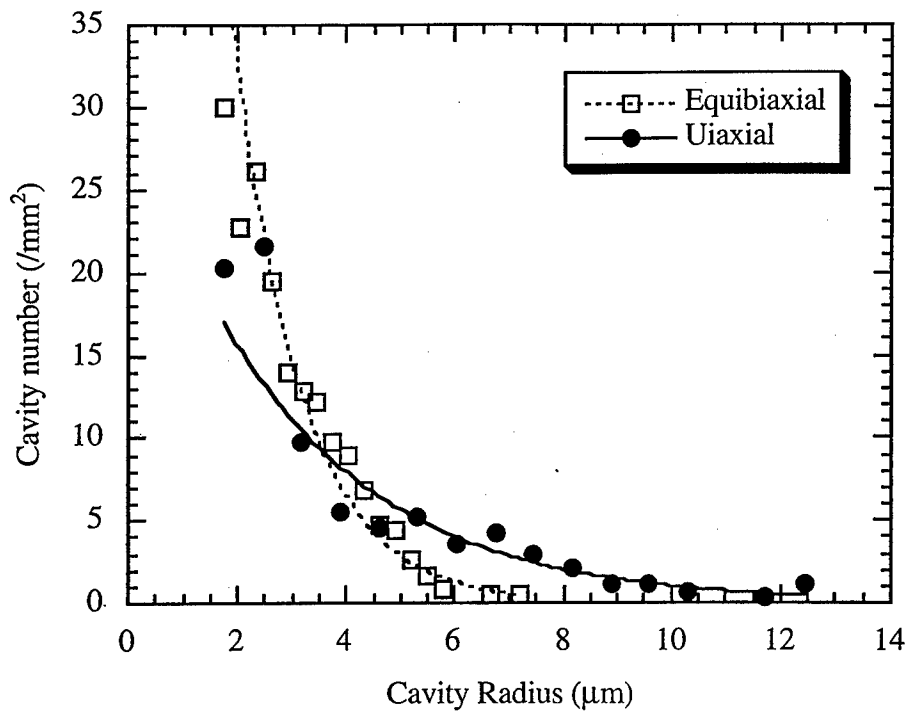
Figure 6.14: The cavity population distribution at $\epsilon = 0.75$ under two different stress states.
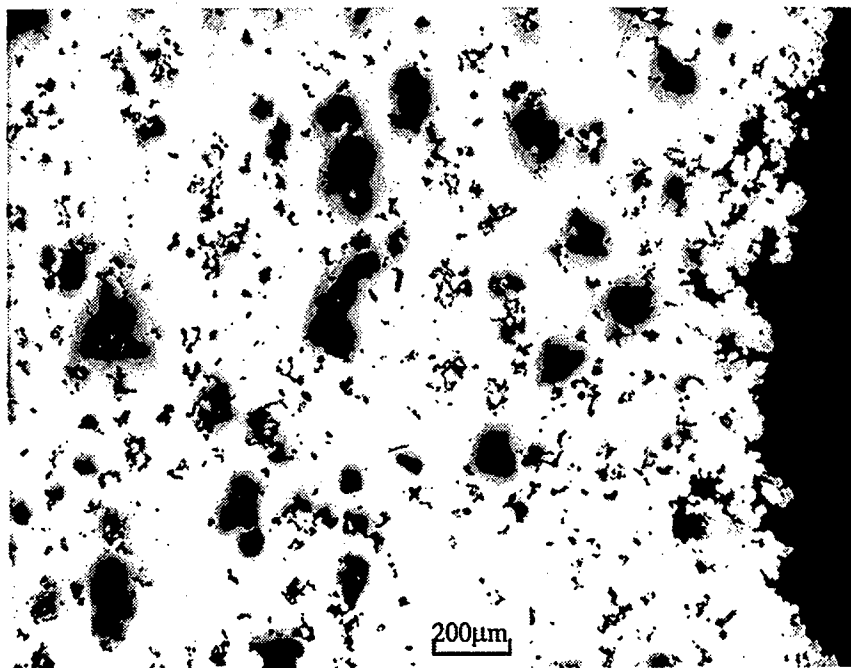
Figure 6.15: Fracture tip showing the interlinkage of cavities along the a direction perpendicular to the tensile axis leading to the failure.
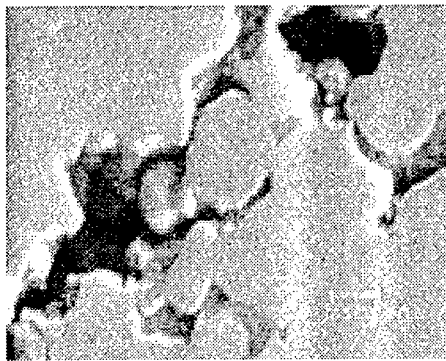
Figure 6.16: The crack-like cavities formed by developing along the grain boundaries.
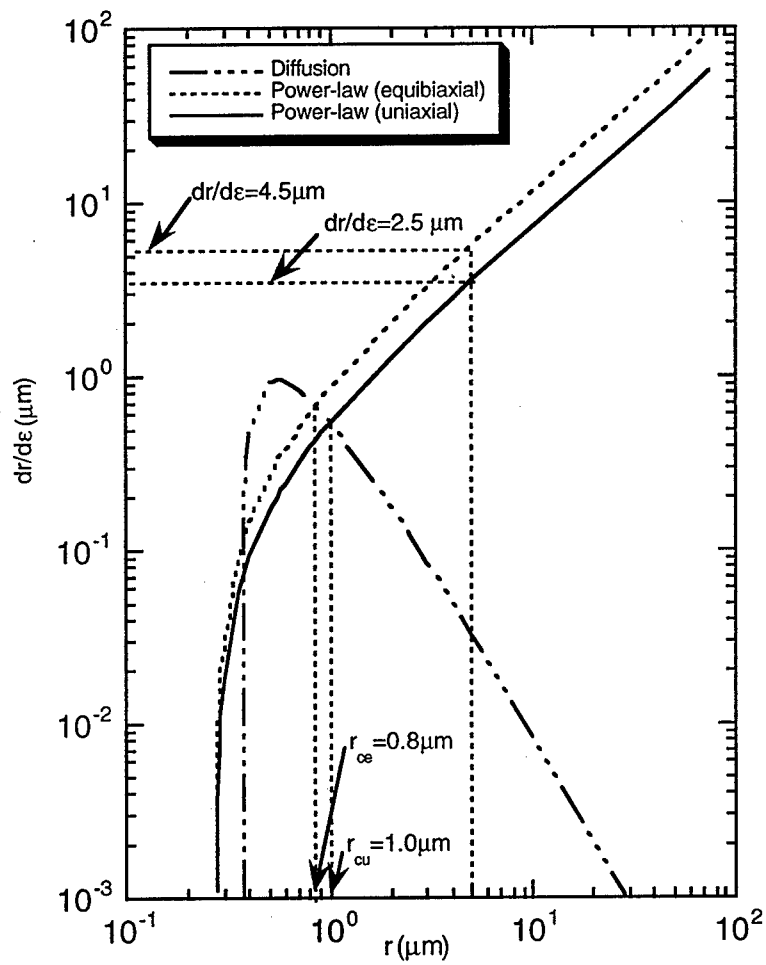
Figure 6.17: The variation of cavity growth rate with cavity radius for specimens deformed under different stress states. The theoretical curves are shown for the diffusion, and power-law controlled mechanisms.

REFERENCES

1. Z. C. Wang, T. J. Davies, and N. Ridley, Cavitation in superplastic metals. Materials Science Forum, 170-172 (1994), 177-186.

2. M.J Stowell, Cavitation in superplasticity, in N. E. Paton and C. H. Hamilton ed. Superplastic Forming Of Structural Alloys, Pp. 321-336.

3. A. H. Chokshi and A. K. Mukherjee, Acta Metallurgica, 37 (1989), 3007-3017.

4. Jiang, X.G, Cui, J. Z, and Ma, L. X, Acta metall., 41(1993), 2721-2727.

5. H. Iwasaki, K. Higashi, S. Tianmura, T. Komatsubara and S. Hayami, in Superplasticity in Advanced Materials (1991), 447-452.

6. J. Plling and N. Ridley. Superplasticity in Crystalline Solid, pp. 114-158.

7. A. H. Chokshi and T. G. Langdon, Acta Metall. Mater., 37 (1989), 715-723.

8. J. S. Wang, J. J. Stephens and W. D. Nix, 33 (1985), 1009-1021.

9. A. H. Chokshi and A. K. Mukherjee, Mater. Sci. Engng., A171 (1993), 47-54.

10. H. Imamura and N. Ridley, Superplasticity in Advanced Materials (1991) 41-458.

11. R. Verma, P. A. Friedman, A. K. Ghosh, C. Kim and S. Kim, J. Mater. Eng. Perform., 114 (1995) 543-550.

12. K. Kannan and C. H. Hamilton, Scripta Materialia, 38 (1997) 299-305.

13. A. H. Chokshi, Metallurgical Transactions A, 18A (1987), 63-67.

14. A. H. Chokshi and T. G. Langdon, Acta Metallurgica, 37 (1989), 715-723.

15. C. C. Bampton and R. Raj, Acta Metall. Mater., 30 (1982), 2043-2053.

16. M. A. Khaleel, M. T. Smith and A. L. Lund, Mater. Sci. Forum, 243-245 (1997).

17. A. H. Chokshi, and A. K. Mukherjee, Mater. Sci. Engng., A110 (1989), 49- 60.

18. A. H. Chokshi and T. G. Langdon, Acta Metallurgica et Materialia, 38 (1990), 867-877.

19. C.C Bampton andJ. W. Edington, Metall., 37 (1989), 3307.

20. D. J. Lloyd and D. M. Moore, Superplastic forming of structural alloys, Pp. 147-169 (1988)

21. M. V. Speight and W. Beere, Met. Sci. j., 9 (1967) 190.

22. Pilling, J.; Ridley, N. Effect of hydrostatic pressure on cavitation in superplastic aluminum alloys. Acta Metall. Mater., 1986; 34: 669-679.

24. C. H. Caceres and D. S. Wilkiinson, Acta Metall., 32 (1984), 423.

Chapter 7

Design and Implementation of Internet Based Integrated Design System

7.1 INTRODUCTION

Software designers have to consider three dimensions of integration while integrating different components that run on different platforms. They are the control dimension, the data dimension and the user interface dimension [10]. The control dimension of an integrated system determines its communicational ability, *i.e.*, the degree to which it communicates the findings and actions to each component, and the degree to which it provides means for the components to communicate with it. This includes the temporal aspect of immediate notification and the selective aspect of communication with a particular component. The data dimension of an integrated system determines the degree to which data generated by one component is made accessible and is understood by other components. The user interface dimension of an integrated system is the degree to which different tools present a similar external look-and-feel, and behave consistently in similar situations.

There are two emerging classes of integrated systems that operate across network:

- Multi-function systems that execute multiple applications concurrently.

- Multi-mode systems that offer users alternative modes of operation but not concurrently. These systems perform a single function at a time but can change the way they operate depending on the intermediate results.

This paper focuses on the multi-mode systems that include tightly coupled hardware and software components. The design of such a system requires the use of a diverse set of concepts such as network programming, security, and coordination.

A framework, which forms the basis of this paper, explores the viability of extending a multi-mode integrated system over the Internet. The benefit is unprecedented: the integrated system will be available to any user located anywhere in the world unlike most of the integrated systems that are available only over the Intranet. This framework uses client/server techniques and queuing procedures to handle requests from web clients; invokes the components in the proper order while coordinating the communication and the results; and displays the textual and graphical results via the Internet. The use of client/server techniques to perform distributed computing is not new; however, implementing such a system in the background of a web interface is new and it brings with it a host of new problems.

The primary objective of this research is to design and implement a framework for developing an Internet-based Integrated Design System (IBIDS). For the purpose of demonstration, a distributed mechanical engineering application has been selected. This application is used in the design and manufacture of engineering products using superplastic forming process (SPF) [1]. This research involves both computer science (integration, user interface, etc.) and mechanical engineering concepts. Only the former is addressed in this paper. Also, we are concerned with only the input and output from the individual components (software applications/tools) and not with the actual working detail of the tools themselves. Section 7.2 of this paper discusses the features of IBIDS. Section 7.3 provides the information on the design methodologies for developing an integrated system, web programming concepts and web security issues. Section 7.4 presents the rationale behind our design decisions, the framework of IBIDS, and the implementation details of the application. Section 7.5 contains the concluding remarks and the direction of the future research.

7.2 FEATURES OF IBIDS

Many business, scientific and engineering applications require user interaction for valid input data, invocation of different components in a specific sequence and the presentation of results in many different formats. To accommodate the above generic requirements, the IBIDS framework has been designed to include the following features:

- A web user interface

- User authentication

- Input data validation

- Notification of an approximate response time to the users

- Statistical data collection for estimating turnaround time

- Invocation of different software running on different platforms in the proper order

- Textual and graphical display of results

- Flexible design to incorporate additional components to the system

In addition to implementing these features, IBIDS carefully addresses the security problems omnipresent in all web applications.

7.3   ISSUES IN THE DESIGN OF IBIDS

Since IBIDS is implemented over the network, it should also consider the web programming and security concepts apart from the integrated systems design issues. Integrated systems can be implemented in several different ways and the most commonly used methodologies are Client/Server model, Middleware and distributed software agent and are discussed in Section 7.3.1. Sections 7.3.2 and 7.3.3 discuss the concepts involved in web programming and security.

7.3.1   Methodologies for Designing Integrated Systems

The client/server software architecture is a versatile, message-based and modular infrastructure that is intended to improve usability, flexibility, interoperability, and scalability as compared to centralized, mainframe, and time sharing computing. The traditional Client/Server model is used in tightly coupled systems [3].

Middleware is an enabling layer of software that resides between applications and the networked layer of heterogeneous platforms and protocols. It decouples applications from any dependencies on the plumbing layer, which consists of heterogeneous operating systems, hardware platforms and communication protocols by providing its own Application Program Interfaces (APIs) [4]. However, developing APIs for each component is very time/money consuming.

Another promising paradigm for integrated systems is distributed software agents: programs that are autonomous, network aware, and (potentially) move from machine to machine [5]. An integrated system that uses agents is described in reference [2].

7.3.2   Web Programming

Web uses a client/server architecture in which a client uses a web browser to request information from a web server on the Internet. The web server can send two different types of web pages, namely, static and dynamic. A static page has all the data to be displayed by the browser and is typically an HTML document. A CGI (Common Gateway Interface) script invoked by a web server creates dynamic pages and the contents of these pages depend on the client's input into a form. The CGI scripts are written using the scripting languages such as

Perl, Python, Rexx, Tcl, Visual Basic, and the Unix shells with CGI interface [8]. Scripting languages assume that there already exists a collection of useful components written in other languages. They are not intended for writing applications from scratch; they are intended primarily for binding together components.

7.3.3 Web Security

A server program that accesses the host computer's resources can be a source of potential security leaks in the following ways:

- A server that provides read access to its document space may let anyone read any document and this can be avoided by user authentication.

- A server that lets clients to write directly to its document space has to ensure that no one can maliciously alter the document space or introduce viruses.

- A server that allows users to execute programs on the host computer may aid in break-ins to the system is not designed with utmost caution.

As far as security is concerned, our focus is on user authentication, security of server and host environments of the different software components, and data transport between the server and the host environment [9]. We do not address the firewall, electronic commerce, anonymity, and privacy or intrusion detection issues since they are not specific to our design [7].

There are a few kinds of authentication methods used on the Internet which include Basic authentication and Digest Authentication. Basic Authentication uses a conventional username and password that is passed openly across a network [6] and digest authentication uses a shared secret password, but verifies without sending the password openly [9].

There are two fundamentally different approaches to securing data in transit, namely, Secure Sockets Layer (SSL) and Secure-Hyper Text Transfer Protocol (S-http). While S-http marks individual documents as private or signed, SSL mandates the data channel used for communication between the corre-sponding processes as private and/or authenticated.

7.4 DESIGN AND IMPLEMENTATION OF IBIDS

As previously discussed, the interoperability among heterogeneous software and hardware environments, coordination of the component activities, and system security have to be considered in order to design and implement an integrated system. The design of the framework and the rationale behind the selection of the programming language and other design decisions are described in section 4.1. Section 7.4.2 briefly introduces the operating environment

for the mechanical engineering application; and section 4.3 describes the implementation of IBIDS using this framework for the engineering application.

7.4.1 Design of the Framework

From the design point of view, there are three different types of software in IBIDS:

- The web browser A web user sends request to the IBIDS using a web browser through the Internet. Typically a web browser is a client of the web server.

- The web server provides static/interactive web pages upon request and/or passes information to a CGI script.

- The component software/tool individual software component that solves a specific problem. These components may run on machines in the same local area network (LAN) and share the same file system with web server, or they may connect directly to the Internet.

Since a typical scientific or engineering application involves tightly coupled components, the Client/Server technology is best suited and is used in two layers as shown in Figure 1.

- Job submission layer - the web user submits a request with all the required information through the web browser, the web browser is the client and the web server is the server.

- Job processing layer Once the web server gets all the required information, all the component software have to be invoked in the proper order and with proper communication. In this case, the web server is the client and the component software is the server.

The above design unfortunately introduces major security holes since the web server runs as a user nobody with privileges to access any information. So the idea of a Middle Ware (referred to as the Mid-Ware in Figure 2) is introduced along with the Client/Server method to isolate the application layer from the web server [3]. Thus the framework shown in Figure 1 has been modified to introduce the isolation layer and queues, and the new framework is shown is Figure 2.

In the new framework shown in Figure 2, web users access the web server of IBIDS through the Internet and provide the required information. The web server and the Mid-Ware reside on the same machine. The web server on receiving the information saves them to a User- Request-Queue which can also be accessed by the Mid-Ware. Once the User-Request-Queue has been updated, the Mid-Ware takes control. It reads the request from the User-Request-Queue; decides on all the necessary software components to be invoked; creates all the necessary component requests; and sends them to the different components in the
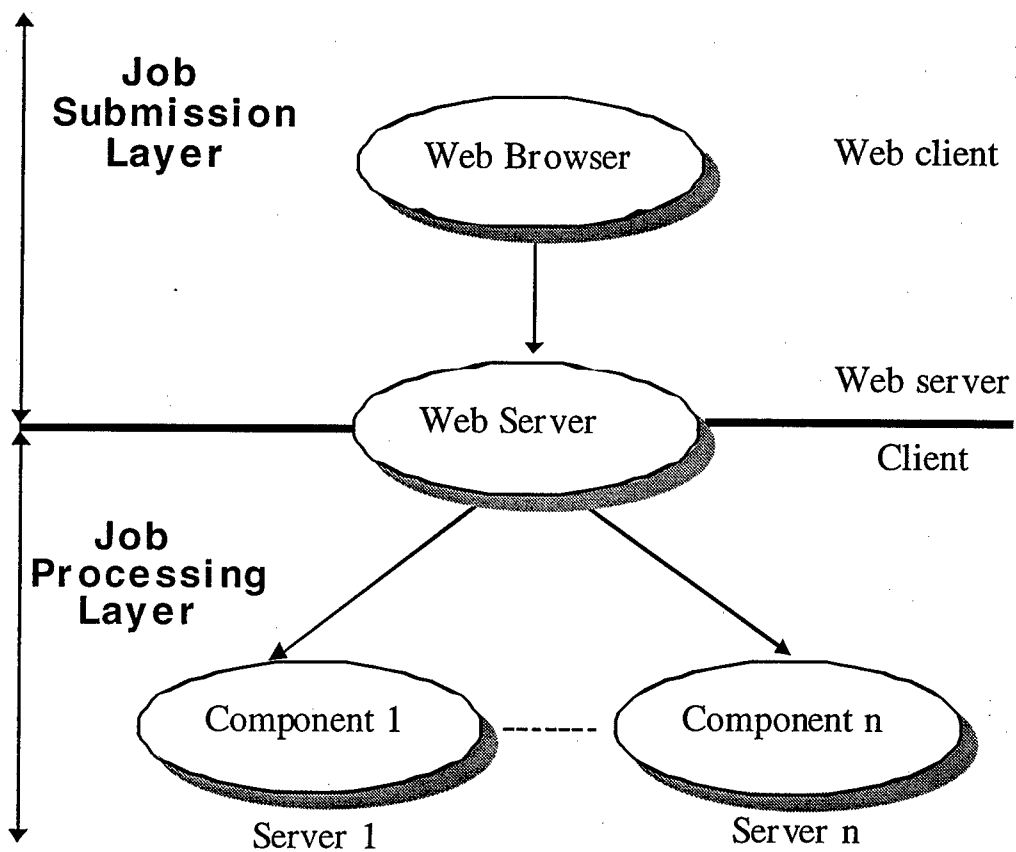
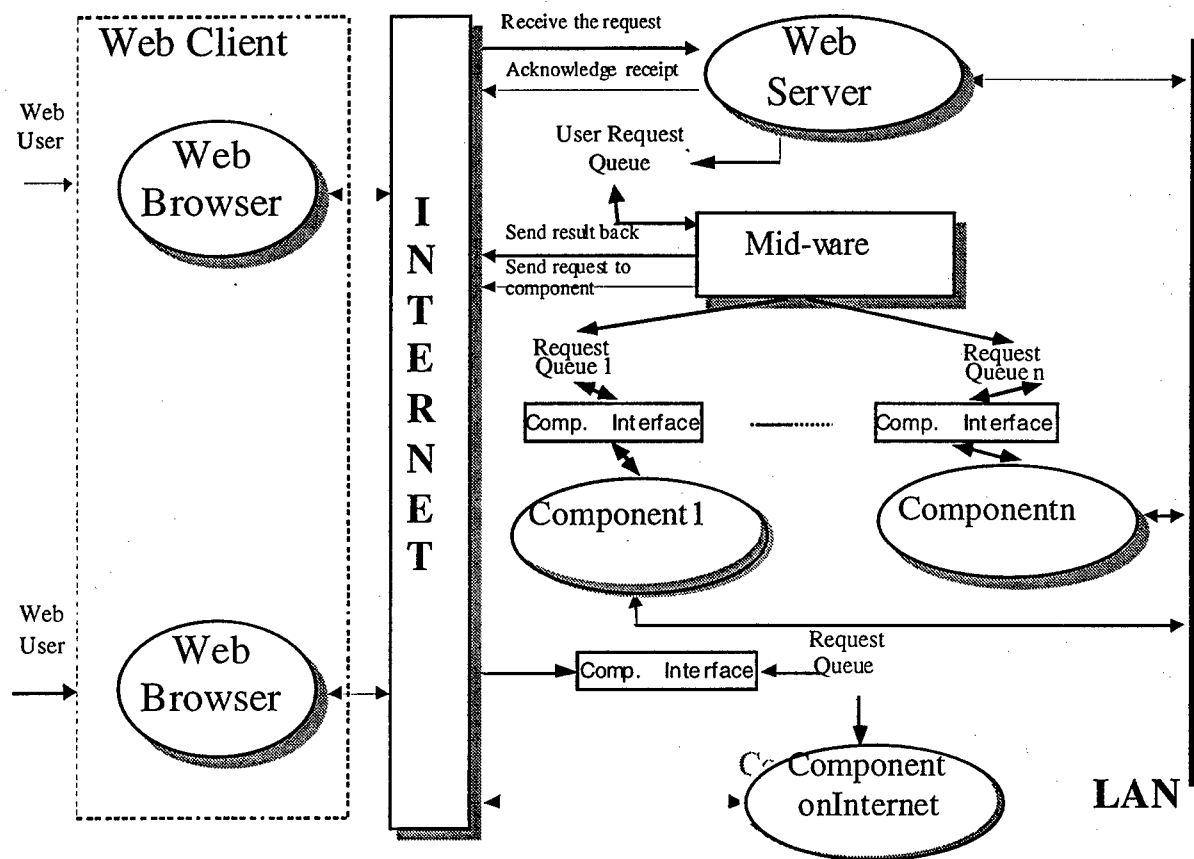Figure 7.1: Client/Server technology in IBIDS.

Figure 7.2: Framework of IBIDS.

proper order. Each software component is provided with its own interface in order to achieve a secure environment and the Mid-Ware communicates with this component interface via a queue.

Two possible situations arise when the Mid-Ware sends the requests to the software component interfaces:

- If the component is located in the same LAN and shares the same file system as the Mid-Ware, the requests are saved directly to the request queue of the component.

- If the component is connected through the Internet, the requests are sent to the component interface, and the component interface adds the requests to its request queue.

After sending all the requests, Mid-Ware then waits for the results. Component interfaces simply read their request queues; run the respective software components and place the results of different requests into the result document space. All these results are collected by Mid-Ware into a web page and the URL of the result web page is sent back to the web user.

From the design of the framework, it can be seen that the following elements have to be implemented:

- All the necessary web pages and the form-related CGI programs, which form the web user interface

- Mid-Ware, which is the bridge between the web server and the components

- The interface for the components which manages the component-request-queue; runs the component and places the results into the result document space.

In the following section, the environment chosen to demonstrate this design is briefly introduced.

7.4.2 Hardware and Software Components of the Engineering Application

For the purpose of demonstration, a mechanical engineering application has been selected. This application is used in the design and manufacture of aerospace products using Superplastic Forming (SPF) methods. The layout of this distributed environment is shown in Figure 3.

The computer hardware includes a Silicon Graphics (SGI) Origin 200 Server (hostname: amml) and two Silicon Graphics (SGI) O2 workstations that run under UNIX, (hostnames:
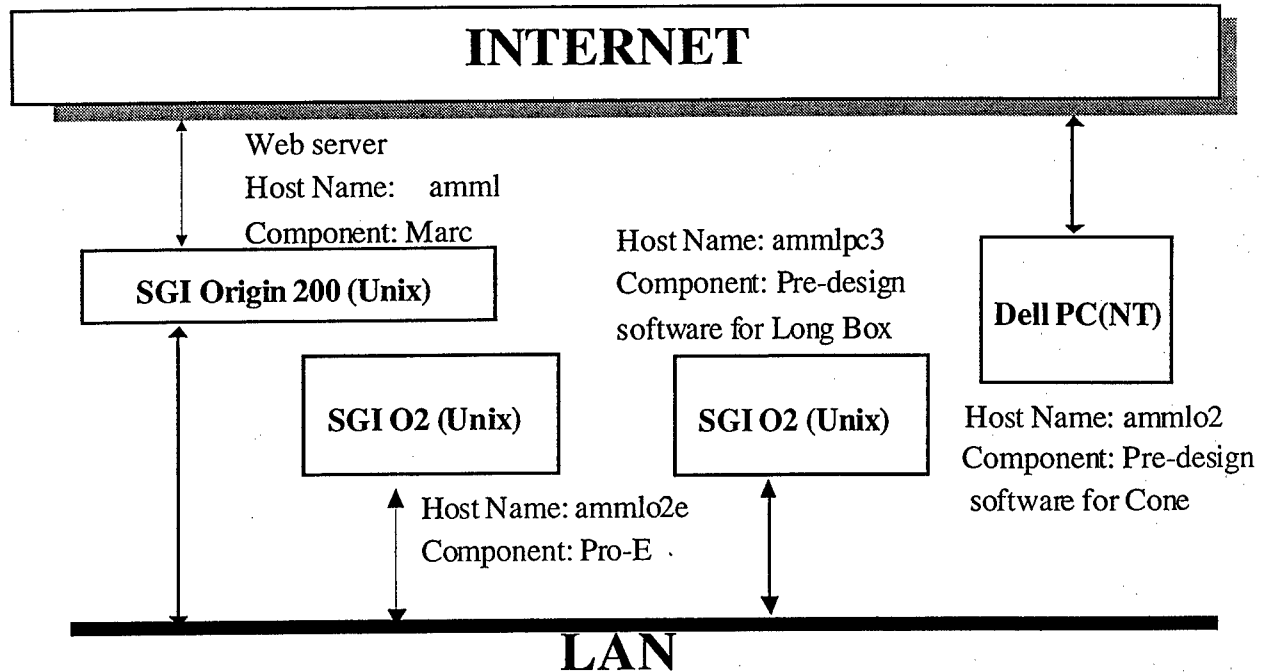
Figure 7.3: Operating environment.

ammlo2 and ammlo2e) and, a Dell PC which runs Microsoft Windows NT 4.0 (hostname: ammlpc3). The software components of this application are as follows:

- Pro-E: Computer Aided Design (CAD) software for SPF component that runs on SGI O2 (ammlo2e)

- MARC/Mentat: Pre- and Post- Processing for SPF component that runs on SGI Origin 200 (amml)

- Pre-design software for SPF component Cone that runs on the second SGI O2 (ammlo2)

- Pre-design software for SPF component Long Box that runs on Dell PC (ammlpc3)

- Post-design software that runs on ammlpc3 and ammlo2

7.4.3 Implementation of the Mechanical Engineering Application

Perl is used to implement Mid-Ware and the component interfaces of this system since it has a very convenient CGI and network programming interfaces. HTML is used to create all web pages, several JavaScript functions are added to HTML codes to validate the input data from user. Figure 4 shows the implementation of IBIDS.

Figure 7.4: Implementation of IBIDS.

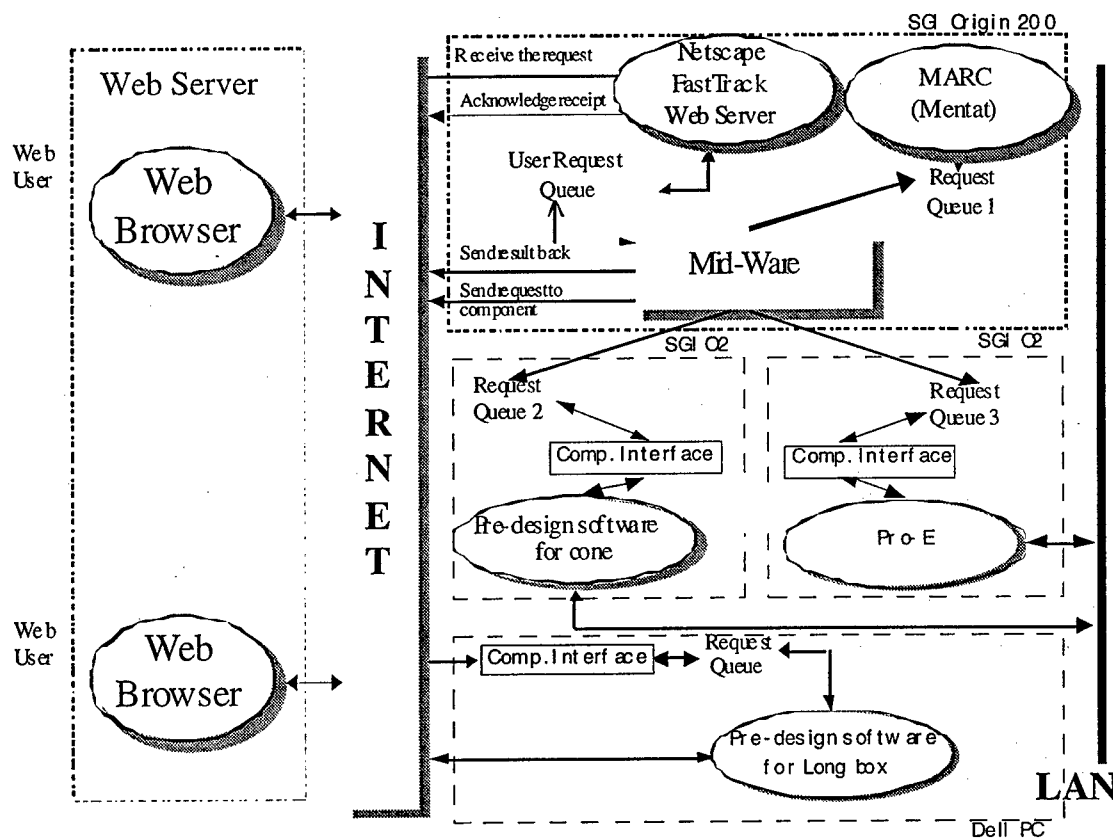Mid-Ware is a daemon program that runs on the same machine as the web server. It checks the User-Request-Queue periodically; processes a request by preparing the input templates; communicates with the component interfaces in the proper order; collects the textual and graphical results into a web page; and notifies the user the URL of the result page. If the component servers share a file system with the web server, the request is directly written to request queue. Otherwise, Mid-Ware creates a socket to communicate with the component interface via the Internet and the component interface adds the request to its queue. The component interface is also a daemon program that runs on each component server. It checks the request queue periodically; processes a request by running the component; saves the results in a directory.

Basic user authentication has been added to disallow unauthorized accesses. Very secure CGI scripts have been written to avoid malicious attacks. Further, the Mid-Ware isolates the execution of programs from the web server script. A fully functional system has been implemented and is currently being used via the URL http://amml.eng.fsu.edu/~shi.

7.5   Summary and Conclusions

We have presented a framework for an Internet based integrated design system (IBIDS). The design considered the control, data and user interface dimensions along with web security. It combined the traditional client/server technology with the middleware to address the security problems inherent in all web applications. It also used Basic User Authentication method to control access to the system as well as the results. A mechanical engineering application involving the manufacture of superplastically formed components was implemented to demonstrate the framework. The design is flexible enough to add more components using the request queues and the component interfaces. Further work is in progress to include exception handling with respect to software and/or hardware failure and resource allocation.

References

1. Chandra, N., Analysis of Superplastic Metal Forming by a Finite Element Method, International Journal for Numerical Methods in Engineering, Vol. 26, 1988, pp. 1925-1944.

2. Deshmukh, A., Middelkoop, T., Krothapalli, A., Shields, W., Zhang, C., Chandra, N., Challa, M., and Smith, C., Multi-Agent design Architecture for Integrated design Systems, American Institute of Aeronautics and Astronautics Paper 98-0914, 1998.

3. Duchessi, P., and Chengalur-Smith, I., Client/Server Benefits, Problems, Best Practices, Communications of The ACM, Vol. 41, No. 5, May 1998, pp. 87-94.

4.   Middleware White Paper, International Systems Group, Inc.   1997, http://www.openvms.digital.com/openvms/whitepapers/middleware/isgmidware.html

5. Joshi, A., Ramakrishnan, N., and Houstis, E., Multiagent System Support of Networked Scientific Computing, IEEE Internet Computing, Vol. 2, No. 3, May/June 1998, pp. 69-83.

6. Macgregor, R. S., Arest, A., and Siegert, A., WWW Security, Prentice-Hall, Inc., 1996, ISBN 0-13-612409-7.

7. Oppliger, R., Internet Security: Firewalls and Beyond, Communications of The ACM, Vol. 40, No. 5, May 1997, pp. 92-102.

8. Ousterhout, J., Scripting: Higher Level Programming for 21st Century, IEEE Computer, Vol. 2, No. 2, March 1998, pp. 23-30.

9. Rubin, A., and Geer, D., A Survey of Web Security", IEEE Computer, Vol. 31, No. 9, September 1998, pp. 34-41.

10. Schefstrom, D. , Tool Integration, John Wiley & Sons Ltd., 1993, ISBN 0-471-93554-9.

Chapter 8

Conclusions

A micro-mechanical model using the concept of threshold stress has been proposed to model the superplastic deformation process. On a grain level, strains produced by diffusional and dislocational accommodation mechanisms are explicitly computed based on the fundamental material properties. The self-consistent method using Eshelby's approach is used to account for the effect of heterogeneity arising from the crystallographic orientation and the consequent stress field. The model is successfully applied to aluminum-based conventional superplastic materials. The material constants including the threshold stresses (σ_*) are evaluated from experimental data. These constants except σ_* are found to be true constants for a particular material irrespective of temperature and grain size etc. σ_* is found to be strongly dependent on temperature and independent of grain size. σ_* is also expressed in the form of activation energy, which can explain the decrease in σ_* levels with increase in temperature. Efforts to apply the threshold stress concept to the high strain-rate superplastic (HSRS) materials are currently in progress.

The model has been extended to characterize the dual-phase superplastic deformation process and is successfully applied to two-phase Ti-6Al-4V and Zn-22Al materials. The flow stresses as a function of temperature and grain size and strain rate sensitivity (m) are predicted for a wide range of strain rates. The threshold stress (σ_*) introduced to the diffusional flow at slip system level manifests as experimentally observed threshold stress at the macro level, and was found to be strongly dependent on temperature. The diffusion contribution to the strain rate is dominant at low strain-rate regions, while the dislocational contribution becomes significant as the strain rate increases in both the material systems.

Interatomic potentials using Embedded Atom Method (EAM) are used in conjunction with molecular statics and dynamics calculations to study the sliding and migration of (110) symmetric tilt grain boundaries (STGB) in aluminum, under both applied displacement and force conditions. Three low energy configurations (corresponding to $\Sigma 3(1\bar{1}1)$, $\Sigma 3(1\bar{1}2)$ and $\Sigma 11(1\bar{1}3)$ twin structures) are found in the [110] STGB structures when grain boundary energies at 0 K are computed as a function of grain misorientation angle. "*Pure*" GBS without migration is implemented by applying external displacement. The propensity for

"pure" GBS is evaluated by computing the energy associated with incremental equilibrium configurations during the sliding process, and the magnitude of the energy barriers is found to be much higher than that with migration. In contrast, in the applied stress conditions, the energy barriers are reduced due to the fact that grain boundary sliding of STGB is always coupled with apparent migration. Thus the study clearly shows that in these special grain boundaries(STBGs), migration is coupled with sliding during GBS. It is seen that when the free energy in the grain boundary decreases (more specialized boundaries approaching twin boundaries), the boundary offers more resistance to sliding and, consequently, migration. The computational results indicate that if we can engineer grain boundary, we can decrease the GB energy to decrease deformation rate (e.g. creep resistance) and increase GB energy to promote sliding (e.g. superplasticity).

On macro level, we focus on pre-existing cavities and cavitation evolution. Although the subject of pre-existing cavitation is controversial, it does exist in the two important Aluminum based superplastic materials we have examined. The evidence is provided by the direct observation of as-received Al 5083 and Al 7475 sheet metal samples. The occurrence of pre-existing cavities is associated with second phase particles, especially those of a larger size. Numerical simulation verifies that there is a possibility of introduction of pre-existing cavities during single pass rolling process and that the occurrence depends on thickness reduction, particle size and bonding between particle and matrix.

An Al-Mg-Mn-Cr alloy were deformed under both uniaxial and equi-biaxial stress state at a constant strain rate of $5x10^{-4}s^{-1}$ to compare the difference of cavity nucleation, growth and interlinkage behavior. Cavity volume fraction obtained from density measurement, and number density, size distribution obtained from image analysis indicated that the cavity growth rate is higher in the equibiaxial stress state than that in the uniaxial stress state. The failure of the material occurred earlier in the uniaxial stress state than that in the equibiaxial stress state since in the uniaxial stress state, cavities were more prone to interlink. Stress analysis indicated that in the interlinkage area, higher stress concentration can be produced in the uni-axial stress state.

A framework for an Internet based integrated design system (IBIDS) has been developed. The design considered the control, data and user interface dimensions along with web security. It combined the traditional client/server technology with the middleware to address the security problems inherent in all web applications. It also used Basic User Authentication method to control access to the system as well as the results. A superplastic forming processing was implemented to demonstrate the framework.

Appendix

To determine the ratio of $\frac{a_b}{a_l}$ in the diffusion equation:

The total strain rate contribution from diffusion can be considered to be the sum of the contributions from both lattice and grain boundary diffusion.

$$\dot{\epsilon}_{diffusion} = \dot{\epsilon}_{lattice} + \dot{\epsilon}_{boundary}$$

$$\dot{\epsilon}_d = \dot{\epsilon}_l + \dot{\epsilon}_b$$

For each slip system in the model, the contribution from lattice and boundary diffusion can be given as,

$$\overset{(k)}{\dot{\epsilon}}_d = a_l \frac{1}{Td^2} exp\left(\frac{-Q_L}{RT}\right)(\overset{(k)}{\sigma_n}) + a_b \frac{1}{Td^3} exp\left(\frac{-Q_B}{RT}\right)(\overset{(k)}{\sigma_n}) \tag{.1}$$

But from Ashby-Verrall equation (neglecting threshold stress), the contribution from lattice and boundary diffusion are given in macro scale as,

$$\dot{\epsilon}_d = \frac{100\Omega}{kTd^2} D_L \sigma + \frac{100\Omega}{kTd^3}(3.3\delta) D_B \sigma \tag{.2}$$

where, Ω is atomic volume, k is the Boltzmann constant, δ is the grain boundary thickness, σ is the applied stress and D_L and D_B are the lattice and boundary diffusion coefficients at a specified temperature.

From Equation (.1),

$$\frac{\dot{\epsilon}_b}{\dot{\epsilon}_l} = \frac{a_b}{a_l} \frac{Td^2}{Td^3} \frac{exp\left(-Q_B/RT\right)}{exp\left(-Q_L/RT\right)}$$

$$\frac{\dot{\epsilon}_b}{\dot{\epsilon}_l} = \frac{a_b}{a_l} \frac{1}{d} \frac{exp\left(-Q_B/RT\right)}{exp\left(-Q_L/RT\right)} \tag{.3}$$

From Equation (.2),

$$\frac{\dot{\epsilon}_b}{\dot{\epsilon}_l} = \frac{3.3\delta}{d} \frac{D_B}{D_L} \tag{.4}$$

Equating right hand side expressions in Equations (.3) and (.4),

$$\frac{a_b}{a_l} \frac{1}{d} \frac{exp\left(-Q_B/RT\right)}{exp\left(-Q_L/RT\right)} = \frac{3.3\delta}{d} \frac{D_B}{D_L}$$

$$\frac{a_b}{a_l} = 3.3\delta \frac{D_B}{D_L} \frac{exp\left(-Q_B/RT\right)}{exp\left(-Q_L/RT\right)}$$

112

where $D_B = D_{0B} \, exp(-Q_B/RT)$ and $D_L = D_{0L} \, exp(-Q_L/RT)$

Hence,

$$\frac{a_b}{a_l} = 3.3\frac{\delta D_{0B}}{D_{0L}} = r$$

Since δ, D_{0B} and D_{OL} are material constants, the ratio a_b/a_l is a constant for a given material independent of temperature, grain size etc.

For example, the constant r for pure aluminum is 9.709 x 10^{-10}.